



PONTIFICIA UNIVERSIDAD CATÓLICA DE CHILE  
ESCUELA DE INGENIERÍA

# **BIOMECHANICAL QUANTIFICATION OF THE HEART USING CARDIOVASCULAR MAGNETIC RESONANCE IMAGES**

**HERNÁN ARTURO MELLA LOBOS**

Thesis submitted to the Office of Graduate Studies  
in partial fulfillment of the requirements for the Degree of  
Doctor in Engineering Sciences

Advisor:  
**SERGIO URIBE**

Santiago de Chile, 13 August 2021

© MMXXI, HERNÁN ARTURO MELLA LOBOS



PONTIFICIA UNIVERSIDAD CATOLICA DE CHILE  
SCHOOL OF ENGINEERING

# BIOMECHANICAL QUANTIFICATION OF THE HEART USING CARDIOVASCULAR MAGNETIC RESONANCE IMAGES

**HERNÁN ARTURO MELLA LOBOS**

Members of the Committee:

**SERGIO URIBE**

DocuSigned by:

*Sergio Uribe*

3A85961CD999485...

DocuSigned by:

**DANIEL HURTADO**

*D. Hurtado*

4AD1C27AD1BB4B6...

DocuSigned by:

**JOAQUÍN MURA**

*Joaquín Mura*

7A24BCB91DB346B...

DocuSigned by:

**CLAUDIO GARCÍA**

*Claudio García Herrera*

86DEF7D92749413...

DocuSigned by:

**HUI WANG**

*Hui Wang*

59D66416D636416...

DocuSigned by:

**GUSTAVO LAGOS**

*Gustavo Lagos C.*

B558E6FD3B4641F...

Thesis submitted to the Office of Graduate Studies in partial fulfillment of  
the requirements for the Degree Doctor in Engineering Sciences

Santiago de Chile, August, 2021

© MMXXI, HERNÁN ARTURO MELLA LOBOS

*Para los que hicieron este viaje  
más llevadero*

## ACKNOWLEDGEMENTS

I want to thank the people that guided and inspired me through this investigation. To my Biomedical Imaging Center teammates for the insightful discussions, particularly during the funny lunches, eternal and several coffee breaks, and the COD parties. My professors, who under their experienced eyes, gave me the best guidance. Sergio Uribe, for the trust, the knowledge, and the advice placed in me.

Of course, I gratefully acknowledge my family, whose support and love made me complete this journey. Notably, thanks to Sonia, my beloved wife, for being all that I needed and more. To Oscar, my son, for his innocent and sincere love and the deep and helpful discussions about the heart, MRI, and universe.

Also, I would like to thank the financial support of ANID through the Ph. D. scholarship 21170592, CONICYT-PIA-Anillo ACT1416, and ANID-Millennium Science Initiative Program - NCN17\_129.

## TABLE OF CONTENTS

ACKNOWLEDGEMENTS	v
LIST OF FIGURES	x
LIST OF TABLES	xx
ABSTRACT	xxi
RESUMEN	xxiii
1. INTRODUCTION	1
1.1. Overview . . . . .	3
1.2. Physical principles of MRI . . . . .	4
1.2.1. Magnetization . . . . .	4
1.2.2. RF excitation . . . . .	6
1.2.3. Relaxation . . . . .	7
1.2.4. Spatial encoding of the image . . . . .	8
1.2.5. The signal equation . . . . .	12
1.3. Tagging Magnetic Resonance Imaging . . . . .	14
1.4. Motion estimation techniques from tagged MR images . . . . .	17
1.5. Biomechanical quantification using cardiac strain . . . . .	22
1.6. Objectives and hypothesis . . . . .	23
1.6.1. Hypothesis . . . . .	24
2. FIRST ARTICLE: A COMPREHENSIVE COMPARISON OF MOTION ESTIMATION TECHNIQUES	25
2.1. Title and authors . . . . .	25
2.2. Introduction . . . . .	25
2.3. Material and methods . . . . .	29
2.3.1. Image generation . . . . .	29

2.3.2.	CSPAMM magnetization . . . . .	30
2.3.3.	DENSE magnetization . . . . .	30
2.3.4.	Numerical experiments . . . . .	31
2.3.5.	Image processing . . . . .	36
2.3.6.	Motion estimation . . . . .	38
2.3.7.	Statistical analysis . . . . .	39
2.4.	Results . . . . .	40
2.4.1.	Sensitivity analysis: resolution . . . . .	40
2.4.2.	Sensitivity analysis: noise . . . . .	41
2.4.3.	3D experiment . . . . .	45
2.5.	Discussion . . . . .	47
2.6.	Acknowledgments . . . . .	51
3.	<b>SECOND ARTICLE: A NOVEL METHOD FOR MOTION ESTIMATION</b>	52
3.1.	Title and authors . . . . .	52
3.2.	Introduction . . . . .	53
3.3.	Methods . . . . .	56
3.3.1.	Principle of HARP-I . . . . .	56
3.3.2.	Strategies for correcting temporal phase inconsistencies . . . . .	60
3.3.3.	Application of HARP-I in oblique directions . . . . .	61
3.3.4.	Implementation of HARP-I . . . . .	62
3.3.5.	Implementation of SP-HR and SinMod . . . . .	63
3.4.	Experiments . . . . .	64
3.4.1.	In-silico experiments . . . . .	64
3.4.2.	In-vivo experiments . . . . .	65
3.4.3.	Statistical analysis . . . . .	66
3.5.	Results . . . . .	67
3.5.1.	Noise-free experiments . . . . .	67
3.5.2.	Noisy experiments . . . . .	69
3.5.3.	Motion estimation on healthy volunteers . . . . .	71

3.6.	Discussion . . . . .	74
3.7.	Conclusion . . . . .	81
3.8.	Acknowledgements . . . . .	81
4.	THIRD ARTICLE: A NOVEL SEQUENCE FOR TAGGING MRI	83
4.1.	Title and authors . . . . .	83
4.2.	Introduction . . . . .	83
4.3.	Methods . . . . .	86
4.3.1.	Sequence development . . . . .	86
4.3.2.	Phantom and in-vivo data acquisition . . . . .	91
4.3.3.	Image analysis . . . . .	92
4.4.	Results . . . . .	93
4.4.1.	Phantom acquisition . . . . .	93
4.4.2.	In-vivo acquisition . . . . .	96
4.5.	Discussion and conclusions . . . . .	100
4.6.	Acknowledgments . . . . .	104
5.	FUTURE WORK AND PERSPECTIVES	105
5.1.	Short-term: A Phase Complementary SPAMM (PCSPAMM) acquisition to quantify simultaneously tissue motion and flow velocity . . . . .	105
5.2.	Mid-term . . . . .	109
6.	CONCLUSIONS	111
	REFERENCES	113
	APPENDIX	133
A.	Appendix for publication 1 . . . . .	134
A.1.	Motion model . . . . .	134
B.	Appendix for publication 2 . . . . .	137
B.1.	Exact interpolation condition . . . . .	137
B.2.	Evaluated norms in the RBF interpolator . . . . .	137

C.	Summary of participation in other research projects . . . . .	138
C.1.	Research articles . . . . .	138
C.2.	International conferences . . . . .	139
C.3.	National conferences . . . . .	140

## LIST OF FIGURES

1.1	A group of hydrogen spins share the same magnetic moment but randomly oriented in the absence of an external magnetic field ( $B_0 = 0$ ), which leads to a zero net magnetization $M$ . After applying a strong magnetic field ( $B_0 = 1.5\text{T}$ ), the spins align with the magnetic field, resulting in a non-zero net magnetization. . . . .	5
1.2	In presence of a strong $B_0$ field, the net magnetization vector is aligned with this field and precess with an angular frequency $\omega_0$ . After the application of a $90^\circ$ RF pulse ( $B_1$ field) with central frequency $\omega_0$ , the magnetization vector is not longer aligned with $B_0$ . . . . .	6
1.3	(a) T1 and (b) T2 relaxation curves . . . . .	7
1.4	After the application of a RF pulse combined with a slice-selective $z$ -gradient, the precession frequency of the tissue vary linearly with the $z$ position. Depending on the central frequency of the RF pulse, thin slices in different $z$ locations can be excited. For instance, if the RF pulse has central frequency $f_0$ , only the magnetization vectors inside the thin Slice 0 are excited. . . . .	9
1.5	(a) During the readout (the application of a frequency encoding gradient), the spins precess at different frequencies based on their spatial location in the $x$ -direction, generating different signals. (b) The signal that is being readout is a superposition of these signal and it is used to locate the protons in the $x$ -direction. . . . .	11
1.6	(a) During the application of the phase-encoding gradient ( $G_y$ ), each spin is subject to a spatially varying magnetic field $B_0 + y \cdot G_y$ , which makes it to precess at different frequencies. (b) After turning-off the gradient, the spins regain their original frequencies but are dephased in the $y$ -direction. . . . .	12

1.7	(a) The combination of the slice selection, and frequency and phase encodings define an acquisition sequence. (b) The MR signal is acquired in the $k$ -space, which denotes the image in the Fourier domain. (c) After the application of the inverse Fourier transform, the image is recovered. . . . .	13
1.8	(a) Anatomical and (b) tagged MR images of a short-axis LV slice of the heart for an end-diastolic (upper row) and end-systolic (bottom row) cardiac phase. . . . .	14
1.9	Representation of the heart as a continuum body. The motion of the heart is defined through the deformation map $\varphi$ , which maps every material point $P$ from an undeformed state $B_0$ (i.e., end-diastolic position) to its position at a later state $p \in B_t$ . . . . .	22
1.10	Left-ventricle of the heart with the circumferential (CC), radial (RR), and longitudinal (LL) directions represented by red arrows. . . . .	23
2.1	Representation of the synthetic geometry and slices used to generate the images. (a) The geometry in the undeformed state was used to place the basal, mid, and apical slices. (b) As the geometry moves with a clockwise and counterclockwise rotation at the base and apical levels, the isochromats moves in and through the plane of each slice. (c) The displacement field observed in (b) of the isochromats is shown in the same slices, showing the amount of in- and through-plane motion. (d) To estimate the voxel-wise signal, all the isochromats located inside the voxel are identified and used to define weights based on their distance with respect to the voxel center (red sphere). Blue spheres denote the set of isochromats inside the voxel. . . . .	28
2.2	Using the 2D data, displacement and strain fields are estimated for every resolution and noise level described in the Experiments section. Then, the error metrics given in Equations 8a, 8b, and 8c are evaluated. For the 3D data, displacement and strain fields are estimated and the error metric given in Equation 9 is evaluated. . . . .	36

2.3	k-space and reconstructed images for (a) SPAMM and CSPAMM, and (b) DENSE and phase-cycled DENSE of an mid-level short-axis slice. The frames 1, 4, 7, 10, 13, and 19 of an acquisition of 20 frames equally distributed in a cardiac cycle of 1 second are shown. In the case of SPAMM and CSPAMM, the image shows the reconstructed magnitude, whereas for DENSE and phase-cycled DENSE, the reconstructed phase. For the image simulation, a multi-shot EPI acquisition was used in all cases, with half of the lines sampled in the phase direction. . . . .	37
2.4	Results for the resolution sensitivity analysis. Mean errors in (a) magnitude, (b) direction of the displacement field, (c) $E_{CC}$ , and (d) $E_{RR}$ strain components. The left plot of each case shows the results obtained using SP-HR and to the right using SinMod. The results from DENSEanalysis are shown on all the plots. Each color denotes a different tag period ( $s$ ). Overall, the estimation obtained from DENSE images performed better than the other techniques, whereas using CSPAMM images, better results were obtained for smaller pixel sizes and wavelengths. . . . .	40
2.5	Mean errors and standard deviations for the best performing combination of tag periods and pixel sizes of the results given in Figure 4, for (a) magnitude, (b) direction of the displacement field, (c) $E_{CC}$ and (d) $E_{RR}$ strain components. Each color represents a different tag period ( $s$ ). The three methods showed similar results in terms of mean errors and deviations (except in the displacement field magnitude, where deviations obtained with DENSEanalysis remain low). . . . .	42
2.6	Results for the noise sensitivity analysis for an end-systolic cardiac phase. Mean errors in (a) magnitude, (b) direction of the displacement field, (c) $E_{CC}$ , and (d) $E_{RR}$ strain components. The left plot of each metric shows the results obtained using SP-HR and to the right using SinMod. The results from DENSEanalysis are shown in all the figures. Each color denotes a different	

	SNR (see Table 2.1). SP-HR gave the most significant sensitivity to noise in every case, whereas DENSEanalysis showed the smallest. . . . .	43
2.7	Results for the noise sensitivity analysis for an early-systolic cardiac phase. Mean errors in (a) magnitude, (b) direction of the displacement field, (c) $E_{CC}$ , and (d) $E_{RR}$ strain components. The left plot of each metric shows the results obtained using SP-HR and to the right using SinMod. Each color denotes a different noise level. As the displacement is small at the beginning of the cardiac cycle, the impact of noise on the phase of harmonic and stimulated echo images becomes more prominent. As a consequence, worse results were achieved for all the error metrics. . . . .	44
2.8	Regional strains at basal, mid, and apical levels. Each column shows the strain estimated using SP-HR, SinMod, and DENSEanalysis. Gray lines with triangle markers denote the reference curves, while black lines with square markers denote the estimations made with the three processing techniques. Every point in the curves represents the mean regional strain across the segments defined by the AHA (Cerqueira et al., 2002; Selvadurai et al., 2018). Analysis of CSPAMM images using SP-HR tends to fail for cardiac phases in the diastolic part of the cardiac cycle, resulting from the signal decay. . . . .	45
3.1	Representation of motion of a continuum body. The motion of the body $\mathbf{R}_0$ is completely defined through the deformation map $\varphi$ , which maps every material point $\mathbf{P} \in \mathbf{R}_0$ to its position at a later state $\mathbf{p} \in \mathbf{R}_k$ . . . . .	57
3.2	(Left image) Tagged image with tag-lines pointing towards the oblique direction $x^*$ , given by the angulation $\theta$ . (Right image) The Fourier transform of the tagging image gives a frequency spectrum in the domain $[\omega_x, \omega_y]$ , with the first harmonic peak centered at a frequency $\Omega$ over the $\omega_x^*$ axis. The central frequency of the bandpass filter (gray broken lines) coincides with $\Omega$ . . . . .	58

3.3	Phase-distance matrices (upper row) and the corresponding unwrapped harmonic phases (bottom row). Figure (a) shows the distance matrix and phase for the reference frame, whereas (b) and (c) show the uncorrected (left) and corrected (right) distance matrices and phases for frames 5 and 12. The matrices were obtained from an image of a healthy volunteer with taglines in the direction given by $\theta = 45^\circ$ (see Figure 3.2) and using only the pixels inside the LV (this explains why the matrix size is square in (a) but non-square in (b) and (c). See (3.11) for the definition of distance matrices). The colors on all the plots share the same scale. . . . .	60
3.4	(a) First and (b) last frames of a noisy synthetic data. The red circle denotes the place where the stiffer inclusion was added. The contrast of the images (see Eq. 3.16) was set differently for a better visualization. Both images were obtained using the $WL_5$ . . . . .	64
3.5	Mean errors and deviations in the estimation of displacement magnitude (first row), direction (second row), circumferential strain (third row), and radial strain (fourth row) for wavelengths of (a) 2.9 ( $WL_3$ ), (b) 4.9 ( $WL_5$ ), and (c) 6.9 ( $WL_7$ ) pixels. The label in the $x$ -axis denotes the amount of radial and angular displacement of the synthetic data (in the last case, the $x$ -axis represents $r$ times the angular displacement, as stated by Eq. 3.17), while in the $y$ -axis, CC and RR stand for circumferential and radial strain components. For all the displacement levels and wavelengths, the performance of HARP-I was superior than SP-HR and SinMod. . . . .	68
3.6	Mean errors and deviations in the estimation of displacement magnitude (first row), direction (second row), circumferential strain (third row), and radial strain (fourth row) for the noisy experiment for wavelengths of (a) 2.9 ( $WL_3$ ), (b) 4.9 ( $WL_5$ ), and (c) 6.9 ( $WL_7$ ) pixels. Strain estimations obtained SP-HR, SinMod, and HARP-I followed a similar behavior than the displacement magnitude and direction. However, the error increased due to the presence of noise. . . . .	70

3.7	Circumferential strain maps obtained with SP-HR, SinMod, and HARP-I for one representative sample of noisy data using $WL_5$ . Rapid spatial variations were observed in estimations made with SP-HR and SinMod, whereas more accurate and homogeneous results were obtained using HARP-I. . . . .	71
3.8	Circumferential strain of a short-axis view of the left ventricle for 5 volunteers at end-systole and late-diastole (the last frame acquired). We used late-diastole to emphasize that in ECG triggered MR images, the cardiac cycle is not completely sampled. All the maps are presented in the reference cardiac phase (first frame) and were estimated using SP-HR (left), SinMod (middle), and HARP-I (right). The red dots indicate the insertion points of the RV walls into the LV. Each volunteer was identified with a number to make it easier to refer. The volunteers 7 and 13 presented abnormal strain patterns as they presented cardiomyopathies. The first case showed a hypokinetic LV and the second hypertrophic cardiomyopathy. SP-HR showed strain maps with artifacts on 3 of the 5 cases, whereas SinMod and HARP-I showed similar results at end-systole for most of the cases. Nonetheless, at late-diastole (where cardiac strain in healthy subjects should be small as the heart relaxes and come back to its reference position) some artifacts were observed with three methods in almost all cases. However, HARP-I showed a more stable behavior across the whole cardiac cycle. . . . .	72
3.9	Accumulated (across all volunteers) fraction of pixels with circumferential strain ( $E_{CC}$ ) with unlikely high values. The X-axis denotes the frame of the cardiac cycle relative to the first one. The fraction was estimated as the number of pixels satisfying $ E_{CC}  > 0.5$ divided by the number of pixels inside the left ventricle. Results were added together no matter if they shared the same number of frames (this explains why SP-HR and SinMod shows curves with increasing and decreasing behavior). . . . .	74

3.10	Circumferential strain curves estimated with SP-HR, SinMod, and HARP-I for in-vivo data (highly unlikely strain values bigger than 0.5 were not considered for the estimation of the curve with SP-HR and SinMod methods, not so with HARP-I). The number on each plot is a label to make it easier to refer to the result of each volunteer. Results remarked with blue boxes are the same as those presented in Figure 3.8. The volunteers 7 and 13 presented abnormal strain patterns as they presented cardiomyopathies. The first case showed a hypokinetic LV and the second hypertrophic cardiomyopathy. . . . .	74
3.11	Motion estimated from a 3D CSPAMM image of a healthy volunteer using HARP-I and SinMod. The figure shows a slice of the 3D volume at (a) frame 2 and (b) 10 of the cardiac cycle (the first frame was not used because of the lack of contrast between the cardiac walls and the blood pool) and the circumferential strain and displacement field (arrows) at frame 10 estimated using (c) HARP-I and (d) SinMod. The red and blue dot denotes the position of two points manually tracked. Figures (e) and (f) shows the global strains of the circumferential, radial, and longitudinal components (GCS, GRS, and GLS, respectively) obtained with HARP-I and SinMod. The strain maps were plotted in the range $[-0.5, 0.2]$ . . . . .	75
4.1	(A) CSPAMM, (B) O-CSPAMM, (C) ORI-CSPAMM, and (D) ORI-O-CSPAMM tagging preparations. In all the figures, M, P, and S denote the measurement, phase, and slice axes. In the ORI-CSPAMM sequence, the spurious phase gained during the tagging preparation is rewound by splitting the tagging gradient into two parts separated by a $180^\circ$ refocusing hard pulse. . . . .	86
4.2	Fat and water masks used for the estimation of the Normalized Mean Signal in (A) ORI-CSPAMM and (B) ORI-O-CSPAMM images. . . . .	92
4.3	Water and fat phantom images obtained using complex difference (CD. Upper row) and MICSR (bottom row). The images were acquired using	

(A) bSSFP, (B) CSPAMM, (C) ORI-CSPAMM, (D) O-CSPAMM, and (E) ORI-O-CSPAMM sequences. The trigger delay of each image is shown in the figures and varies due to the different duration of the preparation pulses. The images acquired without ORI preparation showed a shift in the tagging pattern at the water-fat interface. The MICSR image obtained from O-CSPAMM lost the grid pattern as predicted in Eq. 4.4d. . . . . 93

4.4 k-spaces of the (A) first complementary image acquired by each sequence and (B) the complex difference (CD) reconstructions. High-frequency spectral peaks are present on all the images in (A) although are less visible with ORI-O-CSPAMM (see red arrows). In the complex difference images, the most energetic high-frequency peaks are completely removed with all the sequences but not with O-CSPAMM (see red arrows in (B)), which generate distortions in the water part of the phantom image (see Fig. 4.3). Although 45° rotated and weaker gradients were applied using ORI-O-CSPAMM, the same encoding frequency (tag period) was achieved compared to the other sequences (see blue vertical arrows in (B)). . . . . 94

4.5 Normalized mean signal in the fat (A) and water (B) obtained from images reconstructed using complex difference (CD) and MICSR, from data acquired using ORI-CSPAMM and ORI-O-CSPAMM sequences. The normalized signal from an ORI-CSPAMM acquisition is shown using a blue and red continuous line respectively, while curves obtained from an ORI-O-CSPAMM acquisition are displayed using blue and red square markers. . . . . 96

4.6 Images acquired using the O-CSPAMM (second column) and ORI-O-CSPAMM (third column) sequences and reconstructed using complex difference (CD) and MICSR for (A) volunteer 1, (B) volunteer 2, and (C) volunteer 3. Each volunteer has a bSSFP image as reference. The displayed images correspond to the end-diastolic cardiac phase. The discrepancies in the trigger delay times are due to the difference in the duration of the

	preparation pulses. The red arrows show the places where the grid is distorted by the presence of epicardial and subcutaneous fat. The images acquired with ORI-O-CSPAMM did not show any distortion in the places indicated by arrows. . . . .	97
4.7	Images acquired using the O-CSPAMM (second column) and ORI-O-CSPAMM (third column) sequences and reconstructed using complex difference (CD) and MICSR for (A) volunteer 1, (B) volunteer 2, and (C) volunteer 3. Each volunteer has a bSSFP image as reference. The displayed images correspond to the end-systolic cardiac phase. The discrepancies in the trigger delay times are due to the difference in the duration of the preparation pulses and the cardiac cycle. The red arrows show the places where the grid is distorted by the presence of epicardial and subcutaneous fat. The images acquired with ORI-O-CSPAMM did not show any distortion in the places indicated by arrows. . . . .	99
4.8	Phase of the complex difference (upper row) and MICSR images (bottom row) obtained from (A) CSPAMM, (B) ORI-CSPAMM, (C) O-CSPAMM, and (D) ORI-O-CSPAMM sequences. In complex difference images the phase is always non-zero while in MICSR images the phase is zero and $\pi$ (the last is due that MICSR images have only real part that varies from positive to negative values). . . . .	102
5.1	Pulse sequence diagram of the proposed PCSPAMM sequence. Bipolar gradients with opposite polarities are applied after the excitation RF pulse during the readout in each SPAMM acquisition. . . . .	106
5.2	MICSR and real part of the CSPAMM image reconstructed from PCSPAMM data at end-systole. After the inhomogeneity correction, the CSPAMM image did not showed lines distortions, leading to a sinusoidal pattern similar to MICSR. . . . .	107

5.3	PC images estimated using PCSPAMM (top row) and a SPAMM-PAV-like reconstruction for trigger times of (a) 10 msec and (b) 505 ms. In both cases the velocity is shown in the AP and FH directions, and the red circle denotes the ROI placed near the mitral valve. In our proposal the phase is almost free of artifacts generated by the sinusoidal tagging modulation. . . . .	108
5.4	Mean velocity magnitude in a ROI placed close to the mitral valve obtained from PCSPAMM and SPAMM-PAV. . . . .	109
A.1	Modulation function used to weight the cardiac motion. . . . .	134

## LIST OF TABLES

2.1	Noise levels and corresponding Signal to Noise Ratios in the noise sensitivity analysis images. The noise level has the same standard deviation throughout the cardiac cycle. However, from early-systole to late-diastole, the SNR decreases due to the signal model given in Equations 2.4 and 2.6. The reported SNR has adimensional units. . . . .	33
2.2	Physiological parameters used for the generation of images with 3D motion patters . . . . .	35
2.3	$Err_{seg}(\%)$ for the results of the 3D experiment. Results show how far the regional strains estimated with the three methods are from the reference values. From base to apex, the synthetic phantom rotation increases, and higher errors were found using SP-HR and SinMod. . . . .	46
3.1	Diagnoses and/or MRI findings for subjects with abnormal ventricular contraction . . . . .	66
4.1	Imaging parameters used during the acquisition of the in-silico and in-vivo data. All the volunteers shared the same imaging parameters, only differing in the number of cardiac phases. . . . .	91
A.1	Set of parameters used to generate the synthetic geometries and motion patterns. The notation $x \sim \mathcal{U}(a, b)$ means that for every simulation, the variable $x$ was selected from a uniform distribution on the range $(a, b)$ . The epicardial radius is calculated using $R_{ep} = R_{en} + \tau$ , $d_{en} = (1 - S_{en})R_{en}$ , and $d_{ep}$ was calculated to obtain the change in left-ventricular area imposed by $S_{ar}$ . . . . .	136

## ABSTRACT

Cardiac MRI is a valuable tool for studying cardiac function. Particularly, cardiac tagging MRI combined with advanced processing techniques allows the estimation of the tissue motion and strain, which could help for an early assessment of several diseases. However, state-of-the-art tagging sequences and processing methods suffer from several issues, including but not limited to sensibility to off-resonance, prolonged scanning times, and poor signal for tagging sequences; and sensibility to through-plane motion, large frame-to-frame displacements, and low frequencies contamination for processing techniques. In this thesis, three research articles intended to tackle some of these previous issues are presented.

The first article is a comprehensive comparison of image processing techniques applied to tagged and DENSE MR images under several imaging conditions, including non-ideal cases. This research's primary outcome was the optimum combination of imaging parameters to obtain the best results after applying the motion estimation techniques. The second article introduced HARP-I, a novel motion estimation technique based on tagged MR images that outperformed the state of the art techniques in many aspects. The main outcomes include the reduction in the estimation sensitivity to low-frequencies contamination, noise, and large frame-to-frame displacement problem. The last article presented ORI-O-CSPAMM, a new tagging MR sequence that allowed the acquisition of CSPAMM and MICSR grids in half scan time. ORI-O-CSPAMM also allowed the removal of off-resonance artifacts during the tagging preparation, which is helpful in the presence of fat.

The three research papers presented improvements to the three essential parts of the estimation of cardiac strain, including the acquisition sequence, the imaging parameters, and the image processing tool.

**Keywords:** Cardiovascular MRI, Cardiac MRI, Tagging MRI, Strain imaging, motion estimation.

## RESUMEN

La Resonancia Magnética (RM) cardíaca es una herramienta valiosa para el estudio de la función cardíaca. Particularmente, las imágenes de RM de tagging combinadas con herramientas de procesamiento avanzadas, permiten la estimación del movimiento del tejido y sus deformaciones, y por lo tanto la detección y seguimiento temprano de varias enfermedades. Sin embargo, las secuencias de tagging y los métodos de procesamiento sufren de numerosos problemas, incluyendo pero no limitado a la sensibilidad a efectos de off-resonance, tiempos de adquisición elevados y mala señal en cuanto a imágenes de tagging; y sensibilidad al movimiento a través del plano, grandes desplazamientos entre imágenes consecutivas y contaminación por bajas frecuencias en cuanto a técnicas de procesamiento. En esta tesis se presentan tres artículos que buscan solucionar algunos de los problemas previamente descritos.

El primer artículo es una comparación rigurosa de técnicas de procesamiento aplicadas a imágenes de RM de tagging y DENSE bajo distintas condiciones de adquisición, incluyendo casos no-ideales. Uno de los resultados principales, es la obtención de la combinación óptima de parámetros de adquisición que mejoran los resultados de las técnicas de procesamiento. El segundo artículo introduce la técnica de procesamiento HARP-I, la que a partir de imágenes de RM de tagging, supera al estado del arte en cuanto a estimación de movimiento. Las principales mejoras introducidas incluyen la reducción de la sensibilidad de la estimación a contaminación por bajas frecuencias, ruido y grandes desplazamientos entre imágenes consecutivas. El último artículo presenta ORI-O-CSPAMM, una nueva secuencia de imágenes de RM de tagging que permite la adquisición de grillas de CSPAMM y MICSr en la mitad del tiempo de escaneo en comparación con la secuencia CSPAMM y ORI-CSPAMM. Además, permite remover los artefactos de off-resonance generados durante la preparación de la grilla, lo que es útil en presencia de grasa.

Las tres investigaciones presentan mejoras a tres partes esenciales de la estimación de deformaciones cardíacas, incluyendo la secuencia y los parámetros de adquisición y la técnica de procesamiento.

**Palabras Claves:** RM Cardiovascular, RM Cardíaca, RM de Tagging, Deformaciones Cardíacas, Estimación de Movimiento.

## 1. INTRODUCTION

Cardiovascular diseases are one of the leading causes of death globally (World Health Organization, 2018). Most of these diseases involve myocardial dysfunction, whose signs and symptoms are often called Heart Failure (HF) (Adamczak et al., 2020). HF has been progressively recognized as an epidemic, and its incidence in developing and developed countries keep growing, with a prevalence of 1.1-5.5% in the general population.

The Ejection Fraction (EF), defined as the ratio of the stroke volume<sup>1</sup> and the end-diastolic volume of the Left-Ventricle (LV), is the cornerstone in the diagnosis of HF and has been extensively used (Cikes & Solomon, 2016). Depending on the EF, the HF is subclassified into three ranges: HF with reduced EF (HFrEF;  $EF < 40\%$ ), HF with mid-range EF (HFmrEF;  $40 \leq EF < 50\%$ ), and HF with preserved EF (HFpEF;  $EF \geq 50\%$ ) (Ponikowski et al., 2016). These ranges characterize different diseases with different outcomes in terms of myocardial function, including systolic malfunction in the case of HFrEF and HFmrEF patients, and diastolic dysfunction for HFpEF.

HFpEF was discovered in 1982 and described a group of patients with typical HF symptoms and preserved Left-Ventricular EF (LVEF). Recent studies suggest that the prevalence of HFpEF is increasing at a rate of 1% annually relative to HFrEF, which means that HFpEF is becoming the most common type of HF (Owan et al., 2006; Adamczak et al., 2020). This is particularly important, as most of the diseases inducing HFpEF cannot be detected at the early stages of development, which is crucial for assessing the affections.

Furthermore, EF suffers from several issues that affect its reproducibility and predictive capability, including but not limited to preload and afterload dependency, geometric assumptions, and the presence of pre-existent diseases such as hypertension, diabetes, and renal malfunction (Cikes & Solomon, 2016). Therefore, the use and development of more robust biomarkers with high sensitivity to early cardiac function changes has increased

---

<sup>1</sup>Volume of blood ejected by the left-ventricle at end-systole.

in the past years. In this context, cardiac strain, which is a measure of the tissue's local deformation, plays a fundamental role.

The cardiac strain has been used to assess HF in early and later development stages, including diseases that develop with preserved EF. Cardiac strain has found several applications in later stages of disease development: discriminating dysfunction in patients with myocardial infarction, differentiating patients with idiopathic dilated cardiomyopathy, differentiating active from passive contraction in patients with ischemia, as a predictive index of the extent of transmural infarction, detecting and assessing cardiac dyssynchrony in patients with left bundle branch ablation and HF with narrow QRS, and as a predictive value of the response in cardiac resynchronization therapy (among others) (Götte et al., 2001; MacGowan et al., 1997; Gorcsan & Tanaka, 2011; Budge et al., 2012).

Also, cardiac strain has found useful applications in the early stages of diseases in diagnosing patients with hypertrophic cardiomyopathy with normal or increased EF; assessing the cardiac function in patients with Type 2 Diabetes Mellitus, diastolic dysfunction, and normal EF; and differentiating patients with Duchenne muscular dystrophy (characterized by progressive cardiac dysfunction and myocardial fibrosis late in the disease process) and normal EF at any progression stage of the disease (A. A. Young, Kramer, Ferrari, Axel, & Reichek, 1994; Fonseca et al., 2004; Hor et al., 2009).

Lately, cardiac strain has been used to generate maps of the LV mechanical activation in HF and evaluate its implications in cardiac resynchronization therapy, as a predictor of major adverse cardiac events following an acute myocardial infarction, and to detect post-chemotherapy cardiotoxicity (changes in the cardiac function produced by chemotherapy) in long-term survivors of breast cancer (Auger et al., 2017; Mangion et al., 2019; Kar, Cohen, McQuiston, Figarola, & Malozzi, 2019).

Cardiac strain estimation has become non-invasively available in the late 1980s with the development of Tagging MRI (Reichek, 2017) and since 2004, with the introduction

of echocardiographic Speckle Tracking (Leitman et al., 2004). Since then, many acquisition and image processing techniques for echocardiography and MRI, which allow tissue deformation estimation, have been developed. Since the first evaluations in cardiac diseases and HF, cardiac strain has been a robust biomarker, highly reproducible, and more sensitive to subtle cardiac function variations than EF.

In this thesis, novel MRI acquisition and processing techniques for assessing the cardiac strain were developed to improve issues related to the quantification process. First, a comparison between processing methods to estimate cardiac strain was performed to study the pros and cons of current methods. Second, a new and more robust processing technique was developed to obtain better strain estimations from tagged MR images. Finally, a novel acquisition sequence was introduced to acquire improved tagged MR images in half of the scan time compared to CSPAMM sequences.

## **1.1. Overview**

This thesis is structured as follows: in Section 1.2, the physical principles of MRI are explained. In Sections 1.3 and 1.4, a review of MRI sequences and processing techniques to estimate cardiac motion and strain are presented and their main limitations are mentioned. In Section 1.5, the formal definition of cardiac strain is given. In Section 1.6, the main and specific objectives, the hypothesis, and also the methodology of this research are introduced.

In Chapter 2, the first publication is presented. In this research, three state-of-the-art motion estimation techniques used on two kinds of MR images were interrogated and compared under different imaging conditions to evaluate their performance.

In Chapter 3, the second publication is given. In this investigation, a new motion estimation technique, more robust to low-frequency artifacts and improved temporal consistency, is introduced and tested on synthetic and in-vivo data of healthy and unhealthy volunteers and compared against two current techniques.

In Chapter 4, the third article is provided. In this work, a new acquisition sequence of tagged MR images, which allows the measurement of high-quality images without off-resonance artifacts in reduced scan-time and allows magnitude reconstructions, was developed.

Finally, in Chapters 5 and 6, the current work's perspectives and the conclusions of this research are listed and discussed.

## **1.2. Physical principles of MRI**

The Magnetic Resonance (MR) phenomenon is based on an external magnetic field's interaction with the protons of the atom's nucleus. Suppose the number of protons and the atomic weight of a nucleus are odd. In that case, its magnetic moment interacts with the magnetic field due to its electrical charge and spin (the intrinsic angular momentum of the proton). The human body comprises several nuclei with suitable characteristics to interact with magnetic fields. However, the hydrogen nucleus made up of a single proton (i.e.,  $^1\text{H}$  nucleus) is the most abundant. Therefore, MR focuses mainly on imaging the  $^1\text{H}$  nucleus.

In the MR context, the spin of atomic or subatomic particles is a fundamental property that represents the ability of a nucleus to interact with electromagnetic fields, and like the angular momentum, it is represented by an arrow (see Fig. 1.1). Unlike macroscopic properties, the spin (denoted by the letter  $I$ ) can only be measured in discrete integer or half-integer units (0, 1/2, 1, 3/2, 2, 5/2, ...), and only nuclei with non-zero spins can resonate while interacting with an external magnetic field. The  $^1\text{H}$  nucleus and the single proton conforming it have a spin of 1/2, which makes it suitable for MR applications.

### **1.2.1. Magnetization**

The MR measurement is generated by a set of hydrogen atoms rather than individual atoms. In the absence of a magnetic field, the protons in a tissue containing hydrogen

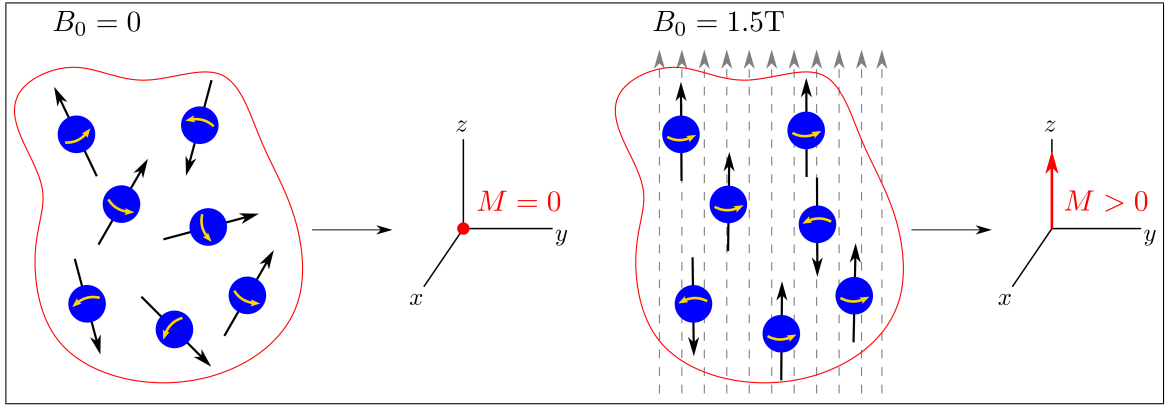


Figure 1.1. A group of hydrogen spins share the same magnetic moment but randomly oriented in the absence of an external magnetic field ( $B_0 = 0$ ), which leads to a zero net magnetization  $M$ . After applying a strong magnetic field ( $B_0 = 1.5\text{T}$ ), the spins align with the magnetic field, resulting in a non-zero net magnetization.

atoms have spins with the same magnitude oriented randomly in several directions (see Fig. 1.1). Therefore, the vectorial addition of all the spins leads to a zero-sum or no net magnetization. If an external magnetic field  $B_0$  is applied to the tissue, the hydrogen atoms align with the magnetic field leading to a net magnetization  $M$ . The interaction between the external magnetic field and the hydrogen nucleus spins makes the individual protons start to precess around  $B_0$  with a frequency given by

$$f_L = \frac{\gamma B}{2\pi} \quad (1.1)$$

The Larmor frequency  $f_L$  is a fundamental property of the nucleus and depends on the gyromagnetic constant  $\gamma$  and the external magnetic field  $B$ . For instance, on a MR scanner with main magnetic field of  $B = 1.5$  Tesla (T), for the hydrogen nucleus  $\gamma/(2\pi) = 42.58 \times 10^6$  Hz/T and the Larmor frequency is  $f_L \approx 64$  MHz (in the same range of FM radio signals).

As it will be discussed later, for the generation of MR images, small spatial variations are induced on the magnetic field  $B$  to change the precession frequency at different spatial locations of the tissue, which are then measured to form images. Thus, the expression given in Eq. 1.1 is fundamental to MRI.

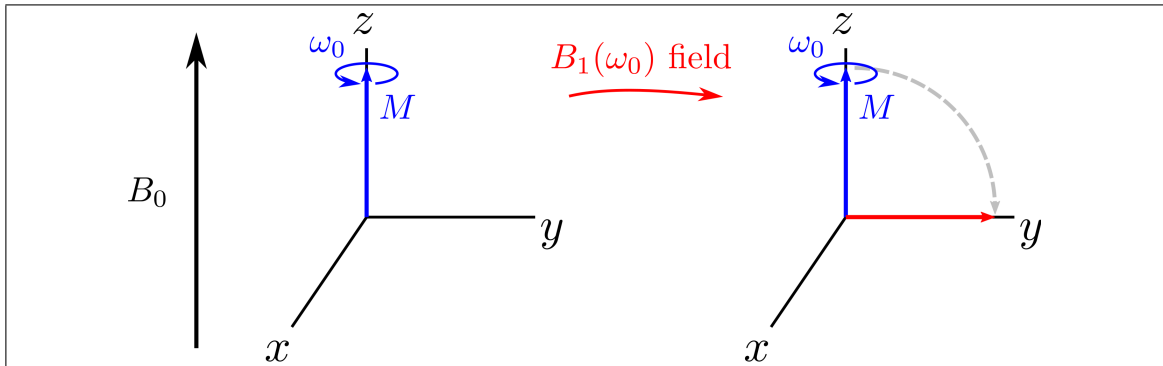


Figure 1.2. In presence of a strong  $B_0$  field, the net magnetization vector is aligned with this field and precess with an angular frequency  $\omega_0$ . After the application of a  $90^\circ$  RF pulse ( $B_1$  field) with central frequency  $\omega_0$ , the magnetization vector is not longer aligned with  $B_0$

### 1.2.2. RF excitation

The signal detection in MR is based on an energy transfer principle. Before the detection, the  $^1\text{H}$  nuclei in the tissue are excited by a radiofrequency (RF) pulse with central frequency  $f_L = \gamma B_0 / 2\pi$  (note that  $B$  in Eq. 1.1 was replaced by the main magnetic field of an MR scanner  $B_0$ ). The energy of the RF pulse is absorbed by the tissue, re-emitted, and measured by the MR scanner.

The RF pulse is a less powerful magnetic field denoted as  $B_1$ , which is applied perpendicular to  $B_0$  to allow the energy transfer to the protons and the rotation of the magnetization vector out of the equilibrium and away from the  $B_0$  direction. In the presence of a strong magnetic field, the magnetization vector aligns with the  $B_0$  axis (usually referred to as  $z$ -axis), and the spins precess with the Larmor frequency. As the precessing is incoherent, there is no net magnetization in the  $x - y$  plane. After the application of  $B_1$ , the magnetization is rotated into the  $y$ -axis, generating a net magnetization in the transverse ( $x - y$ ) plane (see Fig. 1.2). The rotation angle (i.e., the amount of transverse net magnetization) depends on the strength and duration of  $B_1$  (for instance, in Fig. 1.2, a  $90^\circ$   $B_1$  field was used, which fully rotated the magnetization vector into the transverse plane).

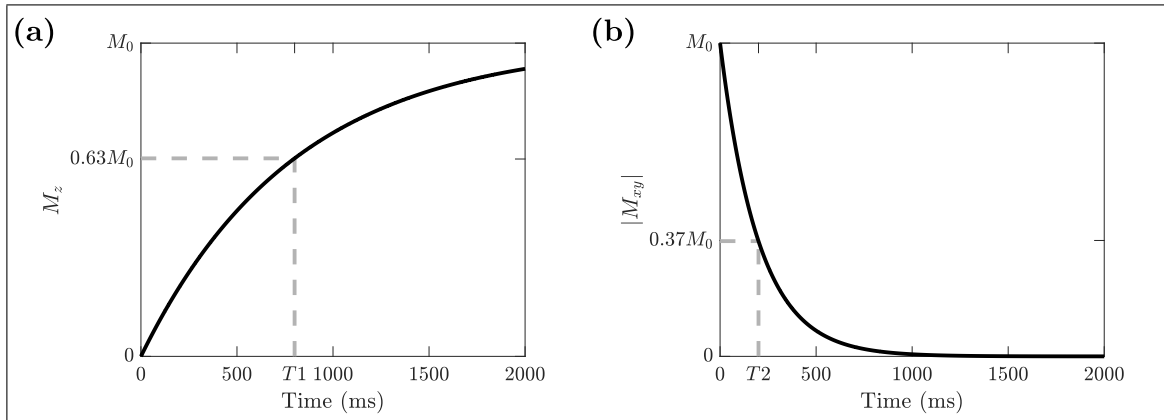


Figure 1.3. (a) T1 and (b) T2 relaxation curves

When the  $B_1$  field is turned off, the  $^1\text{H}$  protons will tend to the equilibrium state, aligning with the  $B_0$  field. During the previous process, the net magnetization on the  $x - y$  plane precesses around  $B_0$ , emitting energy at a frequency  $f_L$ . Suppose a loop of wire is placed perpendicular to the transverse ( $x - y$ ) plane. The precessing magnetization vector will induce a voltage in a phenomenon denoted Free Induction Decay (FID) by Faraday's induction law. The FID is the received MR signal used to generate the images, and the loop of wire is the receiver, often called the receiver coil.

### 1.2.3. Relaxation

The relaxation process describes how the magnetization vector returns to the equilibrium after applying a RF pulse. The recovery of the magnetization in the longitudinal ( $z$ ) axis is characterized by the  $T_1$  relaxation (also called spin-lattice relaxation) time. The decay of the magnetization in the  $x - y$  plane is characterized by the  $T_2$  relaxation (also called spin-spin relaxation) time.

#### T1 relaxation

After the application of a  $90^\circ$  RF pulse, the magnetization  $M_0$  is fully rotated into the transverse plane (see Fig. 1.2), resulting in a zero net magnetization in the longitudinal direction ( $z$ -axis). Once the RF pulse is turned-off, the magnetization tends to the

equilibrium and recovers its longitudinal component exponentially with:

$$M_z(t) = M_0(1 - e^{-t/T1}) \quad (1.2)$$

where  $t$  is the time after the RF pulse application, and  $T1$  the time that takes to recover 63% of the longitudinal magnetization (see Fig. 1.3).

### **T2 relaxation**

After the application of a  $90^\circ$  RF pulse, all the magnetization  $M_0$  is placed in the transverse plane, resulting in a  $M_{xy}$  magnetization equals to  $M_0$ . Once the  $B_1$  field is turned-off, the transverse magnetization start to decay exponentially to zero:

$$M_{xy} = M_0 e^{-t/T2} \quad (1.3)$$

where  $t$  is the time after turning off the RF pulse, and the  $T2$  the time that takes the magnetization to decay 37% of its original value (see Fig. 1.3).

#### **1.2.4. Spatial encoding of the image**

Spatially varying magnetic gradients are applied to change the precession frequency of the spins locally, generating a FID signal that depends on the magnetic gradients, i.e., the spatial position. By applying magnetic gradients with different magnitudes and durations, multiple spatially varying FID signals can be measured, which are used to generate the image.

### **Magnetic gradients**

Magnetic gradients are coils within the scanner that are used to spatially encode the MR signal. These gradients produce small variations of the static  $B_0$  field (typically less than 1% of the total magnetic field). The gradients can be varied in the  $x$ -,  $y$ -, and  $z$ -directions with strengths<sup>2</sup>  $G_x$ ,  $G_y$ , and  $G_z$ , respectively, generating a magnetic field

<sup>2</sup>The strength of the magnetic gradients is usually measured in *militesla per meter* ( $\text{mT m}^{-1}$ ).

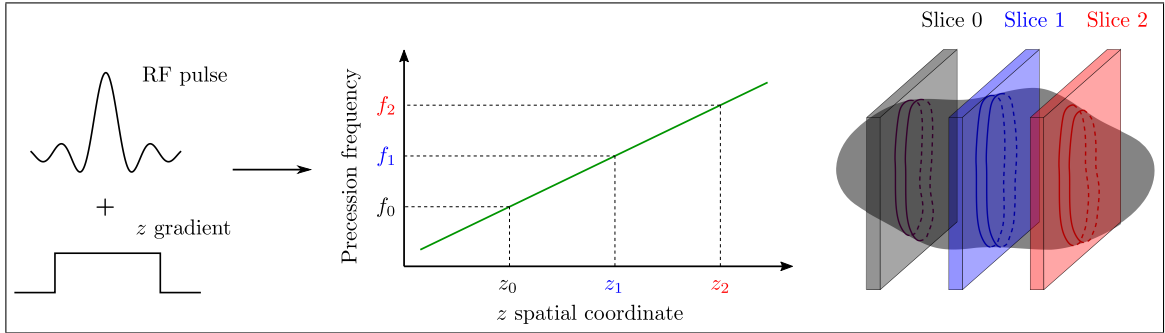


Figure 1.4. After the application of a RF pulse combined with a slice-selective  $z$ -gradient, the precession frequency of the tissue vary linearly with the  $z$  position. Depending on the central frequency of the RF pulse, thin slices in different  $z$  locations can be excited. For instance, if the RF pulse has central frequency  $f_0$ , only the magnetization vectors inside the thin Slice 0 are excited.

that depends linearly on the gradients:

$$B_z(x, y, z) = B_0 + G_x x + G_y y + G_z z \quad (1.4)$$

The  $B_z$  field generates a spatially varying Larmor frequency given by:

$$f_L(x, y, z) = \frac{\gamma}{2\pi} (B_0 + G_x x + G_y y + G_z z) \quad (1.5)$$

which makes the protons resonate at different frequencies depending on its position. By changing the gradient strength and taking multiple measurements, information about one spatial location at multiple frequencies can be obtained.

### Slice selection (encoding in $z$ -direction)

The first step in acquiring a MR image is to localize the signal in one of the spatial dimensions ( $z$ - or slice-direction). This is done by the combination of a  $B_1$  field and magnetic gradient in a process called slice-selective excitation. After the application of a magnetic gradient in the  $z$ -direction, the precession frequency vary with the spatial location within the magnet:

$$f_L(x, y, z) = \frac{\gamma}{2\pi} (B_0 + G_z z) \quad (1.6)$$

The slice selection is when just the magnetization of a thin slice of tissue is tipped to the transverse plane. The last is done by tuning the central frequency and bandwidth ( $BW$ ) of the  $B_1$  field to values corresponding to different tissue locations (see Eq. 1.6) and slice thicknesses. Thus, only spins with precession frequency within the range  $f_L \pm BW$  are excited. After the excitation, the transverse plane's spins are dephased because they did not experience the same magnetic field, and a rephasing gradient is applied to regain its initial phase. However, in some MR applications, the whole volume (slices with infinite thickness) is excited in a process called non-selective RF excitation, which is often used in contrast preparation.

Although the selective RF excitation was described only in the  $z$ -direction, by combining the magnetic gradient fields in two or more directions, slices can be positioned in any arbitrary orientation.

### **Frequency encoding (encoding in x-direction)**

During the frequency encoding (readout), a magnetic gradient is applied in the  $x$ -direction to localize the FID signal spatially. In the readout, the spins precess at different frequencies based on their location in the  $x$ -direction (see Fig. 1.5a). The signal measured by the receiver is a superposition of these frequencies, which contains information on the localization of protons in the  $x$ -direction (see Fig. 1.5b). The measured FID signal is related with the image through the Fourier transform, as will be discussed later.

The signal measured by the scanner is continuous in time, but due to the discrete nature of the hardware, it is sampled at a specific frequency. The Nyquist sampling theorem states that a continuous signal can be reconstructed from uniformly spaced samples if the samples are taken at a rate that is twice the signal's bandwidth. Thus, during the acquisition, the user specifies the bandwidth defining the field-of-view ( $FOV_x$ ) and the number of samples ( $N_x$ ) in the  $x$ -direction to fulfill the Nyquist theorem (the pixel size is given by  $\Delta x = FOV_x/N_x$ ).

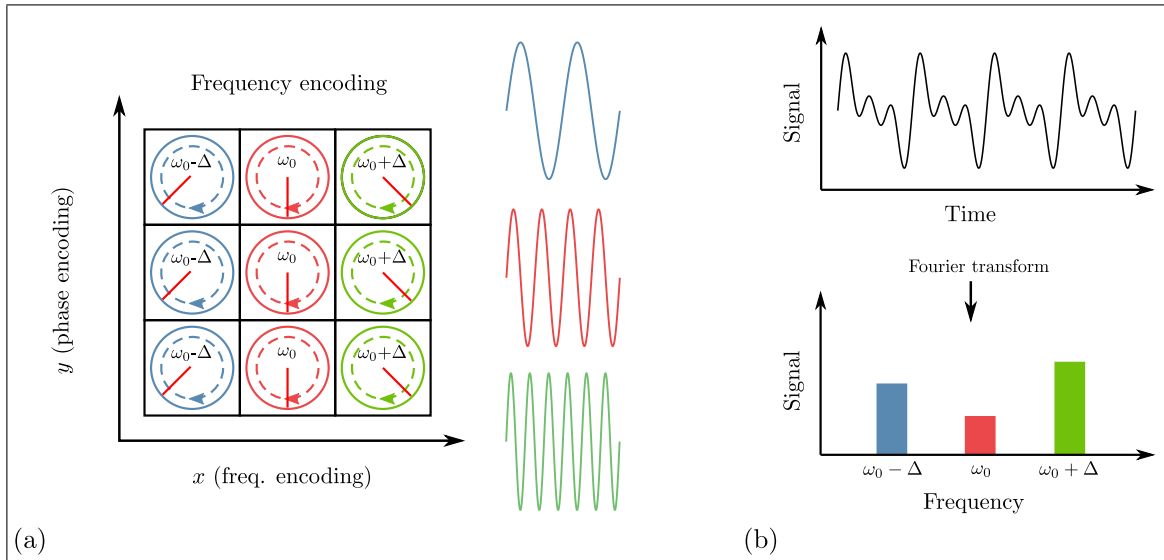


Figure 1.5. (a) During the readout (the application of a frequency encoding gradient), the spins precess at different frequencies based on their spatial location in the  $x$ -direction, generating different signals. (b) The signal that is being readout is a superposition of these signal and it is used to locate the protons in the  $x$ -direction.

### Phase encoding (encoding in $y$ -direction)

The phase encoding is the final step to localize the final spatial dimensions. During the phase encoding, a magnetic field gradient is applied in the  $y$ -direction (phase direction) after the slice selection and before the frequency encoding. After the slice-selective excitation, the spins precess at a frequency given by  $f_L = \gamma B_0 / (2\pi)$ . With the application of a phase-encoding gradient  $G_y$ , the protons experience a different precession frequencies based on their  $y$ -location according to  $f_L = \gamma / (2\pi) (B_0 + G_y y)$ . When  $G_y$  is turned-off, the spins recover their original frequency but they are now dephased (see Fig. 1.6). The different phases of the spins depends on their  $y$ -location, the strength of  $G_y$ , as well as its duration, and are used to localize the protons in the  $y$ -direction.

Similar to frequency encoding, the user defines the field-of-view ( $FOV_y$ ) and the number of samples ( $N_y$ ) in the  $y$ -direction during a MR scan (the pixel size is given

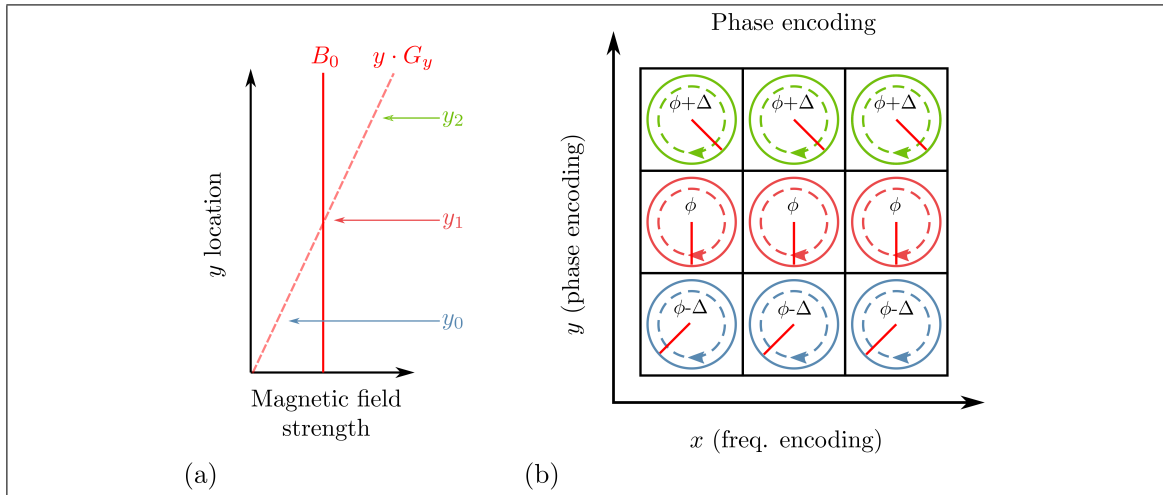


Figure 1.6. (a) During the application of the phase-encoding gradient ( $G_y$ ), each spin is subject to a spatially varying magnetic field  $B_0 + y \cdot G_y$ , which makes it to precess at different frequencies. (b) After turning-off the gradient, the spins regain their original frequencies but are dephased in the  $y$ -direction.

by  $\Delta y = FOV_y/N_y$ ). However, unlike frequency encoding, each sample in the phase-encoding direction is sampled in separate measurements, increasing the scan time if the chosen  $N_y$  is large.

The slice selection, frequency-, and phase-encoding are the main ingredients to obtain a MR image, and are combined into an acquisition sequence (Fig. 1.7a).

### 1.2.5. The signal equation

The MR signal scanned during an exam contains the protons information encoded based in their spatial location. These signal can be viewed as points in the  $k$ -space. The  $k$ -space corresponds to the spatial frequency content of the image, i.e., the Fourier transform of the image (see Fig. 1.7b). Each location in the  $k$ -space is defined by the frequency

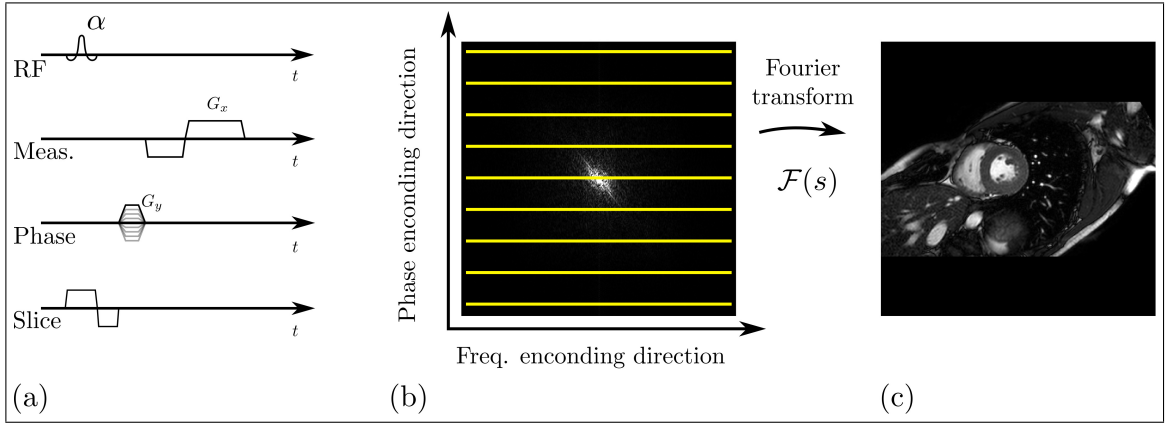


Figure 1.7. (a) The combination of the slice selection, and frequency and phase encodings define an acquisition sequence. (b) The MR signal is acquired in the  $k$ -space, which denotes the image in the Fourier domain. (c) After the application of the inverse Fourier transform, the image is recovered.

and phase encoding gradients:

$$k_x = \frac{\gamma}{2\pi} \int_0^T G_x(\tau) d\tau \quad (1.7a)$$

$$k_y = \frac{\gamma}{2\pi} \int_0^T G_y(\tau) d\tau \quad (1.7b)$$

where  $\gamma$  denotes the gyromagnetic constant,  $T$  the duration of the magnetic gradients  $G_x$  and  $G_y$  (the total time in which the gradients were turned-on), and  $k_x$  and  $k_y$  the spatial frequencies (with units usually measured in Hz/m).

The  $k$ -space formalism given in Eq. 1.7 allows to represent the measured signal by the Fourier transform of the object being scanned, which is defined by:

$$s = \int_{\mathbf{r}} M_{xy}(\mathbf{r}) \exp(-i2\pi\mathbf{r} \cdot \mathbf{k}) d\mathbf{r} \quad (1.8)$$

where  $M_{xy}$  denotes the transverse magnetization of the object and  $\mathbf{k} = (k_x, k_y)$  the  $k$ -space locations, and  $\mathbf{r} = (x, y)$  the object position. With the previous definition, the magnetization of the object being measured is reconstructed using the inverse Fourier

transform (see Fig. 1.7c):

$$M_{xy} = \mathcal{F}^{-1}(s) \quad (1.9)$$

### 1.3. Tagging Magnetic Resonance Imaging

Tagging MRI is an acquisition technique in which, a grid pattern generated over the tissue at the beginning of the cardiac cycle (by a selective saturation of the tissue in the form of lines) follows the cardiac motion (see Fig. 1.8), allowing the tracking of the cardiac walls with temporal resolutions in the range of 30 to 50 msec. At the beginning of the cardiac cycle, grid-lines in tagged images are parallel and equispaced. In the spatial frequency domain, this behavior is expressed as several spectral peaks with harmonic frequencies, which become wider due to the tissue contraction and energyless as the magnetization relaxes. Several techniques have been developed to acquire tagged MR images<sup>3</sup>.

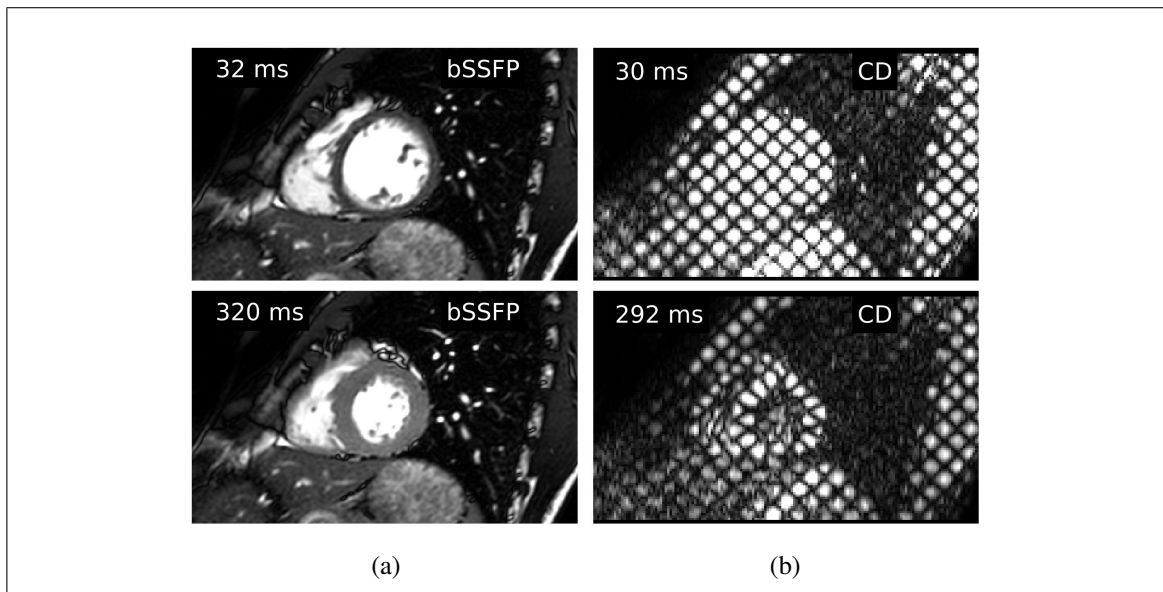


Figure 1.8. (a) Anatomical and (b) tagged MR images of a short-axis LV slice of the heart for an end-diastolic (upper row) and end-systolic (bottom row) cardiac phase.

<sup>3</sup>It must be noticed that cardiac strain cannot be estimated directly from tagged MR images, and other processing techniques must be applied. Nonetheless, in the following paragraphs, Tagging MRI sequences are explained and revisited. Processing techniques to estimate cardiac strain are described immediately after.

One of the earlier approaches combined a series of selective Radio-Frequency (RF) pulses to create saturation bands on the cardiac tissue (Zerhouni, Parish, Rogers, Yang, & Shapiro, 1988), which allowed following the myocardium's motion. However, the time required to generate a proper amount of stripes was elevated and did not allow finer grids. A year later, the Spatial Modulation of Magnetization (SPAMM) was introduced (Axel & Dougherty, 1989a), which employed a position encoding gradient and two non-selective RF pulses to rapidly saturate the magnetization, allowing images with sinusoidal intensity profile. High-order SPAMM was introduced in the same year (Axel & Dougherty, 1989b), and distributed the gradients and RF pulses accordingly with the coefficients of the binomial sequence to obtain sharper stripes. The last two remain as the most used Tagging MRI techniques and have commercial implementations in multiple vendors.

A significant improvement was made with the Complementary SPAMM (CSPAMM) sequence (Fischer, McKinnon, Maier, & Boesiger, 1993), which used two SPAMM acquisitions to remove the non-tagged signal from the image at the cost of doubling the acquisition time. The last permitted to improve the tagging contrast through the cardiac cycle. A Slice-Following CSPAMM (SF-CSPAMM) acquisition was introduced a year later (Fischer et al., 1994). Using a slice-selective tagging preparation and excitation, SF-CSPAMM allowed for the first time imaging the true myocardial motion by correcting the through-plane cardiac displacement. Despite the improved capabilities, both CSPAMM and SF-CSPAMM share time restrictions, requiring four images to measure a 2D grid, while SPAMM only needs one.

In the late 1990s, the Displacement-Encoded with Estimated Echoes (DENSE) acquisition sequence was introduced (Aletras, Ding, Balaban, & Wen, 1999). In DENSE MRI, the tissue motion is encoded into the complex image phase by using a position encoding and decoding magnetic gradient, allowing the direct estimation of motion. DENSE MRI shares similar characteristics with SPAMM, CSPAMM, and SF-CSPAMM in the following sense: (1) the same SPAMM tagging prepulse is used to position-encode the tissue

at the beginning of the cardiac cycle. (2) Unwanted spectral peaks are removed by acquiring a complementary DENSE acquisition in the so-called Phase-Cycling approach (Kim, Gilson, Kramer, & Epstein, 2004). And (3), Slice-Following DENSE MRI is used to measure true myocardial motion (Spottiswoode et al., 2008). However, DENSE MRI needs five images to measure 2D motion (four position encoded and one reference).

Cardiac strain is estimated by applying complex processing methods to tagged MR images, many times involving elevated processing times. These issues were surpassed with the introduction Strain-Encoded (SENC) MRI (Osman, Sampath, Atalar, & Prince, 2001), which allowed measuring strain directly from the image. In SENC MRI, a simple calculation on two SPAMM images with position encoding gradients orientated in a direction perpendicular to the image plane and with different phase encodings allows the estimation of a dense strain map. The strain is measured in the same direction of the applied gradients and, i.e., in the orthogonal direction of the image plane. To obtain fully 2D strain maps, SENC MRI requires four images, making it similar to CSPAMM in terms of acquisition times.

MRI images are prone to off-resonance effects, which, in tagged MR images, are visible as distorted or curved stripes in the absence of motion. A modified CSPAMM sequence was introduced later to fix the off-resonance effects produced by fat, which worked inverting the tagging gradient in the second SPAMM image and adjusting its duration (Fahmy, Basha, & Osman, 2009). This sequence was generalized five years later with the development of the Off-Resonance Insensitive CSPAMM (ORI-CSPAMM) acquisition, which corrected the off-resonance effects produced not only by fat but also by other chemical species (Reyhan, Natsuaki, & Ennis, 2014).

Almost in parallel, Orthogonal CSPAMM (OCSPAMM) was introduced to reduce the acquisition time of CSPAMM grids. In this sequence, two complementary SPAMM acquisitions with orthogonal tagging gradients (instead of the four needed with CSPAMM) are used to generate a CSPAMM grid after complex subtraction (H. Wang et al., 2011).

Many of the MRI sequences mentioned before have been extended to allow 3D acquisitions, i.e., they can measure a volume instead of 2D slices. Some examples are 3D SPAMM, 3D CSPAMM, Accelerated 3D CSPAMM, and Volumetric Spiral Cine DENSE MRI, which have been used to assess the left-, right-, and bi-ventricular cardiac function (A. A. Young & Axel, 1992; Haber, Metaxas, & Axel, 2000; Ryf, Spiegel, Gerber, & Boesiger, 2002; Rutz, Ryf, Plein, Boesiger, & Kozerke, 2008; Zhong, Spottiswoode, Meyer, Kramer, & Epstein, 2010).

Although the previously mentioned MRI sequences have been successfully used to estimate cardiac strain, they suffer from mainly two issues: first, all of them suffer from off-resonance artifacts generated during the preparation pulses and the readout (Fahmy et al., 2009; Reyhan et al., 2014). Second, many of them (CSPAMM, SF-CSPAMM, ORI-CSPAMM, DENSE, and 3D versions) are not applicable to clinical setups due to high acquisition times. Therefore, new improvements must be developed to overcome these issues.

#### **1.4. Motion estimation techniques from tagged MR images**

Cardiac strain cannot be estimated directly from tagged MR images, and motion estimation techniques must be applied. Motion processing techniques can be divided into two groups: those based on the image intensity and those based on the k-space<sup>4</sup>. In the first group, taglines tracking, optical flow, and image registration methods (which use intensity models and brightness or biomechanical constraints) are found. In contrast, the second is composed of those based on the identification and filtering of the harmonic spectral peaks.

One of the earlier approaches used optical flow to estimate the tissue velocity from synthetic and in-vivo 2D tagged MR images of a phantom, which was used later to estimate the underlying displacement field recursively (Prince & McVeigh, 1992). A few years later, an image registration problem was solved using the active contours to estimate 3D

---

<sup>4</sup>The image representation in the k-space is obtained by taking the Fourier transform of the image.

motion from a set of orthogonal Short-Axis (SA) and Long-Axis (LA) tagged MR images. The cardiac strain was calculated after motion interpolation using the Finite Elements Methods (FEM) (A. A. Young, Kraitchman, Dougherty, & Axel, 1995). Physic-based deformable models were used to parameterize the cardiac geometry and motion one year later, which used Lagrangian dynamics to convert the geometric model to an equivalent dynamic model deformed by external forces to estimate strain. Similar to the previous method, 3D motion was estimated from a set of SA and LA tagged MR slices of the heart (Park, Metaxas, Young, & Axel, 1996; Park, Metaxas, & Axel, 1996). The last method was extended later by using a Cascaded SPAMM acquisition, which allowed the LV motion estimation with full cardiac cycle coverage (Park, Metaxas, Axel, Yuan, & Blom, 1999).

B-splines have also been used for taglines localization and tracking of combined SA and LA tagged MR data. Deformable B-solids, defined in terms of a 3D tensor product B-spline, were used to localize and track the taglines of the tagged MR images. The cardiac motion was estimated by solving an energy minimization problem (Radeva, Amini, & Huang, 1997). Similarly, B-snake grids (a grid formed by a set of B-splines) were used to estimate the displacements at the tag intersections, and constrained thin-plate spline interpolation was used to obtain a dense map of displacements (Amini, Chen, Curwen, Mani, & Sun, 1998). A 4D B-spline model was proposed later for the spatio-temporal tracking of myocardial deformation also from combined SA and LA images. A time-varying B-spline model was used to localize the tag-planes, extract a set of material points, and reconstruct the displacement field in a single-step procedure (Huang, Abendschein, Dâvila-Român, & Amini, 1999), which had better interpolation properties than previous B-spline methods.

Another method was introduced later to track a sparse set of material points through the whole cardiac cycle. Tag-planes were recovered using thin-plate splines at each frame, and the intersection points of three perpendicular planes were defined as the material points. The time-varying position of each material point was used to calculate the tissue motion

(Kerwin & Prince, 1998). The Model Tags method was developed a year later to overcome the long processing times required for most techniques. Model Tags allowed the direct 3D tracking of cardiac motion from orthogonal SA and LA tagged MR slices by using a FEM mesh for the geometric model, which included material surfaces to mimic the tag-planes. The match between the mesh with the images was done through a constrained optimization problem imposing the likelihood between the mesh's material surfaces and the tag-planes. The processing time was reduced from 45 min/frame to 5 min/frame compared to other methods (A. A. Young, 1999).

In the late 1990s, the Harmonic Phase analysis (HARP) was introduced, allowing the automation of estimating motion and strain from tagged MR images. HARP method is a k-space-based technique in which the first harmonic spectral peak is bandpass-filtered to obtain a harmonic image whose phase contains the tissue's position. The phase is treated as a material property moving accordingly with the tissue, i.e., material points keep their phase through the cardiac cycle. The last assumption is used to track the tissue's material points into a deformed state by solving an optimization problem (Osman, Kerwin, McVeigh, & Prince, 1999; Osman, McVeigh, & Prince, 2000). The development of the HARP algorithm marked a milestone in the history of cardiac motion estimation, and until today remains as one of the most used techniques.

Peak-combination HARP was published a few years later to correct artifacts in the harmonic phases produced by unwanted variations in the scanner's main magnetic field (Ryf, Tsao, Schwitter, Stuessi, & Boesiger, 2004). HARP only uses the first negative or positive spectral peak to obtain the harmonic phases, while peak-combination HARP uses either the positive and negative. However, peak-combination HARP reaches its optimum performance with CSPAMM images, i.e., images without non-tagged signal.

ZHARP was introduced the next year to obtain 3D motion from 2D CSPAMM images. ZHARP is both a new processing method and a new acquisition sequence (Abd-Elmoniem, Stuber, Osman, & Prince, 2005). Trough-plane motion is encoded into the images by modifying the CSPAMM sequence adding a position encoding gradient through the Z

direction to each SPAMM image. Then, harmonic phases are obtained by solving a linear system of equations after applying four bandpass filters to the first negative and positive spectral peaks in the X and Y directions.

Another family of k-space-based technique is the Gabor filter banks. A Gabor filter has the form of a sinusoidally modulated Gaussian, and it is mostly used for texture analysis applications. A set of Gabor filters with different central frequencies and bandwidths called Gabor Filter Banks have been used for tagline detection and motion estimation from tagged MR images. Deformable models combined with Gabor filter banks and spatio-temporal constraints were used to automatically segment the myocardial geometry and estimate cardiac strain from 3D tagged MR images (T. Chen & Axel, 2006). A similar work was done to detect and track the tag-planes of 3D tagged MR images using Gabor filter banks (Qian, Metaxas, & Axel, 2006). Similar to the previous methods, Gabor filter banks, robust point matching, and deformable models were used to find the tag intersections, sparsely track the tissue motion, and obtain a dense motion map, respectively (T. Chen, Wang, Chung, Metaxas, & Axel, 2010). This last methodology allowed the automated estimation of 3D motion and strain from 3D tagged MR images.

Another improvement of HARP was made with Extended HARP, which fixed tracking issues suffered by the original method (Tecelão, Zwanenburg, Kuijjer, & Marcus, 2006). During the acquisition of tagged MR images, the tissue near cardiac borders goes in and out of the imaging plane, making the harmonic phase appear and disappear from one frame to another. This produces mistracking near the boundaries. Extended HARP added additional constraints to the tracked points to fix the issue mentioned before, allowing the estimation of a more accurate and representative motion of the LV.

With the advances in computation capacity, the non-rigid image registration problem has become more available to estimate cardiac motion (Chandrashekar, Rao, Sanchez-Ortiz, Mohiaddin, & Rueckert, 2003; Ledesma-Carbayo et al., 2008; Li, Young, & Cowan, 2008). Moreover, the registration problem has been enriched via regularization or data assimilation using biomechanical models and MRI observations to improve the tracking

outcome (Genet, Stoeck, von Deuster, Lee, & Kozerke, 2018; Škardová, Rambašek, Chabiniok, & Genet, 2019), allowing the estimation of cardiac motion as well as other mechanical parameters.

Feature Tracking (FT) is another processing technique used to obtain motion and strain using tagged MR images that can also be applied to anatomical images (Claus, Omar, Pedrizzetti, Sengupta, & Nagel, 2015). FT is based on tracking the intensity features of the images using image registration algorithms with proper regularization schemes. Recent advances in FT are based on hyperelastic regularization to penalize the deviation from the mechanical equilibrium instead of penalizing the kinematic (Genet et al., 2018). This leads to results that are physically consistent with the mechanical behavior of the cardiac tissue.

Nevertheless, it has been demonstrated that FT performs well obtaining global metrics of the heart but poorly locally (Morton et al., 2012; Wehner et al., 2018). For this reason, FT was not considered in this investigation as regional strain measurements are relevant to detect subtle changes in cardiac function.

Overall, most of the techniques mentioned previously suffers from at least one of the following issues:

- (i) High operator-dependency and elevated interaction times.
- (ii) Elevated processing times (computational expensiveness).
- (iii) DC (low frequencies) contamination.
- (iv) Signal decay.
- (v) Missestimation due to through-plane motion.
- (vi) Missestimation due to large frame-to-frame motion.
- (vii) Missestimation of local deformations (in the case of non-rigid registration methods).

Therefore, new strategies must be developed to surpass these issues.

### 1.5. Biomechanical quantification using cardiac strain

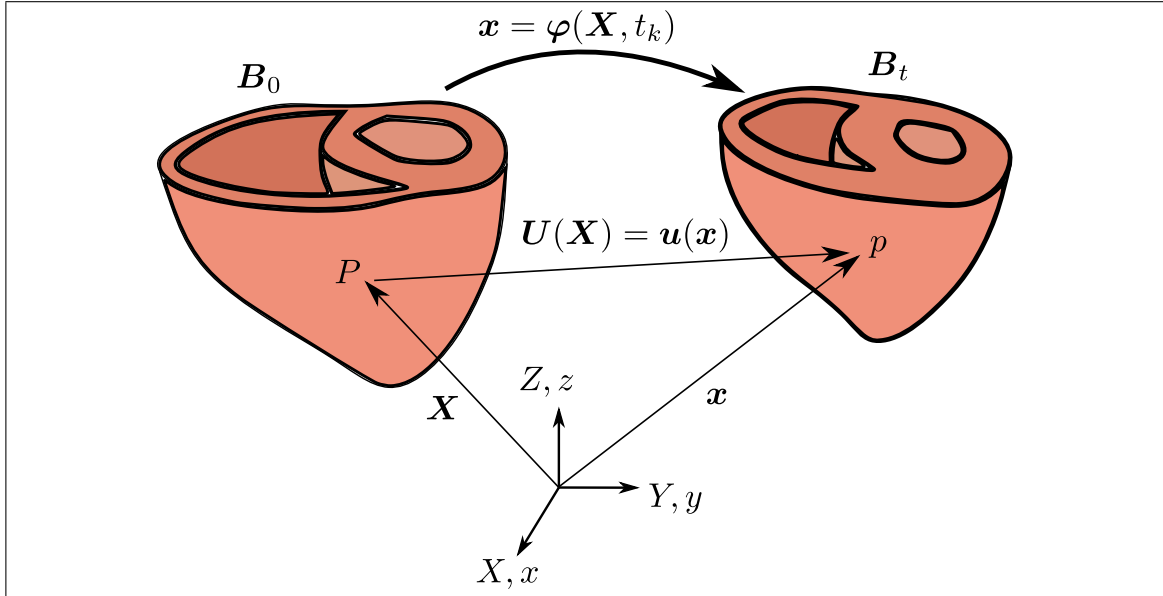


Figure 1.9. Representation of the heart as a continuum body. The motion of the heart is defined through the deformation map  $\varphi$ , which maps every material point  $P$  from an undeformed state  $B_0$  (i.e., end-diastolic position) to its position at a later state  $p \in B_t$ .

The heart can be represented as a continuum body that moves through time (see Fig. 1.9). The undeformed configuration of the heart  $B_0$  is usually chosen as its position at end-diastole, i.e., just before the contraction. At any time  $t$  after end-diastole, the domain occupied by the deformed heart is denoted by  $B_t$ .

The deformation map  $\varphi$ , that completely describes the motion of the heart, can be recovered after the processing of MR images. Thus, the deformation maps of the heart can be obtained through the Green-Lagrange strain tensor  $\mathbf{E}$ :

$$\mathbf{E} = \frac{1}{2}(\mathbf{F}^T \mathbf{F} - \mathbf{I}) \quad (1.10)$$

where  $\mathbf{I}$  denotes the identity and  $\mathbf{F}$  the deformation gradient tensor defined as:

$$F_{iJ} = \frac{\partial \varphi_i}{\partial X_J} \quad (1.11)$$

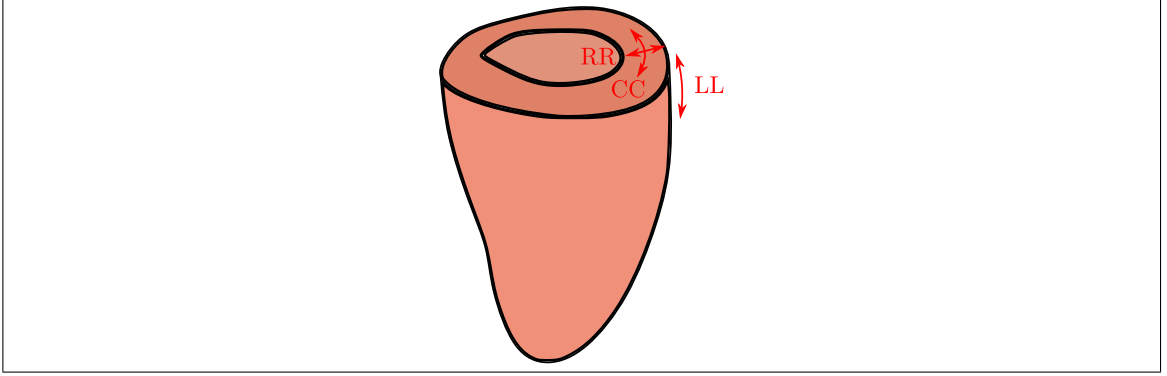


Figure 1.10. Left-ventricle of the heart with the circumferential (CC), radial (RR), and longitudinal (LL) directions represented by red arrows.

To obtain the circumferential (CC), radial (RR), and longitudinal (LL) strain components,  $\mathbf{E}$  needs to be rotated using:

$$E_{CC} = \hat{\lambda}_{CC} \cdot \mathbf{E} \hat{\lambda}_{CC}, \quad (1.12a)$$

$$E_{RR} = \hat{\lambda}_{RR} \cdot \mathbf{E} \hat{\lambda}_{RR}, \quad (1.12b)$$

$$E_{LL} = \hat{\lambda}_{LL} \cdot \mathbf{E} \hat{\lambda}_{LL}, \quad (1.12c)$$

where  $\hat{\lambda}_{CC}$ ,  $\hat{\lambda}_{RR}$ , and  $\hat{\lambda}_{LL}$  represent unit vectors pointing towards the directions CC, RR, and LL (see Fig. 1.10).

## 1.6. Objectives and hypothesis

The objective of this research is to develop strategies for the acquisition and processing of cardiac MR images, providing techniques with improved detection of motion and strain under ideal and non-ideal conditions such as noise, off-resonance artifacts, DC contamination, and large frame-to-frame motion, among others. Therefore, the specific objectives

of this investigation are: (1) to compare the state-of-the-art motion estimation techniques based on motion encoded MR images, interrogating their strengths and weaknesses. (2) To develop a new acquisition sequence that could deal with off-resonance artifacts and could be used in clinical protocols without increasing the scan time. And (3), to develop a new and more robust processing technique to estimate cardiac motion and strain from MR images that can deal with large motions, DC contamination, and signal decay.

### **1.6.1. Hypothesis**

We hypothesize that the use of more robust acquisition sequences and processing techniques on tagged MR images will lead to better estimations of motion and strain in terms of precision and accuracy than current methods based on tagging MR imaging.

## 2. FIRST ARTICLE: A COMPREHENSIVE COMPARISON OF MOTION ESTIMATION TECHNIQUES

### 2.1. Title and authors

A Comprehensive Comparison Between Shortest-Path HARP Refinement, SinMod, and DENSEanalysis Processing Tools Applied to CSPAMM and DENSE Images

*Hernán Mella<sup>1,2,6</sup>, Joaquín Mura<sup>3,6</sup>, Julio Sotelo<sup>4,6</sup>, and Sergio Uribe<sup>1,2,5,6</sup>*

<sup>1</sup> Department of Electrical Engineering, Pontificia Universidad Católica de Chile, Santiago, Chile.

<sup>2</sup> Biomedical Imaging Center, Pontificia Universidad Católica de Chile, Santiago, Chile.

<sup>3</sup> Department of Mechanical Engineering, Universidad Técnica Federico Santa María, Santiago, Chile.

<sup>4</sup> School of Biomedical Engineering, Universidad de Valparaíso, Valparaíso, Chile.

<sup>5</sup> Department of Radiology, School of Medicine, Pontificia Universidad Católica de Chile, Santiago, Chile.

<sup>6</sup> Millennium Nucleus for Cardiovascular Magnetic Resonance, ANID - Millennium Science Initiative Program - Millennium Nucleus in Cardiovascular Magnetic Resonance, Santiago, Chile.

Article published in the Magnetic Resonance Imaging journal (impact factor of 2.546).

### 2.2. Introduction

The myocardial strain is a regional biomarker of the cardiac function that has been assessed for several cardiovascular diseases (Fonseca et al., 2004; Ernande et al., 2012; Auger et al., 2017). One of the main advantages of strain measurements over global measurements, as ejection fraction or stroke volume, is its significant sensitivity to detect early changes in cardiac function (Cikes & Solomon, 2016).

Several non-invasive Magnetic Resonance (MR) imaging techniques have been used to estimate myocardial strain. Among them, Tagging MR imaging has been intensely used for the evaluation of strain (Axel, Montillo, & Kim, 2005; Petitjean, Rougon, & Cluzel, 2005), considering the conventional tag analysis (i.e., following the intersections of the tag lines) the current gold-standard MR method for the estimation of heart deformation (Auger et al., 2017). One of the most used Tagging modalities is Complementary Spatial Modulation of Magnetization (CSPAMM) (Fischer et al., 1993), which uses two complementary SPAMM acquisitions to generate a new image with better relaxation properties. Another technique for quantifying strain is Displacement Encoding with Stimulated Echoes (DENSE) (Aletras et al., 1999), which encodes the displacement of the tissue into the phase of the magnetization vector. In the last case, a phase-cycling approach (based on the same principle that CSPAMM) can be employed to isolate the stimulated echo (Gilson, Yang, French, & Epstein, 2004). DENSE imaging has recently been considered the new gold standard for estimating motion and strain from MRI (Goto et al., 2017; Wehner et al., 2018).

In CSPAMM and DENSE, the motion of the tissue cannot be directly estimated from the image, and other postprocessing methods need to be applied. Some well-known methods are Shortest-Path HARP Refinement (SP-HR) (an improved version of the Harmonic Phase analysis (HARP) (Osman et al., 1999, 2000)) and Sine-Wave Modeling (SinMod) (Arts et al., 2010), which extract harmonic peaks from the k-space using bandpass filters. In DENSE, the motion is estimated by isolating the stimulated echo from k-space (Spottiswoode et al., 2007; Kim et al., 2004), which contains information about the displacement of the tissue.

Several articles have evaluated the behavior of Tagging and DENSE imaging techniques under different acquisition parameters (NessAiver & Prince, 2003; Sigfridsson, Haraldsson, Ebbers, Knutsson, & Sakuma, 2011; Kim et al., 2004; D. Wang, Fu, & Ashraf, 2015; Epstein & Gilson, 2004), illustrating the importance of an appropriate imaging protocol. Recent works have compared different postprocessing methods for Tagging MR

images using synthetic images (E. S. Ibrahim, Swanson, Stojanovska, Duvernoy, & Pop-Busui, 2016; ElDeeb & Fahmy, 2016; E. S. H. Ibrahim et al., 2018; Cao et al., 2018), giving insights about the differences between SinMod and HARP methods. The estimation of motion and strain with both Tagging and DENSE images have also been compared against feature tracking (Li, Liu, Occleshaw, Cowan, & Young, 2010), providing a picture of the reproducibility and differences in the estimation of radial, circumferential, and longitudinal strain components from each imaging modality (Cao et al., 2018; Augustine et al., 2013; Wu et al., 2014). Furthermore, the estimation of motion and strain using conventional methods from SPAMM and DENSE images has also been studied under controlled conditions on in-silico, in-vitro, and in-vivo experiments (A. A. Young, Li, Kirton, & Cowan, 2012), showing comparable performances in all cases except for radial strain, where analysis of DENSE images showed best results. However, most of these works suffer from a lack of analytical solutions or controlled experiments and have excluded variables such as the cardiac motion, pixel sizes, noise level, and tag periods, among other relevant parameters.

Although there is a consensus about the expected performance of motion and strain metrics estimated from each imaging modality, the ultimate performance depends on the acquisition parameters and the postprocessing strategy used. This work aims to analyze the precision and accuracy in estimating both motion and strain, compared against simulated values, using SP-HR, SinMod, and DENSEanalysis; three different automated post-processing tools on CSPAMM and DENSE images when subjected to several noise and resolution levels. The study firstly uses images from 2D phantoms with only in-plane motion and under ideal acquisition conditions. Secondly, under non-ideal conditions, considering a cartesian acquisition (i.e., adding EPI-like artifacts, k space cropping, and k space filtering). Finally, the sensitivity analysis in estimating the three-dimensional cardiac motion and artifacts is performed using 3D data sets. To achieve these goals, we developed a multi-platform open-source Python (Van Rossum & Drake, 2009) library to generate numerical phantoms of CSPAMM and DENSE MR images, which can be used to simulate different physiological motion conditions.

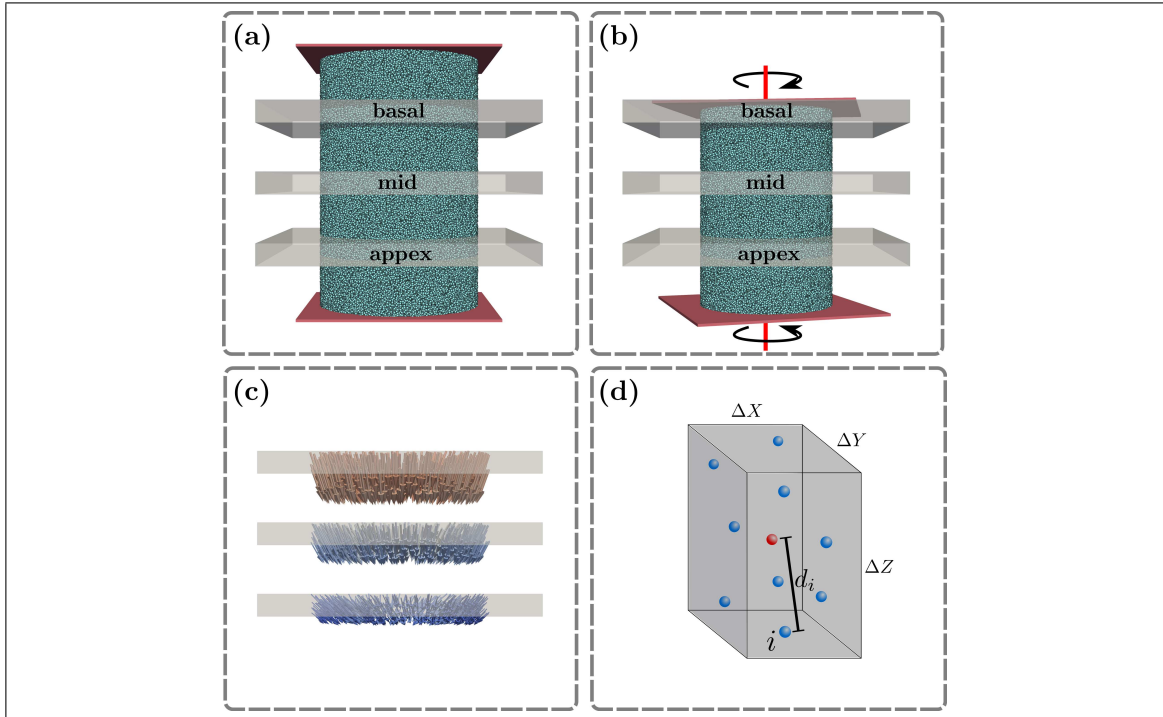


Figure 2.1. Representation of the synthetic geometry and slices used to generate the images. (a) The geometry in the undeformed state was used to place the basal, mid, and apical slices. (b) As the geometry moves with a clockwise and counterclockwise rotation at the base and apical levels, the isochromats move in and through the plane of each slice. (c) The displacement field observed in (b) of the isochromats is shown in the same slices, showing the amount of in- and through-plane motion. (d) To estimate the voxel-wise signal, all the isochromats located inside the voxel are identified and used to define weights based on their distance with respect to the voxel center (red sphere). Blue spheres denote the set of isochromats inside the voxel.

It is essential to clarify that this work compares the estimations of motion obtained with SP-HR, SinMod, and DENSEanalysis as processing tools rather than CSPAMM and DENSE as imaging sequences.

## 2.3. Material and methods

### 2.3.1. Image generation

A 3D phantom consisting of millions of isochromats randomly distributed on space is generated and limited to the cardiac geometry (see Fig. 2.1). We defined the idealized cardiac geometry as a cylinder whose in-plane motion is determined by a set of parameters and expressions given in (Gilliam & Epstein, 2012). Additionally, we added a third motion component in the through-plane ( $Z$ ) direction to achieve a displacement from base to apex up to 20 mm (Fischer et al., 1994), which is given by:

$$\Delta Z = 20 \times (\tilde{Z} - 1) \quad (2.1)$$

where  $\tilde{Z}$  is a normalized coordinate that varies from 0 to 1 from base to apex and  $\Delta Z$  the through-plane displacement. To emulate the clockwise and anticlockwise rotation of the LV at the basal and apical levels (Fischer et al., 1994), we added a scaling factor which changes the rotation of the isochromats depending on its longitudinal position, defined by:

$$\alpha_\phi = \tilde{Z} \left( \frac{\phi_{en}^{apex}}{\phi_{en}} - 1 \right) \quad (2.2)$$

where  $\alpha_\phi$  denotes the scaling,  $\phi_{en}^{apex}$  the imposed end-systolic endocardial rotation at the apex, and  $\phi_{en}$  the end-systolic endocardial rotation at the base. In all our simulations  $\phi_{en}^{apex} > 0$  and  $\phi_{en} < 0$ .

To generate the MR images, we assigned a complex magnetization to every isochromat, which was transferred to the images using a distance-weighted sum (with respect to the voxel centers). We modified the FOV and resolution of images to emulate the k space sampling of the MR scanner. Finally, the images with the user's specifications were obtained by filtering, zero-filling, and correcting the oversampling of the generated k space.

### 2.3.2. CSPAMM magnetization

CSPAMM images were built by adding two complementary SPAMM images (Fischer et al., 1993). During each SPAMM pre-pulse, a position encoding gradient  $G$  is placed between two radiofrequency (RF) pulses with tip angles  $(+\beta + \beta)$  and  $(+\beta - \beta)$ . In both combinations, the last RF pulse stores the magnetization in the longitudinal direction  $\pm Z$  (depending on its polarity) to avoid  $T_2$  relaxation. With this into consideration, both complementary SPAMM magnetizations at the time  $t_n$  are given by (Fischer et al., 1993):

$$\begin{aligned}
 M_{\text{SPAMM}}(t_n) &= M_0 \cos^2(\beta) \sin(\alpha) e^{-t_n/T_1} + M_0 \sin(\alpha) \cos^n(\alpha) (1 - e^{-t_n/T_1}) \\
 &\pm \left\{ \frac{M_0}{2} \sin(\alpha) \cos^n(\alpha) \sin^2(\beta) e^{-t_n/T_1} e^{-ik_e X} \right. \\
 &\left. + \frac{M_0}{2} \sin(\alpha) \cos^n(\alpha) \sin^2(\beta) e^{-t_n/T_1} e^{+ik_e X} \right\} \quad (2.3)
 \end{aligned}$$

where  $M_0$  represents the magnetization at the thermal equilibrium,  $i = \sqrt{-1}$  the complex unit,  $\alpha$  the imaging flip angle,  $X$  the material position of the tissue, and  $k_e$  the encoding frequency. The sign of the last term in Eq. 2.3 depends on RF pulses polarity during the preparation step. Thus, if two complementary SPAMM images  $I_{\text{SPAMM}}^A$  and  $I_{\text{SPAMM}}^B$  are acquired, their difference leads to the CSPAMM magnetization expression:

$$\begin{aligned}
 M_{\text{CSPAMM}}(t_n) &= I_{\text{SPAMM}}^A - I_{\text{SPAMM}}^B \\
 &= M_0 \sin(\alpha) \cos^n(\alpha) \sin^2(\beta) e^{-t_n/T_1} e^{-ik_e X} \\
 &\quad + M_0 \sin(\alpha) \cos^n(\alpha) \sin^2(\beta) e^{-t_n/T_1} e^{+ik_e X} \quad (2.4)
 \end{aligned}$$

### 2.3.3. DENSE magnetization

The DENSE acquisition sequence encodes the displacement of the tissue directly on the phase of the magnetization. The preparation pulse is the same as SPAMM, but the acquisition sequence differs due to an additional gradient with the same magnitude applied in the preparation step, which rephases the static spins. In this sequence, the magnetization is also stored in the longitudinal direction to avoid  $T_2$  relaxation. Thus, the magnetization

expression at the time  $t_n$  for the DENSE technique becomes (Kim et al., 2004):

$$\begin{aligned}
M_{\text{DENSE}}(t_n) &= M_0 \sin(\alpha) \cos^n(\alpha) (1 - e^{-t_n/T_1}) e^{-ik_e(X+\Delta X)} \\
&\pm \frac{M_0}{2} \sin(\alpha) \cos^n(\alpha) e^{-t_n/T_1} e^{-ik_e\Delta X} \\
&\pm \frac{M_0}{2} \sin(\alpha) \cos^n(\alpha) e^{-t_n/T_1} e^{-ik_e(2X+\Delta X)}
\end{aligned} \tag{2.5}$$

where  $\Delta X$  represents the displacement of the tissue and  $k_e$  the encoding frequency and the sign of the two first terms depend on the polarity of RF pulses during the preparation step. Thus, similarly to CSPAMM, if two complementary DENSE images  $I_{\text{DENSE}}^A$  and  $I_{\text{DENSE}}^B$  are acquired, their difference leads to:

$$\begin{aligned}
M_{\text{CDENSE}}(t_n) &= I_{\text{DENSE}}^A - I_{\text{DENSE}}^B \\
&= \frac{M_0}{2} \sin(\alpha) \cos^n(\alpha) e^{-t_n/T_1} e^{-ik_e\Delta X} \\
&+ \frac{M_0}{2} \sin(\alpha) \cos^n(\alpha) e^{-t_n/T_1} e^{-ik_e(2X+\Delta X)}
\end{aligned} \tag{2.6}$$

The last step is also called phase-cycling (Gilson et al., 2004).

### 2.3.4. Numerical experiments

#### 2D analysis

We generated a synthetic dataset using SPAMM and DENSE magnetization expressions given in Equations 2.3 and 2.5, where a different image was generated for each RF pulse polarity to obtain, after subtraction, the CSPAMM and phase-cycled DENSE images. The dataset consisted of 100-2D slices of a short-axis view of an idealized left-ventricle with only in-plane motions with a FOV of  $100 \times 100 \times 8\text{mm}^3$  and isotropic (in-plane) pixel sizes of 1.0, 1.5, 2.0, 2.5, and 3.0 mm. For this experiment only mid-level slices were considered. The number of isochromats used in each data was around  $22/\text{mm}^3$  (this density depends on the LV volume rather than the slice volume) which means that smaller voxels contained a smaller number of isochromats (a voxel of  $1 \times 1 \times 8\text{mm}^3$  that belongs

completely to the LV contained 176 isochromats, while a voxel of  $3 \times 3 \times 8\text{mm}^3$  contained 1584). This number was arbitrarily defined and only depends on the computational capacity, the signal requirements, and the time available for the generation.

For the SPAMM images, we used encoding frequencies of 0.79, 0.63, 0.52, 0.45, and 0.39  $\text{rad mm}^{-1}$  to achieve tag periods of 8, 10, 12, 14, and 16 mm respectively. Here, it must be noticed that the tag period is effectively one period of the sinusoid given in Equations 2.3 and 2.4 and not half of the period as usually reported as tag spacing in magnitude images. Additionally, to make a fair comparison with DENSE and avoid adding an unwanted DC component, we decided to work with complex CSPAMM data. A fixed encoding frequency of 0.75  $\text{rad mm}^{-1}$  was chosen for DENSE images to achieve suitable echoes for phase-cycling correction and avoid large phase wrapping artifacts. The imaging flip angle for both images was chosen as  $15^\circ$  (constant through the cardiac phases), and a tissue  $T_1$  relaxation of 0.85 seconds was used to emulate the relaxation properties of the myocardium at 1.5T (Fischer et al., 1993).

We randomly choose the physiological parameters, which controls the geometry and motion, according to Gilliam et al. (Gilliam & Epstein, 2012), i.e., we choose different physiology for each synthetic data. In our case, we used a set of parameters defining 50 cases with normal deformation patterns (normal cardiac function) and 50 with abnormal patterns (regionally reduced function) (Gilliam & Epstein, 2012) to interrogate the three methods under different levels of motion at end-systole. For the analysis of the results, both types of deformation patterns were equally considered for the estimation of the error metrics and no differences were made between them. The displacement field of the defined motion is defined by

$$\Delta \mathbf{r}_n(t) = \Gamma(t)(\Delta \mathbf{r}_n^{ES} - \Delta \mathbf{r}_n^{ED}) \quad (2.7)$$

Where  $\Gamma(t) \in [0, 1]$  is a piece-wise continuous function, which mimics the standard left-ventricular volume diagram (McCulloch, 2000) and modulates the maximum end-systolic displacement, and  $\mathbf{r}_n^{ES}$  and  $\mathbf{r}_n^{ED}$  the end-systolic and end-diastolic position of the LV, respectively (the expression defining  $\Gamma(t)$  is given in the Appendix A.1).  $\mathbf{r}_n^{ED}$  is defined

Table 2.1. Noise levels and corresponding Signal to Noise Ratios in the noise sensitivity analysis images. The noise level has the same standard deviation throughout the cardiac cycle. However, from early-systole to late-diastole, the SNR decreases due to the signal model given in Equations 2.4 and 2.6. The reported SNR has adimensional units.

Name	Noise level	Early-systolic SNR ( $\times\alpha$ )	Late-diastolic SNR ( $\times\alpha$ )
NL <sub>0</sub>	0	noise-free	noise-free
NL <sub>1</sub>	1	33.6	8.4
NL <sub>2</sub>	2	27.6	7.0
NL <sub>3</sub>	3	21.4	5.5

$\alpha$ : scaling factor to consider the signal decay due to the reduction of the voxel size. For an in-plane isotropic pixel size (and constant slice thickness) of 3, 2.5, 2, 1.5, and 1 mm the associated factors are 1, 0.69, 0.44, 0.25, 0.11, respectively.

by the initial geometry of the phantom (for all the 2D data, we used a cylinder height of 8 mm as only in-plane motions were considered), whereas  $r_n^{ES}$  depends on several parameters uniformly distributed, such as the end-diastolic endocardial radius, end-diastolic wall thickness, end-systolic endocardial and epicardial twist, and end-systolic endocardial and area scaling, among others (Gilliam & Epstein, 2012). The expressions and parameters defining the motion patterns and the geometry of the synthetic LV are given in the Appendix A.1.

We performed a resolution and noise sensitivity analysis to the estimation of displacements and strain obtained from CSPAMM and DENSE MR images using SP-HR, SinMod, DENSEanalysis.

The resolution sensitivity analysis considered several pixel sizes and tag periods for both imaging modalities, whereas, for the noise experiment, we used the tag periods that performed better in the first experiment using the following rule: given fixed pixel size and for all the tag periods, the tag period used for the noise analysis was that one that minimizes the error on the circumferential strain component. The idea behind this selection is to test just those cases which performed better in the estimation of circumferential strain due to the clinical relevance of this biomarker.

Real and imaginary Gaussian noise with zero mean was added to the image k-spaces. The standard deviation (SD) of the noise was estimated to achieve certain SNRs at early systole and late diastole only on  $3 \times 3 \text{ mm}^2$  phase-cycled DENSE images, as described in Table 2.1. However, the noise was added separately before phase-cycling. The same SD was used for images with smaller pixel sizes as the signal is reduced during the generation process (fewer isochromats are inside the voxels). The best and the worst noise scenario can be commonly found on standard cartesian cine (Kim et al., 2004) and undersampled (Sigfridsson et al., 2011) cine DENSE acquisitions with a constant flip angle. The noise SD was estimated as a fraction of the maximum magnitude of the stimulated echo in the k space, which at  $t = 0$  shares the same magnitude as the spectral peaks of the cosine modulation (see Equations 2.3 and 2.5), and therefore can also be used in SPAMM images.

### 3D analysis

In this case, just one set of physiological parameters was chosen (see Table 2.1) to generate slice-following versions of the CSPAMM and DENSE images (Fischer et al., 1994; Spottiswoode et al., 2008). For both imaging techniques, the slice thickness of the selective excitation was 8 mm with offsets of 12 and 6 mm for slices at basal and mid cardiac levels, whereas the imaged thickness was 30, 25, and 20 mm for slices at basal, mid, and apical cardiac levels respectively (Stuber et al., 1999). The encoding frequency used for SPAMM was  $0.39 \text{ rad mm}^{-1}$  (tag period of 16 mm) and for DENSE  $0.75 \text{ rad mm}^{-1}$ . Both images also shared the same FOV of  $350 \times 350 \text{ mm}^2$ , and were generated using imaging matrices of  $256 \times 128$  for SPAMM and  $128 \times 64$  for DENSE with an oversampling factor of 2 in the measurement direction. A constant flip angle of  $15^\circ$  was used to simulate the acquisition of 20 cardiac phases. The dimensions of the cylinder emulating the LV geometry are given in Table 2.2. The same density of isochromats used for the 2D generation was used in this experiment, i.e., the number of isochromats contained in the cylinder was 4 millions.

Table 2.2. Physiological parameters used for the generation of images with 3D motion patterns

$R_{en}$	$\tau$	$H$	$\sigma$	$S_{ar}$	$S_{en}$	$\phi_{en}$	$\phi_{en}^{apex}$	$\phi_{ep}$	$\Psi$	$\chi$	$t_A$	$t_B$	$t_C$
25	10	100	4.0	0.7	1.1	-8.0	20	-4.0	0.0	0.5	0.15	0.35	0.5

$R_{en}$ : endocardial radius (mm),  $\tau$ : LV thickness (mm),  $H$ : long axis height (mm),  $\sigma$ : the skew factor which moves motion towards epicardial ( $\sigma > 1$ ) or endocardial motion ( $\sigma < 1$ ),  $S_{ar}$ : end-systolic area scaling,  $S_{en}$ : end-systolic endocardial scaling,  $\phi_{en}$ : end-systolic endocardial twist ( $^\circ$ ),  $\phi_{ep}$ : end-systolic epicardial twist ( $^\circ$ ),  $\Psi$ : the direction in which the motion is reduced ( $^\circ$ ),  $\xi$ : motion reduction factor,  $t_A$ ,  $t_B$ ,  $t_C$ : time modulation times (s)

Additionally, we simulated a cartesian acquisition and added multi-shot EPI-like artifacts considering a “top-down” acquisition with a receiver bandwidth of 64 KHz, echo-train length of 9, and off-resonance frequency of 115 Hz, as described in (Bender, Ahmad, & Simonetti, 2013). This setup generates a shifting artifact in the reconstructed image due to the linear accumulation of phase across the k space. Also, complex Gaussian noise was added to achieve the SNRs given by the  $NL_1$  in Table 2.1. The previously described EPI artifact and noise were added to each SPAMM and DENSE acquisitions used to generate CSPAMM and complementary DENSE images.

The imaging parameters were chosen according to standard values given in the literature. Pixel sizes, slice-thicknesses, tag periods, acquisition matrices, number of cardiac phases, and flip angles were similar to that described in (Stuber et al., 1999; Tecelão et al., 2006; X. Liu & Prince, 2010) for the acquisition of CSPAMM and slice-following CSPAMM images in volunteers, while similar DENSE imaging parameters, including the given encoding frequency, have been used in (Kim et al., 2004; Spottiswoode et al., 2007; Sigfridsson et al., 2011) for in-vivo studies.

The set of physiological parameters used in this study (following the notation of Gilliam et al. (Gilliam & Epstein, 2012)), which defines the motion at the basal level, are presented in Table 2.2.

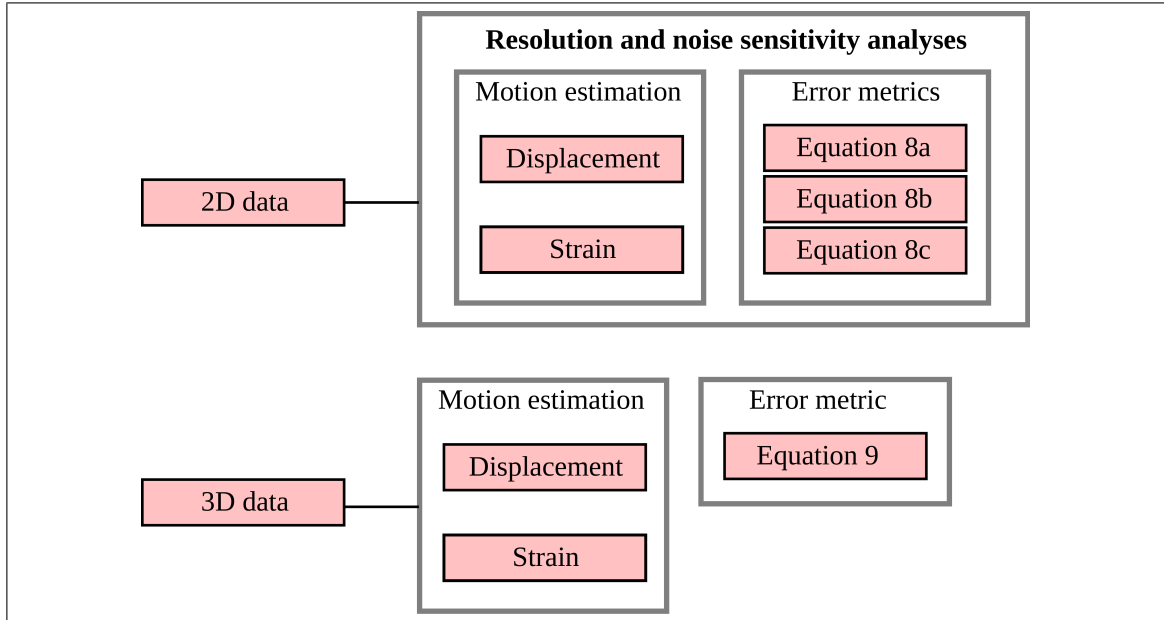


Figure 2.2. Using the 2D data, displacement and strain fields are estimated for every resolution and noise level described in the Experiments section. Then, the error metrics given in Equations 8a, 8b, and 8c are evaluated. For the 3D data, displacement and strain fields are estimated and the error metric given in Equation 9 is evaluated.

A summarized description of the 2D and 3D experiments is shown in Fig. 2.2.

### 2.3.5. Image processing

In Eq. 2.5, the three terms (in order of appearance) are often called Stimulated, Complex Conjugate, and Relaxation echoes (see Figure 3b), centered at  $(0, 0)$ ,  $(2k_e, 0)$  and  $(k_e, 0)$  respectively. By using the phase-cycling approach, the relaxation echo is canceled (see Eq. 2.6). However, depending on the pixel size (i.e., k space bandwidth), energy from the complex-conjugate echo could be partially or entirely sampled, leading to severe artifacts (Kim et al., 2004). To correct these artifacts, we applied a Butterworth filter (H. Wang & Amini, 2013) of 10-th order and fixed cutoff frequency was applied to every DENSE image.

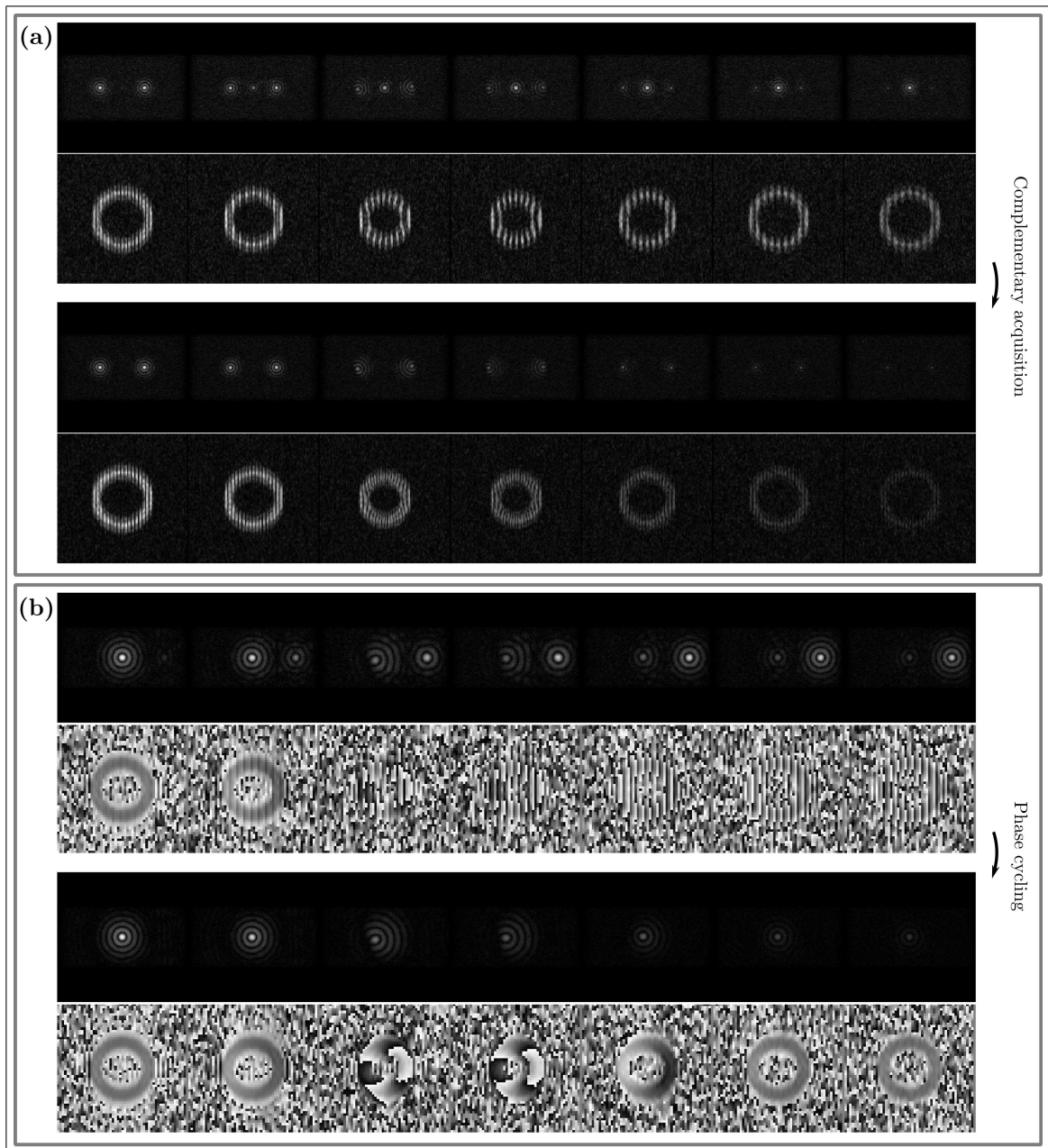


Figure 2.3. k-space and reconstructed images for (a) SPAMM and CSPAMM, and (b) DENSE and phase-cycled DENSE of an mid-level short-axis slice. The frames 1, 4, 7, 10, 13, and 19 of an acquisition of 20 frames equally distributed in a cardiac cycle of 1 second are shown. In the case of SPAMM and CSPAMM, the image shows the reconstructed magnitude, whereas for DENSE and phase-cycled DENSE, the reconstructed phase. For the image simulation, a multi-shot EPI acquisition was used in all cases, with half of the lines sampled in the phase direction.

### 2.3.6. Motion estimation

Using motion estimation techniques, we tracked the CSPAMM and DENSE images to a reference domain at end-diastole. Once the displacement field  $U(\mathbf{X})$  was estimated, we calculated the Lagrangian strain tensor  $\mathbf{E}$  (Fonseca et al., 2004; Auger et al., 2017). In this study, we evaluated the circumferential ( $E_{CC}$ ) and radial ( $E_{RR}$ ) components of the tensor, which are usually used to evaluate strain in short-axis views. As our implementations of SP-HR, SinMod, and DENSE analysis only allowed 2D motion estimation, the longitudinal strain component of the tensor  $\mathbf{E}$  was not evaluated.

Motion from CSPAMM images was obtained using a free version of the SP-HR algorithm provided by the Image Analysis and Communication Lab at Johns Hopkins University (X. Liu & Prince, 2010), and a self-made implementation of SinMod as described by the developers (Arts et al., 2010). In contrast, for DENSE images, the MATLAB toolbox DENSEanalysis (Spottiswoode et al., 2007; Gilliam & Suever, 2016) was used.

In the case of SinMod analysis, no frequency windowing was applied, and resulting displacements were corrected using the quality model proposed by the authors (Arts et al., 2010) with a weighting matrix with 8 in the exponent. In both cases, SP-HR and SinMod, the same bandpass filter was used, as described by Arts et al. (Arts et al., 2010).

When using DENSEanalysis, a temporal fitting of a 10th-degree polynomial was applied (H. Wang & Amini, 2010), and displacement resampling was done using the implementation of the gridfit function given in DENSEanalysis (Gilliam & Epstein, 2012; Gilliam & Suever, 2016), with a triangular interpolation scheme with a smoothing factor of 0.8 for noisy data. The same temporal fitting procedure was used for SP-HR and SinMod displacements.

From the 3D results, mean strains were estimated from the base, mid, and apical cardiac levels using the segmentation defined by the American Heart Association (AHA) (Cerqueira et al., 2002; Selvadurai et al., 2018). As the motion used in this experiment did not contain regional differences, the right-ventricular insertion point was arbitrarily

chosen and used as the reference to evaluate each segment. The segmentation used for the regional strain estimation is shown in Figure S1.

### 2.3.7. Statistical analysis

The error was measured using the Normalized Root Mean Square Error (nRMSE) and Directional Error (DE), defined as (Mura et al., 2016):

$$\text{nRMSE}_a(\%) = 100 \times \frac{1}{\max_i |a_i^e|} \sqrt{\frac{1}{N} \sum_{i=1}^N |a_i - a_i^e|^2} \quad (2.8a)$$

$$\text{nRMSE}_u(\%) = 100 \times \frac{1}{\max_i \|\mathbf{u}_i^e\|_2} \sqrt{\frac{1}{N} \sum_{i=1}^N \|\mathbf{u}_i - \mathbf{u}_i^e\|_2^2} \quad (2.8b)$$

$$\text{DE} = \frac{180}{\pi N} \sum_{i=1}^N \arccos \left( \frac{|\mathbf{u}_i \cdot \mathbf{u}_i^e|}{\|\mathbf{u}_i\| \|\mathbf{u}_i^e\|} \right) \quad (2.8c)$$

where  $N$  represents the number of masked pixels in the image,  $\text{nRMSE}_a(\%)$  and  $\text{nRMSE}_u(\%)$  are the nRMSE for scalar and vectorial quantities respectively,  $a_i$  is any pixelwise scalar quantity at the pixel  $i$  (e.g., circumferential and radial strains), and  $\mathbf{u}_i$  is the displacement field at the pixel  $i$ . The superscript  $()^e$  denotes the exact value. The three previous error metrics were evaluated for SP-HR, SinMod, and DENSEanalysis results at end-systole, where displacements have maximum amplitude.

The error metrics defined in Eq. 2.8 characterized the mean value of the pixelwise error for just one data. However, the error metrics presented in the next section are the mean value across the whole dataset ( $N=100$ ) of the metrics estimated using 2.8.

Finally, to quantify the error in the estimation of regional strain throughout the entire cardiac cycle, we introduce another metric given by:

$$\text{Err}_{\text{seg}} = 100 \times \frac{1}{N_{\text{fr}}} \sum_{n=1}^{N_{\text{fr}}} \frac{|\overline{E}(t_n) \overline{E}^e(t_n)|}{\max_n |\overline{E}^e(t_n)|} \quad (2.9)$$

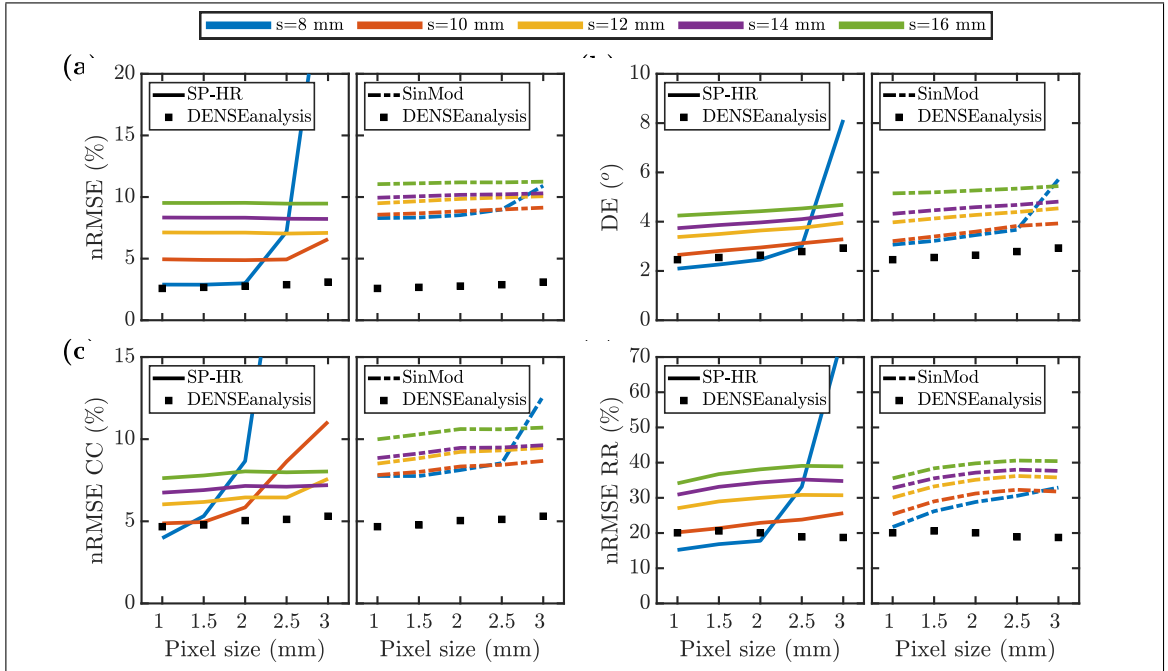


Figure 2.4. Results for the resolution sensitivity analysis. Mean errors in (a) magnitude, (b) direction of the displacement field, (c)  $E_{CC}$ , and (d)  $E_{RR}$  strain components. The left plot of each case shows the results obtained using SP-HR and to the right using SinMod. The results from DENSEanalysis are shown on all the plots. Each color denotes a different tag period ( $s$ ). Overall, the estimation obtained from DENSE images performed better than the other techniques, whereas using CSPAMM images, better results were obtained for smaller pixel sizes and wavelengths.

where the overline denotes the mean value across all the segments,  $\overline{E}(t_n)$  and  $\overline{E}^e(t_n)$  the estimated and exact mean strains at the time  $t_n$ , and  $N_{fr}$  the number of frames (cardiac phases).

## 2.4. Results

### 2.4.1. Sensitivity analysis: resolution

Fig. 2.4 shows the mean nRMSE and DE values across all the analyzed data without noise. In the absence of noise, smaller pixel sizes improve the estimation of displacements and strain using the three techniques. Regarding the displacement field evaluation, the best

performance was achieved by DENSEanalysis, and almost always SP-HR performed better than SinMod (see 2.4a and 2.4b). For standard resolutions of DENSE and CSPAMM images (in-plane isotropic voxel sizes around 3.0 and 1.5 mm respectively (8, 16)), the differences in the performance of DENSEanalysis and SP-HR become a bit smaller, whereas with SinMod results always showed larger errors.

A similar tendency occurs for the estimation of strain. For almost every pixel size, results obtained with DENSEanalysis postprocessing were better than SP-HR and SinMod (see 2.4c and 2.4d). Although the nRMSE of the  $E_{CC}$  obtained with SP-HR grows for tagging periods of 8, 10, and 12 mm, in general terms, SP-HR performed better than SinMod in most of the cases. Additionally, the error  $E_{CC}$  did not follow a clear trend for the spacing of 8 mm. A similar behavior was observed for the  $E_{RR}$  component, although the nRMSE increased with the three postprocessing techniques, with errors rising to around 31% with SP-HR, 33% with SinMod, and 20% with DENSEanalysis (see Figure 2.4d).

Fig. 2.5 shows the mean values and standard deviations (between data) of the most favorable cases of the analysis presented in Fig. 2.4, i.e., combinations of tag periods and pixel sizes where the nRMSE of the  $E_{CC}$  component reached the minimum value of all the curves (see Fig. 2.4c). With SinMod, the best results were obtained using a fixed tagging period of 10 mm for every pixel size, while with SP-HR, the best performance was achieved using a tag period of 10 mm for pixel sizes of 1, 1.5, and 2 mm, and 14 mm for pixels of 2.5 and 3 mm. Despite the difference in the errors between the three methods, all of them shared similar deviations.

#### 2.4.2. Sensitivity analysis: noise

Fig. 2.6 shows the error metrics calculated from the noisy data using the tagging spacings given in Fig. 2.5. As the noise level increases, the overall performance of three motion estimation techniques become worse (as expected). Moreover, the gap between noise levels becomes higher for smaller pixel sizes as the images with larger k space bandwidth are noisier (see the SNR scaling in Table 2.1). At any noise level and resolution,

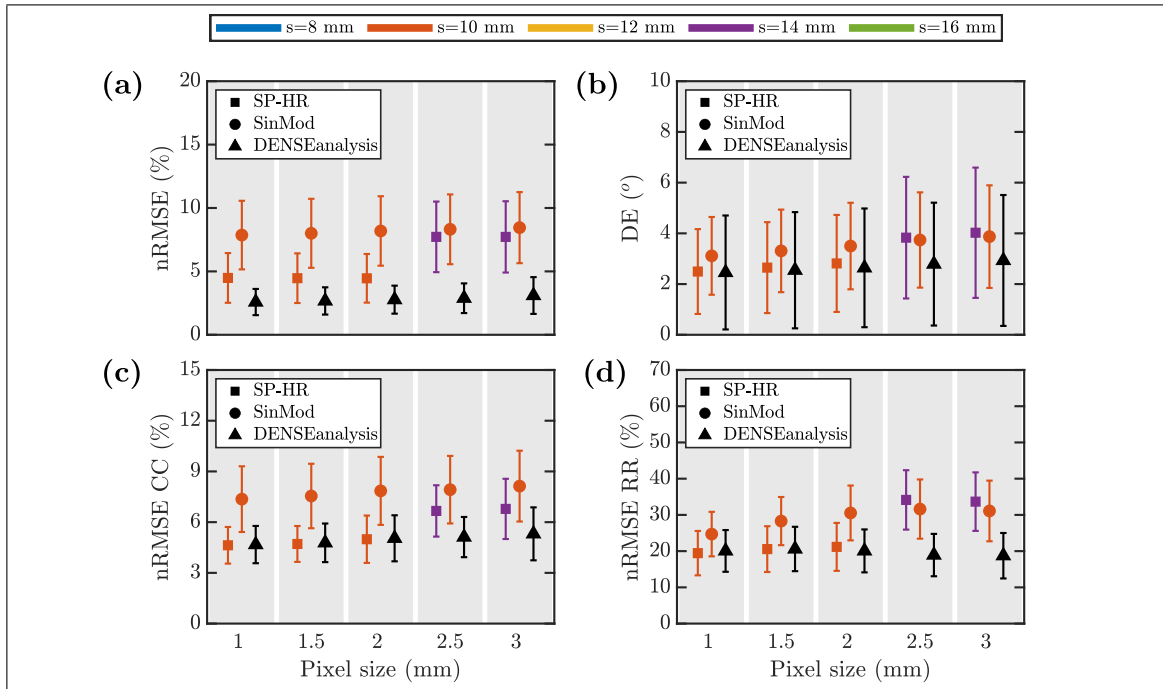


Figure 2.5. Mean errors and standard deviations for the best performing combination of tag periods and pixel sizes of the results given in Figure 4, for (a) magnitude, (b) direction of the displacement field, (c)  $E_{CC}$  and (d)  $E_{RR}$  strain components. Each color represents a different tag period (s). The three methods showed similar results in terms of mean errors and deviations (except in the displacement field magnitude, where deviations obtained with DENSEanalysis remain low).

the displacement fields were better estimated using DENSEanalysis (see 2.5a and 2.5b). However, the difference was more evident for the magnitude rather than the direction. For NL3 case and standard isotropic in-plane pixel sizes of 1.5 and 3 mm for CSPAMM and DENSE images, the nRMSE in magnitude and DE were approximately  $6.2 \pm 2.4\%$  and  $6.7 \pm 5.3^\circ$  for SP-HR,  $9.2 \pm 2.6\%$  and  $7.0 \pm 4.8^\circ$  for SinMod, and  $3.4 \pm 1.4\%$  and  $4.4 \pm 3.9^\circ$  for DENSEanalysis. Although the estimations made with DENSEanalysis showed the best performance, the results obtained with SP-HR and SinMod were comparable with DENSEanalysis.

In terms of strains, the behavior of the three methods was similar between the  $E_{CC}$  and the  $E_{RR}$  components. The errors showed less sensitivity to noise at bigger pixel sizes

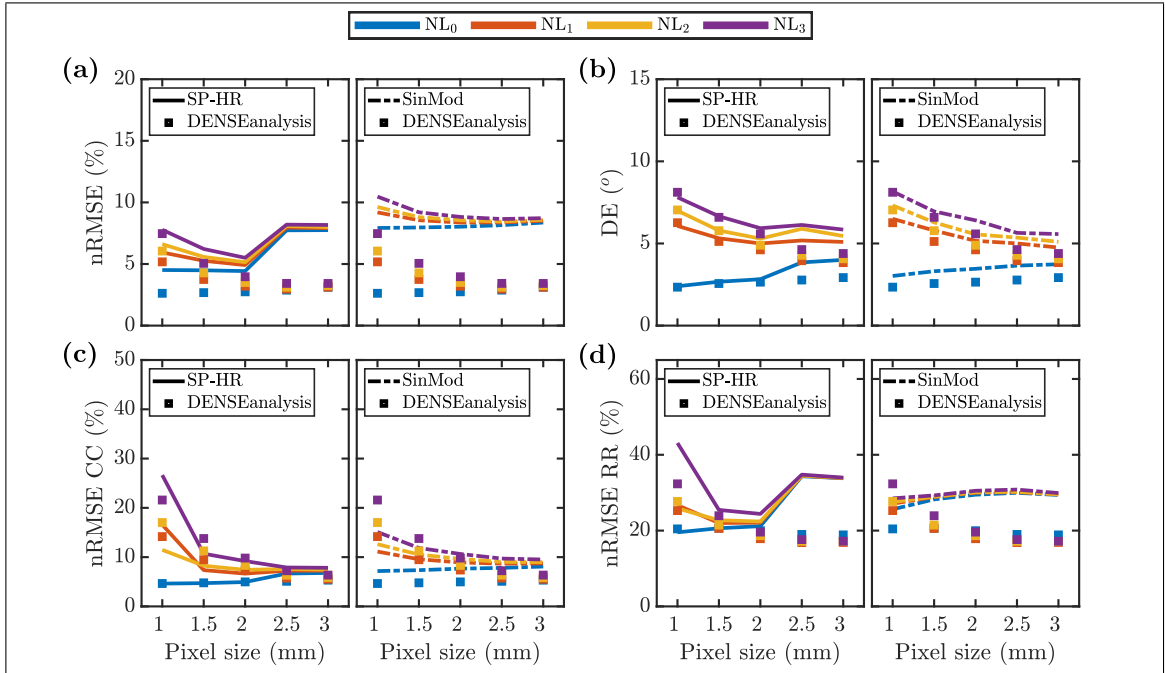


Figure 2.6. Results for the noise sensitivity analysis for an end-systolic cardiac phase. Mean errors in (a) magnitude, (b) direction of the displacement field, (c)  $E_{CC}$ , and (d)  $E_{RR}$  strain components. The left plot of each metric shows the results obtained using SP-HR and to the right using SinMod. The results from DENSEanalysis are shown in all the figures. Each color denotes a different SNR (see Table 2.1). SP-HR gave the most significant sensitivity to noise in every case, whereas DENSEanalysis showed the smallest.

in both cases, with an increasing trend as the pixel size decreases. However, the error obtained using SinMod showed less sensitivity to noise than SP-HR and DENSEanalysis at any pixel size for both strain components.

For the same pixel sizes and noise level previously mentioned, the nRMSE obtained for the  $E_{CC}$  and  $E_{RR}$  components were  $10.7 \pm 10.8\%$  and  $25.5 \pm 14.8\%$  using SP-HR,  $11.9 \pm 2.5\%$  and  $29.3 \pm 6.5\%$  using SinMod, and  $6.4 \pm 2.0\%$  and  $18.2 \pm 4.6\%$  using DENSEanalysis. These results showed a substantial increase in the error variability with SP-HR, which means that the noise highly impacted the motion estimation under different contraction conditions. As in the previous section, the estimation of the  $E_{RR}$  component

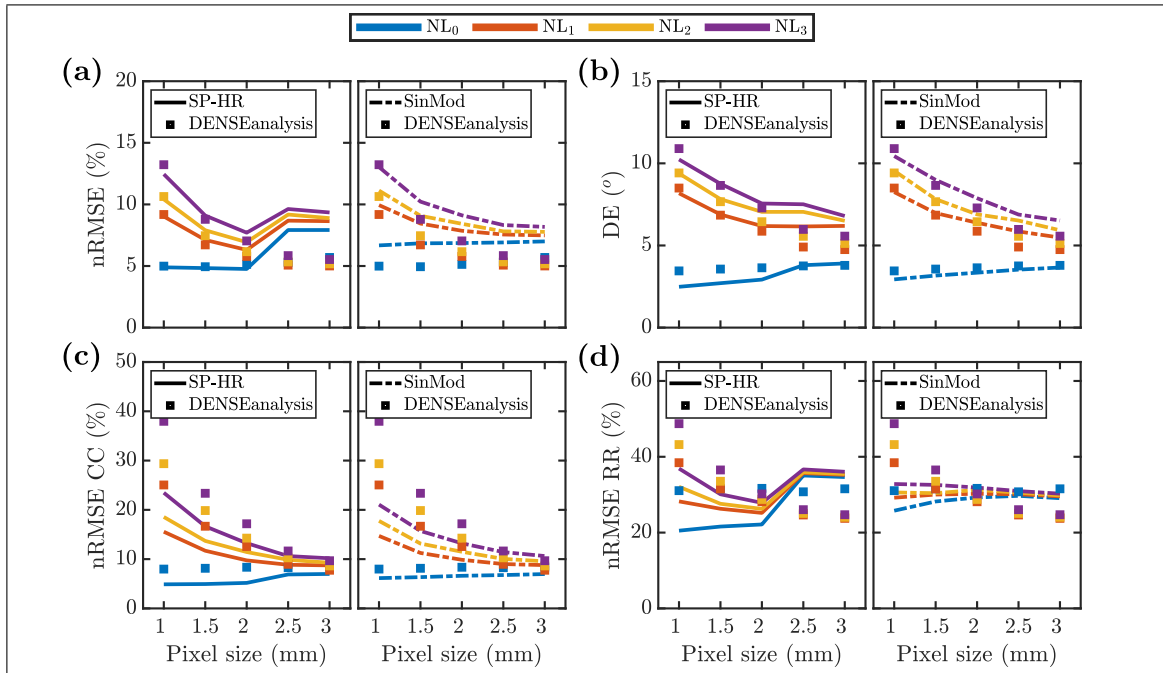


Figure 2.7. Results for the noise sensitivity analysis for an early-systolic cardiac phase. Mean errors in (a) magnitude, (b) direction of the displacement field, (c)  $E_{CC}$ , and (d)  $E_{RR}$  strain components. The left plot of each metric shows the results obtained using SP-HR and to the right using SinMod. Each color denotes a different noise level. As the displacement is small at the beginning of the cardiac cycle, the impact of noise on the phase of harmonic and stimulated echo images becomes more prominent. As a consequence, worse results were achieved for all the error metrics.

was worse than the  $E_{CC}$  component for all the tested postprocessing methods but was better captured using DENSEanalysis for all noise levels.

For small motions, i.e., early systolic cardiac phases, the error metrics for estimating displacement and strain are presented in Fig. 2.7. At lower motion levels, both motion and strain calculation were worse than at end-systolic cardiac phases. The gap in the error of displacement estimation decreased, and in the case of strain, SP-HR and SinMod performed better than DENSEanalysis for the  $E_{CC}$  and partially better for the  $E_{RR}$ . That suggests that DENSEanalysis is more sensitive to noise for lower motion levels.

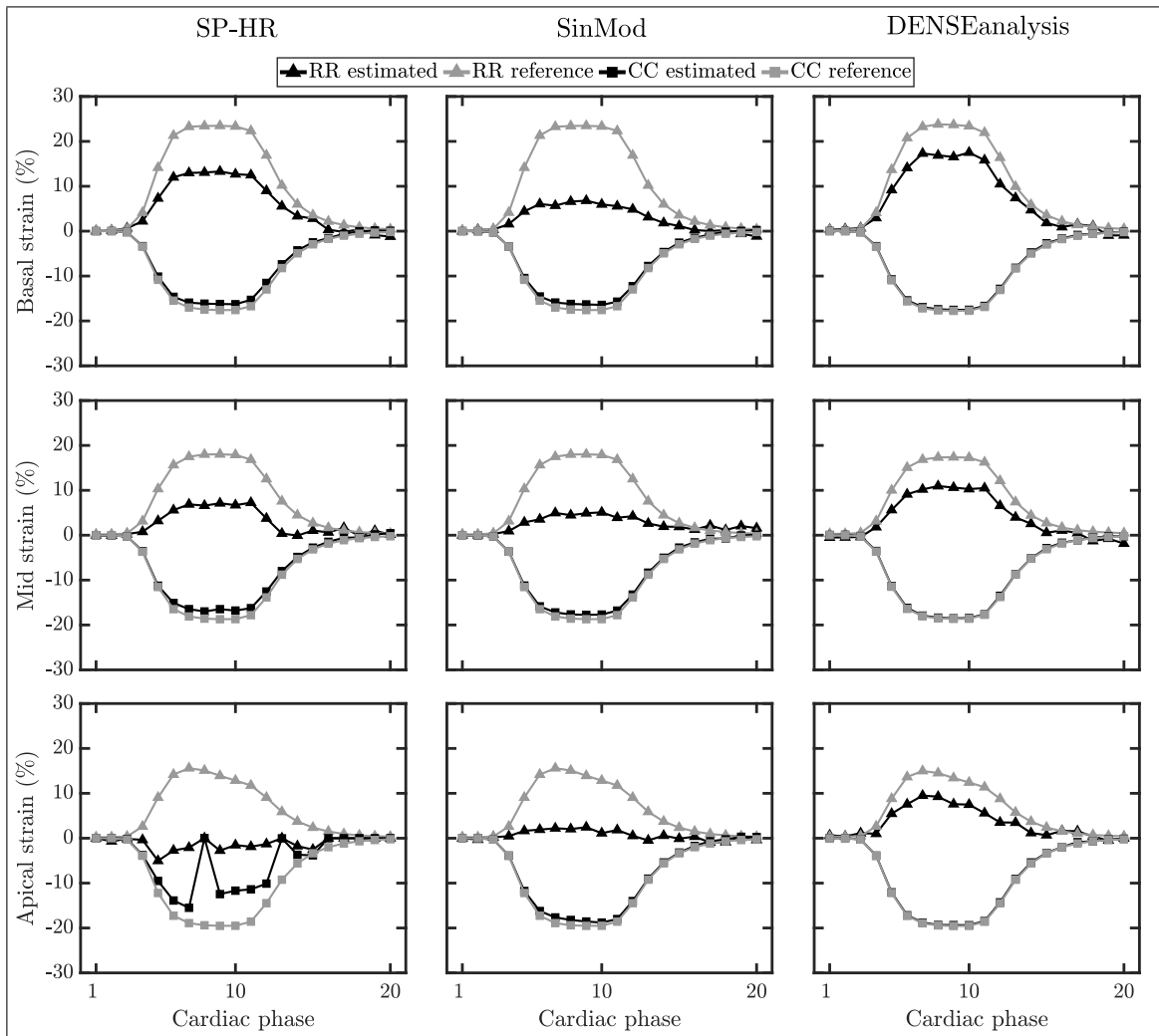


Figure 2.8. Regional strains at basal, mid, and apical levels. Each column shows the strain estimated using SP-HR, SinMod, and DENSEanalysis. Gray lines with triangle markers denote the reference curves, while black lines with square markers denote the estimations made with the three processing techniques. Every point in the curves represents the mean regional strain across the segments defined by the AHA (Cerqueira et al., 2002; Selvadurai et al., 2018). Analysis of CSPAMM images using SP-HR tends to fail for cardiac phases in the diastolic part of the cardiac cycle, resulting from the signal decay.

### 2.4.3. 3D experiment

Figure 8 shows the  $E_{CC}$  and  $E_{RR}$  strain curves obtained from basal, mid, and apical short-axis slices of the phantom shown in Fig. 2.1. In this experiment, the performance

Table 2.3.  $Err_{seg}(\%)$  for the results of the 3D experiment. Results show how far the regional strains estimated with the three methods are from the reference values. From base to apex, the synthetic phantom rotation increases, and higher errors were found using SP-HR and SinMod.

	Cardiac level	SP-HR	SinMod	DENSEanalysis
$E_{CC}$	Base	3.8	3.1	0.9
	Mid	4.3	2.4	0.7
	Apex	19.4	2.5	0.6
$E_{RR}$	Base	19.7	31.0	12.8
	Mid	27.5	30.1	19.2
	Apex	46.0	34.8	17.9

of the three methods was interrogated through the whole cardiac cycle. SP-HR showed the most unfavorable performance, especially in the apical region, where the torsion was augmented. The three methods were imprecise in estimating the  $E_{RR}$  component, but DENSEanalysis was closer to the reference values. In contrast, SinMod and DENSEanalysis gave very accurate estimations of the regional  $E_{CC}$  through the whole cardiac cycle and at any cardiac level, while SP-HR correctly behaved at basal and mid-levels.

In Table 2.3, the errors estimated using the metric proposed in Eq. 2.9 are presented, which measures the difference between strain curves. Differences calculated from the strain curve estimated with SP-HR increased as the slice moved from base to apex. However, the previous statement is no longer valid for SinMod and DENSEanalysis. SinMod did not exhibit any pattern, whereas DENSEanalysis showed decreasing and increasing trends from base to apex. The similarity between the reference and the estimated curves was minimal, and no significant differences were observed between SinMod and DENSEanalysis. However, we noted more significant discrepancies in terms of error for the  $E_{RR}$  component, where DENSEanalysis accomplished the best execution (see Table 2.3).

## 2.5. Discussion

The tag analysis from Tagging MR images has been considered the gold standard for the estimation of myocardial strain. Several approaches have been developed to estimate motion from these images, being SinMod and SP-HR two of the most used methods (Cao et al., 2018). On the other hand, the analysis of DENSE images using processing tools as DENSEanalysis has become a powerful tool for estimating displacements and strain. Nevertheless, tagging and DENSE techniques remain a research (Cao et al., 2018), and discussion about their accuracy and precision continues.

The three methods gave accurate estimations of displacements and strains (see Fig. 2.4) in the absence of noise. As the pixel size decreases, DENSEanalysis showed a slight decay in the error metrics of magnitude, direction, and  $E_{CC}$ , whereas for the  $E_{RR}$  component, the nRMSE increases with smaller pixel sizes. A similar behavior was observed with SP-HR and SinMod for almost any tag period and also for the  $E_{RR}$  component. Concerning the tag periods, there was a clear tendency for both SP-HR and SinMod. As the tag period increases, the estimation of displacement and strain deteriorates, obtaining the most significant errors with a tag period of 14 mm. However, for SP-HR, the smallest tag period did not work adequately for any pixel sizes. We can explain this behavior by comparing the pixel size, tag period, and amount of motion (Osman et al., 1999, 2000), which says that HARP-based techniques tend to fail for motions larger than the tag period. Additionally, for this tag period and the imaging parameters used, the spectral peak containing motion information was too close to the k space bandwidth, leading to information loss.

We decided not to include field inhomogeneities in the generation of the images because we did not observe considerable differences in the error metrics and their behavior. This was tested in the same experiment used to evaluate the behavior of the three techniques under noise-free conditions, but adding a smooth and spatially-varying phase to

each acquisition given in Equations 2.3 and 2.5. Moreover, the average increase in the error metrics for both displacement and strain was around 2%, while keeping their behavior observed in Fig. 2.4. The results obtained from noise-free data with field inhomogeneities are presented in Figure S2 (see supplementary material).

Although several pixel sizes were considered for the analyses, the impact of this parameter on the estimations was small in terms of displacements (see Figures 2.4a and 2.4b). This could be explained by the bandwidth of the bandpass filters used in both CSPAMM and DENSE images. For a fixed encoding frequency, the pixel size only changes the bandwidth of the k-space while the filtered spectral peaks keeps its position and distance with respect to the k-space center. Therefore, the true resolution of the filtered harmonic images and displacement maps obtained from CSPAMM and DENSE is given by the bandwidth of the filter rather than the resolution of the image.

In our experiments, estimations made from DENSE images showed a better behavior than SP-HR and SinMod for the quantification of displacements and strain from noisy data. For the range of pixel sizes usually acquired in DENSE images (2.5 to 3 mm), DENSEanalysis was less sensitive to noise than SP-HR and SinMod, for the range of resolutions usually acquired in CSPAMM images (1.5 mm) (see Fig. 2.6). This behavioral dependency on the voxel size is explained with the SNR reduction as the voxels become small, i.e., the kspace bandwidth becomes bigger. Additionally, the bandpass filters used in SP-HR and SinMod did not remove completely the high-frequency noise as they are centered at a higher frequency than the filter used to remove the remaining energy of the complex-conjugate echo in DENSE images.

In this study, the resolution and noise sensitivity analysis were performed mainly at the end of systole, where the displacement and strain have maximum amplitude. However, due to the signal decay and the low phase SNR in both CSPAMM and DENSE images, the estimation can be biased during early systolic and late diastolic cardiac phases, which could be determinant when smaller strains need to be measured (Auger et al., 2017). Fig. 2.7 shows the errors in the estimation of displacement and strain at early systole. Compared

with Fig. 2.5 (results at end-systole), the three methods showed a worse performance, leading to higher errors in the estimation of motion and strain with increased noise sensitivity. However, SP-HR and SinMod gave better results than DENSEanalysis for the estimation of strain, showing that at smaller motion levels, SP-HR and SinMod, are more accurate and less sensitive to noise.

Although the three methods were able to estimate accurately the regional  $E_{CC}$  component during the whole cardiac cycle (see Fig. 2.8) at any cardiac level, neither SP-HR, SinMod, and DENSEanalysis were able to estimate appropriately the  $E_{RR}$  component (see Figures 2.6, 2.7, and Fig. 2.8), differing severely between techniques even in the absence of noise (see Fig. 2.4). The last finding has been previously reported as an issue shared by many motion estimation techniques (Cao et al., 2018) and needs to be further studied.

When tested under realistic acquisition and motion conditions, the motion estimated with SP-HR failed in apical levels, where the torsion of the phantom was larger than the basal and mid-levels. Torsion augmentation implies an increment of relative displacement between frames, causing more errors in HARP-based methods (X. Liu & Prince, 2010). This behavior was observed in either SinMod and DENSEanalysis. Additionally, the three methods estimated accurately the mean regional  $E_{CC}$  strain component (except for SP-HR at the apex) but not the  $E_{RR}$  (see Fig. 2.8). Furthermore, the estimation of the  $E_{RR}$  made using SP-HR and SinMod differed severely from the reference values, while DENSEanalysis worked significantly better.

The estimation of the  $E_{RR}$  strain component and its reproducibility is still under study (Augustine et al., 2013; Swoboda, Larghat, Greenwood, & Plein, 2011; Haggerty et al., 2013). The inaccuracy in the estimation of the radial strain component is generated mainly by the lack of resolution and the small number of pixels in the radial direction of the LV. This is even worsened by the bandpass filters applied to the images to isolate the harmonic part in CSPAMM, and remove the remaining energy of the complex-conjugate echo in DENSE. However, in this study we found that the radial strain estimated from DENSE images using DENSEanalysis gave the most accurate estimations, which is in

corcondance with (Haggerty et al., 2013) and could be explained by the direct encoding of the displacement into the images (the number of the intermediate steps needed to recover the motion field is minimized).

As a side product of this study, we developed an open-source and flexible Python library to generate synthetic CSPAMM and DENSE images from 3D phantoms. Our library also include variables such as field inhomogeneities, dynamic flip angles, and EPI-like artifacts (among others) to each imaging mode. Another feature is that it can be easily modified to add new imaging techniques. In our case, as we are interested in studying the estimation of motion and strain, future work is the implementation of the Strain-Encoded (SENC) MRI sequence (Osman et al., 2001). PyMRStrain is freely available at [github.com/hmella/pymrstrain](https://github.com/hmella/pymrstrain).

Although it is out of the scope of this paper, the current approach could also be used to interrogate feature tracking techniques applied to images acquired in standard MRI protocols (i.e., bSSFP images). With the current framework, spatially varying isochromats density or tissue properties could be used to introduce features to the images to make it suitable for these techniques

The estimation of motion from both CSPAMM and DENSE images was chosen to consider its similarities related to the MR pulse sequence. Although the DENSE sequence is not yet available across all platforms, its development as a research tool has converted it into a powerful technique for estimating motion. We chose SP-HR, SinMod, and DENSEanalysis as postprocessing techniques because they have implementations commercially and freely distributed, and therefore, have been widely used in the MR community (E.-S. H. Ibrahim, 2011). Regarding the postprocessing techniques, although SinMod was implemented following as exact as possible, the steps and algorithms proposed by the developers, the possibility of some variability between our implementation and commercially available software should be considered.

A limitation of the current study was the lack of tissue surrounding the LV, which can impact negatively the motion estimation. In such case, any method can suffer from artifacts at the interfaces due to differences in tissue properties, discontinuities in the motion field, and loss of signal. Due to the partial volume effect, the three issues described before can bias the motion maps estimated with any technique, introducing unlikely displacements. By construction, SinMod can deal better with these issues because correct unlikely displacements using a quality model (Arts et al., 2010), while phase-based postprocessing techniques such as SP-HR and DENSEanalysis relies on the local information of each pixel. In this investigation, only the loss of signal was considered in the framework.

In conclusion, SinMod and DENSEanalysis showed excellent and comparable results for the estimation of displacements and  $E_{CC}$  strain from CSPAMM and DENSE data when we used typical image resolutions and imaging parameters. In contrast, SP-HR tends to fail for large amplitude motions, although it worked well in any other case. Additionally, we showed that the three techniques could not accurately estimate the radial strain component accurately, even when motion estimated from DENSE images using DENSEanalysis showed the best performance.

## **2.6. Acknowledgments**

The authors thankfully acknowledge the financial support of the ANID Ph. D. Scholarship 21170592 as well as the following projects and institutions: ANID-FONDECYT 1181057, ANID-FONDECYT Postdoctorado 3170737, ANID-FONDECYT de Iniciación en Investigación 11200481, ANID-Millennium Science Initiative Program-NCN17\_129.

### 3. SECOND ARTICLE: A NEW METHOD FOR MOTION ESTIMATION

#### 3.1. Title and authors

HARP-I: A Harmonic Phase Interpolation Method for the Estimation of Motion from  
Tagged MR Images

*Hernán Mella*<sup>1,2,14</sup>, *Joaquín Mura*<sup>3,14</sup>, *Hui Wang*<sup>4,5</sup>, *Michael D. Taylor*<sup>6</sup>, *Radomir Chabiniok*<sup>7,8,9,10</sup>, *Jaroslav Tintera*<sup>11</sup>, *Julio Sotelo*<sup>12,14</sup>, and *Sergio Uribe*<sup>1,2,13,14</sup>

<sup>1</sup> Department of Electrical Engineering, Pontificia Universidad Católica de Chile, Santiago, Chile.

<sup>2</sup> Biomedical Imaging Center, Pontificia Universidad Católica de Chile, Santiago, Chile.

<sup>3</sup> Department of Mechanical Engineering, Universidad Técnica Federico Santa María, Santiago, Chile.

<sup>4</sup> Philips, Cincinnati, Ohio, USA.

<sup>5</sup> Department of Radiology, Cincinnati Children's Hospital Medical Center, Cincinnati, Ohio, USA.

<sup>6</sup> Heart Institute, Department of Pediatrics, Cincinnati Children's Hospital Medical Center, Cincinnati, Ohio, USA.

<sup>7</sup> Inria, France.

<sup>8</sup> LMS, Ecole Polytechnique, CNRS, Institut Polytechnique de Paris, France.

<sup>9</sup> Department of Mathematics, Faculty of Nuclear Sciences and Physical Engineering, Czech Technical University, Prague, Czech Republic.

<sup>10</sup> Division of Pediatric Cardiology, Department of Pediatrics, UT Southwestern Medical Center, Dallas, USA.

<sup>11</sup> School of Biomedical Engineering, Universidad de Valparaíso, Valparaíso, Chile.

<sup>12</sup> Institute for Clinical and Experimental Medicine, Prague, Czech Republic.

<sup>13</sup> Department of Radiology, School of Medicine, Pontificia Universidad Católica de Chile, Santiago, Chile.

<sup>14</sup> Millennium Nucleus for Cardiovascular Magnetic Resonance, ANID-Millennium Science Initiative Program, Santiago, Chile.

Article published in the IEEE Transactions on Medical Imaging journal (impact factor of 10.048).

### **3.2. Introduction**

diseases are one of the leading causes of death globally (World Health Organization, 2018). Most of these diseases induce changes in the functionality of the cardiac muscle, leading to abnormal ventricular contractions (Götte et al., 2006; Schuster, Paul, et al., 2013; Mangion et al., 2019). The assessment of the global cardiac morphology and function has been extensively used for the diagnosis of cardiopathies. However, these metrics can suffer from preload and afterload dependency, geometric assumptions, moderate reproducibility, and its prediction capabilities are affected by conditions such as diabetes and hypertension (Cikes & Solomon, 2016), or congenital heart diseases (Burkhardt et al., 2017). Cardiac strain, on the other hand, is an advanced measure of the cardiac function with good reproducibility (Schuster, Morton, et al., 2013), which has demonstrated to be a powerful tool for the assessment and diagnosis of several cardiac diseases, such as heart failure, cardiomyopathies, dyssynchrony, abnormal pressures, and valve lesions (Chitiboi & Axel, 2017). Moreover, cardiac strain has the potential to detect subtle decreases in contractility not seen by ejection fraction. Therefore, accurate time resolved maps of the motion and deformation of the heart walls are needed for a better diagnosis and understanding of these diseases.

Currently, echocardiography is the most widely used technique to study areas in the left-ventricular walls with reduced functionality by estimating cardiac strain. (Chitiboi & Axel, 2017; Amzulescu et al., 2019). However, this technique suffers from low Signal-to-Noise Ratio (SNR), poor acoustic windows (L. Chen, 2001), geometric assumptions in the bidimensional case (Salgo et al., 2012), and high inter-observer variability depending

on the image quality (Nagata et al., 2018). Tagged Magnetic Resonance Imaging (MRI) has also been used for the assessment of the cardiac function (A. Young, 2006). In this technique, a grid pattern generated over the tissue at the beginning of the cardiac cycle (by a selective saturation of the tissue in the form of lines) follows the cardiac motion, allowing the tracking of the cardiac walls with temporal resolutions in the range of 30 to 50 msec.

At the beginning of the cardiac cycle, tag-lines in tagged images are parallel and equispaced. In the spatial frequency domain, this behavior is expressed as several spectral peaks with harmonic frequencies, which become wider due to the tissue contraction and energyless as the magnetization relaxes. Several techniques have been developed to acquire tagged MR images. One of the earlier approaches combined a series of selective RF pulses to create saturation bands on the cardiac tissue (Zerhouni et al., 1988). A year later, the Spatial Modulation of Magnetization (SPAMM) was introduced (Axel & Dougherty, 1989a), which employed a position encoding gradient and two non-selective RF pulses to rapidly saturate the magnetization. A significant improvement was made with the Complementary SPAMM (CSPAMM) sequence (Fischer et al., 1993), which using two SPAMM acquisitions, removed the non-tagged signal from the image at the cost of doubling the acquisition time. Additionally, other techniques have been introduced, such as high-order SPAMM, slice-following CSPAMM, DANTE, and variations of both of them (Fischer et al., 1994; Axel et al., 2005).

Lately, new acquisition strategies were developed to acquire 3D tagging data. In (Ryf et al., 2002) a 3D CSPAMM sequence was proposed to estimate 3D cardiac motion, taking 16 minutes to acquire all the information. A further improvement was made in (Rutz et al., 2008), where an accelerated 3D CSPAMM was introduced, allowing the acquisition of the whole heart in only 3 breath-holds of 18 heart-beats duration each.

With the advances in the imaging sequences, many motion estimation strategies based on the image intensity or its k-space were developed. In the first group, tag-lines tracking, optical flow, and image registration methods, which use intensity models and brightness constraints, are found (Guttman, Prince, & McVeigh, 1994; A. A. Young, 1999; Dougherty, Asmuth, Blom, Axel, & Kumar, 1999; Chandrashekara, Mohiaddin, Razavi, & Rueckert, 2007). Additionally, although computationally expensive, the image registration problem has been enriched with biomechanical models of the heart to improve the tracking outcome (Genet et al., 2018; Škardová et al., 2019). The other group of techniques are those based on the identification and filtering of the harmonic spectral peaks, such as the Harmonic Phase (HARP) analysis (Osman et al., 1999, 2000), Sine-Wave Modeling (SinMod) (Arts et al., 2010) technique, and Gabor filter banks (Qian et al., 2006; T. Chen & Axel, 2006). The three methods use bandpass filters to obtain images containing motion information processed in three different ways: HARP estimates motion using local approximations of the phase gradient, SinMod does it using power spectrums, and Gabor filter banks detecting tag-lines changes through several k-space filtered images (H. Wang & Amini, 2012). However, until today, the most used techniques are HARP analysis and SinMod method.

Since its initial development, several approaches have been proposed to improve the capabilities of HARP, including the Improved HARP (Khalifa, Youssef, & Osman, 2005), Extended HARP (Tecalão et al., 2006), dense multiscale HARP (Florack, Van Assen, & Suinesiaputra, 2007), seeded region growing refinement (X. Liu, Murano, Stone, & Prince, 2007), shortest path HARP refinement (X. Liu & Prince, 2010) (SP-HR), and HARP tracking with locally uniform deformation assumption (ElDeeb & Fahmy, 2016), which using spatial and/or temporal constraints, were developed to fix tracking issues due to large deformations between image frames, through-plane motion, and tissue boundaries. For SinMod, few improvements have been proposed (at least for the author knowledge), being worth to mention the robust and accurate center-frequency estimation (RACE) algorithm (H. Liu et al., 2014) and the multilevel B-splines based method (H. Wang & Amini, 2011).

Additionally, HARP and SinMod have been successfully extended to work with 3D data (Ryf et al., 2002; Moerman et al., 2011; H. Wang & Amini, 2013).

Although HARP-based techniques and SinMod are good methods for estimating motion and strain, both techniques are affected by different issues: HARP could be sensitive to the image quality (Arts et al., 2010), SinMod over-estimates strain and angular motions (E. S. H. Ibrahim et al., 2018), and both can be very sensitive to DC contamination, as will be shown later. To tackle the issues described above, a robust and fast Harmonic Phase Interpolation method (HARP-I) is introduced. Similar to HARP and SinMod, our proposed method operates using bandpass filters to obtain the harmonic phase of the image. Then, unlike HARP-based methods and SinMod, the whole phase is corrected from wrapping artifacts and temporal inconsistencies, which leads to a function that moves accordingly with the heart motion. Finally, the displacement field on a reference domain is obtained using a Radial Basis Functions (RBF) interpolation scheme defined on unwrapped phases.

In this study, we introduce HARP-I and compare its performance against SP-HR and SinMod using numerical phantoms and tagged MR images from 24 volunteers. We also present a sensitivity assessment under ideal (noise-free) and non-ideal (noisy) image conditions.

### **3.3. Methods**

#### **3.3.1. Principle of HARP-I**

The HARP-I method is based on the same principle as SP-HR but using a different approach to estimate motion. Assuming that the harmonic phase of tagged images (corrected from wrapping artifacts) moves accordingly with the tissue (Osman et al., 1999, 2000), the unwrapped phase of images tagged in orthogonal directions are used to define a new virtual coordinate system. Then using an interpolation scheme, motion maps are obtained on a fixed reference system.

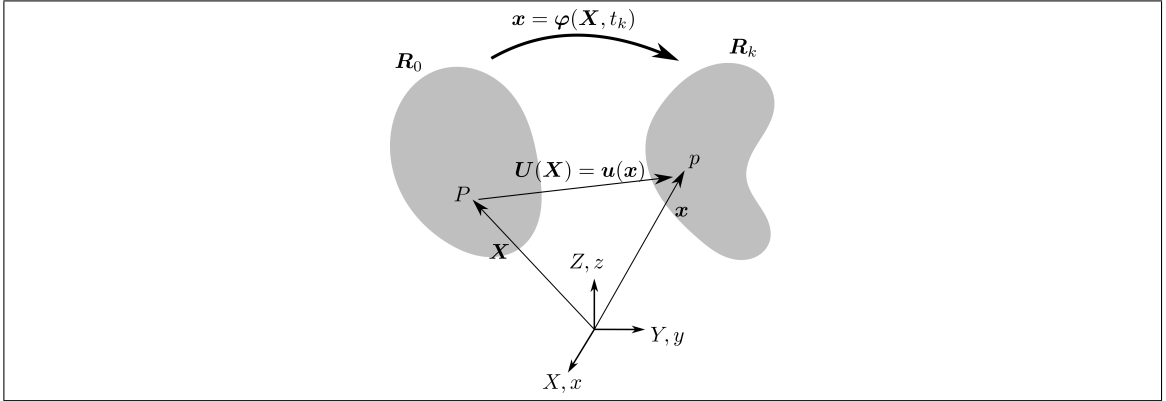


Figure 3.1. Representation of motion of a continuum body. The motion of the body  $\mathbf{R}_0$  is completely defined through the deformation map  $\varphi$ , which maps every material point  $\mathbf{P} \in \mathbf{R}_0$  to its position at a later state  $\mathbf{p} \in \mathbf{R}_k$ .

The motion of a continuum body  $\mathbf{R}_0$  is described using the deformation map  $\varphi$ , which maps the coordinates  $\mathbf{X} \in \mathbf{R}_0$  onto its position  $\mathbf{x} \in \mathbf{R}_k$  (see Figure 3.1). Here  $\mathbf{R}_0$  denotes the body at a reference frame (e.g., the heart at end-diastole) and  $\mathbf{R}_k$  the region of the space occupied by the body at the time  $t_k$  (Gurtin, Fried, & Anand, 2010) (e.g., the beating heart). At this point should be noticed that the following description of the method is general and can be applied to either 2D and 3D data by repeating the whole procedure to an additional dimension.

Let us consider now the pair of images  $I(\mathbf{x}, t_0)$  and  $I(\mathbf{x}, t_k)$  of a sequence of tagged MR images not necessarily subsequent, in which brightness represents an object occupying the domains  $\mathbf{R}_0$  and  $\mathbf{R}_k$  at different times. Without loss of generality, the intensity distribution of the  $k$ -th image with tag-lines in the  $X$  direction was modeled as

$$I(\mathbf{x}, t_k) = A(t_k) \cos(\Omega X(\mathbf{x}, t_k)) + n(\mathbf{x}, t_k) \quad (3.1)$$

where  $\Omega$  represents the spatial frequency of the sinusoidal tag pattern,  $A$  the image intensity depending on time  $t_k$ , and  $n$  the noise contributions which depend separately of  $\mathbf{x}$  and  $t_k$  (i.e. vary with the position and time). Then, isolating the harmonic part of the image in (3.1) using a bandpass filter in the frequency domain  $[\omega_x, \omega_y]$  with central frequency  $\Omega$ ,

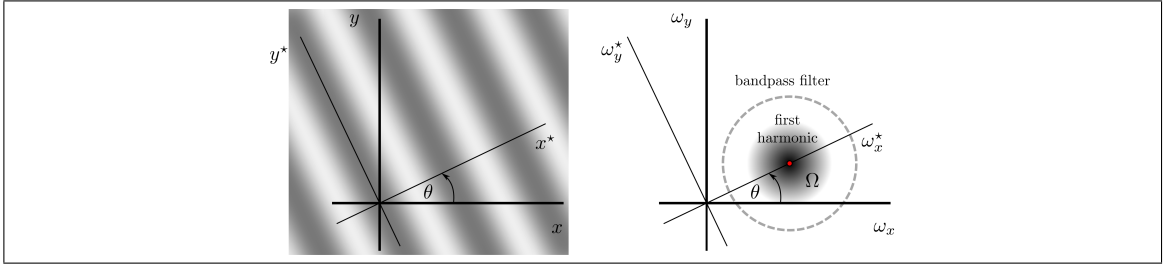


Figure 3.2. (Left image) Tagged image with tag-lines pointing towards the oblique direction  $x^*$ , given by the angulation  $\theta$ . (Right image) The Fourier transform of the tagging image gives a frequency spectrum in the domain  $[\omega_x, \omega_y]$ , with the first harmonic peak centered at a frequency  $\Omega$  over the  $\omega_x^*$  axis. The central frequency of the bandpass filter (gray broken lines) coincides with  $\Omega$ .

we obtained the harmonic image

$$I^{bf}(\mathbf{x}, t_k) = A(t_k)e^{i\Omega X(\mathbf{x}, t_k)} + n^{bf}(\mathbf{x}, t_k) \quad (3.2)$$

where  $n^{bf}$  is the bandpass filtered version of  $n$ . Taking the angle in (3.2), a wrapped version of the harmonic phase of  $I$  was obtained:

$$\phi_w(\mathbf{x}, t_k) = \angle I^{bf}(\mathbf{x}, t_k) = \mathcal{W}(\Omega X(\mathbf{x}, t_k) + n_\phi(\mathbf{x}, t_k)) \quad (3.3)$$

where  $\mathcal{W}(\phi) = \text{mod}(\phi + \pi, 2\pi) - \pi$  denotes the non-linear wrapping operator and  $n_\phi$  the phase noise induced by  $n^{bf}$ .

Following the same procedure for an image with tag-lines in the  $Y$  direction, we can obtain the wrapped phase for the two directions  $X$  and  $Y$  as:

$$\phi_w(\mathbf{x}, t_k) = \mathcal{W}(\Omega \mathbf{X}(\mathbf{x}, t_k) + \mathbf{n}_\phi(\mathbf{x}, t_k)) \quad (3.4)$$

where  $\mathbf{X}$  now denotes the two components of the reference system, and  $\phi_w$  and  $\mathbf{n}_\phi$  (in bold) the vectorial versions of the wrapped phases and noise components.

Differing from SP-HR, we corrected the wrapping artifacts in (3.4) to obtain a phase  $\phi$  that depends directly on the Eulerian (spatial) description of the reference position  $\mathbf{X}$ ,

given by:

$$\phi(\mathbf{x}, t_k) = \Omega \mathbf{X}(\mathbf{x}, t_k) + \mathbf{n}_\phi(\mathbf{x}, t_k) + 2\pi \mathbf{c}_k \quad (3.5)$$

where  $2\pi \mathbf{c}_k$  is a constant vector on  $\mathbf{R}_k$  (with  $\mathbf{c}_k$  a vector of integers) denoting the fact that phases obtained from the unwrapping procedure are not temporally consistent and can differ by a multiple of  $2\pi$ .

Using the first phase as reference (i.e., we assumed  $\mathbf{c}_0 = \mathbf{0}$ ), the reference coordinates are related with the new virtual system as:

$$\mathbf{X}_V(\mathbf{x}, t_k) = \phi(\mathbf{x}, t_k) - \mathbf{c}_k = \Omega \mathbf{X}(\mathbf{x}, t_k) + \mathbf{n}_\phi(\mathbf{x}, t_k) \quad (3.6)$$

where  $\mathbf{X}_V(\mathbf{x}, t_k)$  is a function that depends on noisy measurements of the reference position  $\mathbf{X}(\mathbf{x}, t_k)$  on  $\mathbf{R}_k$  (further details regarding the estimation of  $\mathbf{c}_k$  are discussed later).

Using this new reference system, we defined a multivariate RBF interpolation scheme for noisy scattered data to map deformed coordinates into its reference description (Buhmann, 2003). Thus, the interpolation scheme was defined as:

$$\mathbf{g}(\mathbf{y}) = \sum_{i=1}^{N_{\text{pixels}}} \lambda_i \cdot \psi(\|\mathbf{y} - \mathbf{X}_V(\mathbf{x}_i, t_k)\|) \quad (3.7)$$

where  $N_{\text{pixels}}$  denotes the number of pixels in the image,  $\mathbf{g}(\mathbf{y})$  the interpolated function at the point  $\mathbf{y}$  (with  $\mathbf{y}$  a variable that can be evaluated at any point of the virtual system),  $\psi(\|\mathbf{y} - \mathbf{X}_V(\mathbf{x}_i, t_k)\|)$  a radial basis function centered at  $\mathbf{X}_V(\mathbf{x}_i, t_k)$ , and  $\lambda_i$  the weighting factor associated with the  $i$ -th basis function.

Instead of constructing the exact interpolation of polluted measurements (see Appendix A), we seek the approximation  $\hat{\mathbf{g}}(\mathbf{X}_V(\mathbf{x}_i, t_k)) \approx \mathbf{x}_i$ , using (Poggio & Girosi, 1990):

$$(\Psi + \eta \mathbf{I}) \boldsymbol{\lambda} = \mathbf{G} \quad (3.8)$$

where  $\eta > 0$  is a regularization constant that ensures the non-singularity of the system,  $\mathbf{I}$  the identity matrix,  $\boldsymbol{\lambda}$  a vector of weights, and  $\mathbf{G}$  a vector of measurements (details about the matrix  $\Psi$  are in the Appendix B.1).

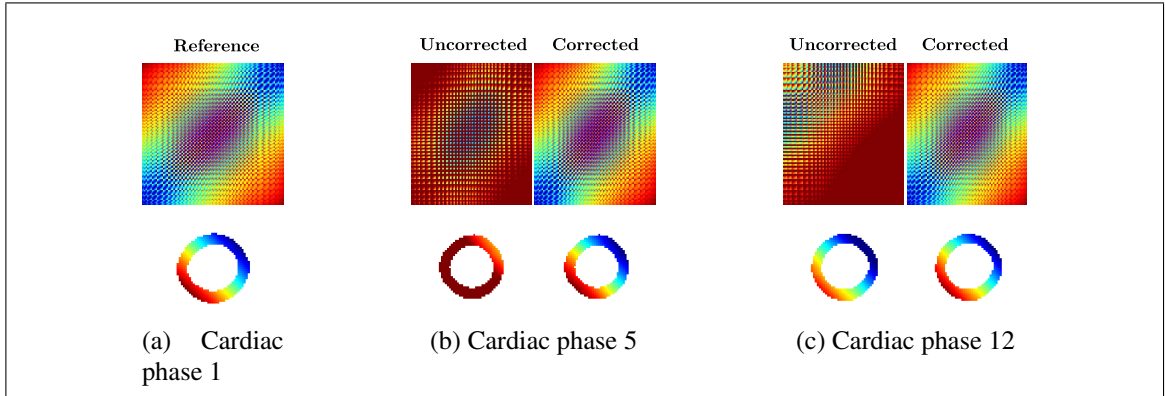


Figure 3.3. Phase-distance matrices (upper row) and the corresponding unwrapped harmonic phases (bottom row). Figure (a) shows the distance matrix and phase for the reference frame, whereas (b) and (c) show the uncorrected (left) and corrected (right) distance matrices and phases for frames 5 and 12. The matrices were obtained from an image of a healthy volunteer with taglines in the direction given by  $\theta = 45^\circ$  (see Figure 3.2) and using only the pixels inside the LV (this explains why the matrix size is square in (a) but non-square in (b) and (c). See (3.11) for the definition of distance matrices). The colors on all the plots share the same scale.

After solving (3.8), the interpolator in (3.7) was evaluated at  $\mathbf{X}_V(\mathbf{X}, t_0)$ , allowing the estimation of the deformed position of the object  $\mathbf{R}_k$  on the reference configuration  $\mathbf{R}_0$  (see Appendix B). Finally, the displacement field  $\mathbf{U}$  of the object  $\mathbf{R}_0$  between the times  $t_0$  and  $t_k$  was easily estimated using

$$\mathbf{U}(\mathbf{X}, t_k) = \varphi(\mathbf{X}, t_k) - \mathbf{X} \quad (3.9)$$

### 3.3.2. Strategies for correcting temporal phase inconsistencies

For a proper estimation of displacements,  $c_k$  is estimated using  $\phi_1$  as reference phase.

**Exploding the structure of the distance matrices:** as we treat the harmonic phases as a material property, both of the following distance matrices should always have a similar

structure:

$$r_{mn}^{\text{ref}} = \|\mathbf{X}_V(\mathbf{X}_m, t_0) - \mathbf{X}_V(\mathbf{X}_n, t_0)\| \quad (3.10a)$$

$$r_{mn}^k = \|\mathbf{X}_V(\mathbf{X}_m, t_0) - \mathbf{X}_V(\mathbf{x}_n, t_k)\| \quad (3.10b)$$

However, due to the phase jumps between temporal frames, the previous assertion is not valid (see Figure 3.3).

Phase inconsistencies are ligated to the constant  $c_k$ , and can be fixed by ensuring the similitude between  $\mathbf{r}^{\text{ref}}$  and  $\mathbf{r}^k$ . This condition is imposed through the coming optimization problem:

$$\arg \min_{c_k} \left\{ \left| \min_{m,n} r_{mn}^{\text{ref}} - \min_{m,n} r_{mn}^k \right| \right\} \quad (3.11)$$

where  $c_k$  is defined implicitly on  $\mathbf{r}^k$  through  $\mathbf{X}_V(\mathbf{x}_n, t_k)$  (see (3.6)). This approach does not introduce any restriction on the temporal resolution and can be used on either segmented or non-segmented cardiac geometries.

### 3.3.3. Application of HARP-I in oblique directions

Although the whole process consider tag-lines in the directions  $x$  and  $y$ , we can also apply HARP-I in oblique directions  $x^*$  and  $y^*$  (see Figure 3.2). Defining the angulation of the tag-lines as  $\theta$ , the deformed and frequency coordinates  $[x^*, y^*]$  and  $[\omega_x^*, \omega_y^*]$  (respectively) are defined by:

$$\begin{bmatrix} x^* \\ y^* \end{bmatrix} = \begin{bmatrix} \cos \theta & \sin \theta \\ -\sin \theta & \cos \theta \end{bmatrix} \begin{bmatrix} x \\ y \end{bmatrix} \quad (3.12a)$$

$$\begin{bmatrix} \omega_x^* \\ \omega_y^* \end{bmatrix} = \begin{bmatrix} \cos \theta & \sin \theta \\ -\sin \theta & \cos \theta \end{bmatrix} \begin{bmatrix} \omega_x \\ \omega_y \end{bmatrix} \quad (3.12b)$$

Thus, replacing  $\mathbf{x}$  by  $\mathbf{x}^* = [x^*, y^*]$  and  $\boldsymbol{\omega}$  by  $\boldsymbol{\omega}^* = [\omega_x^*, \omega_y^*]$  in (3.1) to (3.9) all the procedure remains valid.

### 3.3.4. Implementation of HARP-I

HARP-I method, listed in (3.1) to (3.9), was implemented in MATLAB (The MathWorks, Inc., Natick, Massachusetts). Similar to SP-HR and SinMod, Fast Fourier Transform (FFT) was applied to two input images (not necessarily subsequent)  $I_1$  and  $I_k$  with tag-lines in the direction  $x^*$  (or  $y^*$ ) (see Figure 3.2), leading to frequency spectrums in the  $[\omega_x^*, \omega_y^*]$  domain. The center of the region containing the first harmonic component of the images was identified as  $[\Omega_x, \Omega_y]$ , and the central frequency  $\Omega$  and the tag-lines angulation  $\theta$  (see Figure 3.2) were calculated using:

$$\Omega = \sqrt{\Omega_x^2 + \Omega_y^2}, \quad \theta = \arccos\left(\frac{\Omega_x}{\Omega}\right) \quad (3.13)$$

In practice, we identify just one harmonic component and choose the second direction to be perpendicular to the first one.

The harmonic phases given in (3.4) were corrected from wrapping artifacts using a *quality-guided path following* unwrapping algorithm (Ghiglia & Pritt, 1998), which has been previously used for the estimation of displacements from DENSE images (Gilliam & Epstein, 2012; Spottiswoode et al., 2007).

In our implementation we tested several families of RBF, such as Wendland's, Wu's, splines, Gaussians, and multiquadrics, being the last which had better smoothing properties without comprising the quality of the estimation. Therefore, we used a third-order multiquadric RBF given by

$$\psi(r) = (r^2 + a^2)^{3/2}, \quad a \in \mathbb{R} \quad (3.14)$$

where  $a$  is a constant that controls the smoothing during the interpolation process (Carr et al., 2003). The value of  $a$  used on all the experiments (with synthetic data and real images) was empirically determined as

$$a = \frac{150}{N^o \text{ pixels per wavelength}} = \frac{150\Delta x}{2\pi/\Omega} \quad (3.15)$$

where  $\Delta x$  denotes the pixel size. The key idea behind this choice is that as the number of pixels-per-wavelength decreases, higher frequency components are present in the filtered images and therefore, the amount of smoothing should increase.

### 3.3.5. Implementation of SP-HR and SinMod

To compare our method with other processing techniques, we used SP-HR and implemented SinMod methods as described in Osman *et al.* (Osman et al., 1999, 2000; X. Liu & Prince, 2010) and Arts *et al.* (Arts et al., 2010), respectively. In the case of SP-HR, the source code was provided by the Image Analysis and Communication Lab at Johns Hopkins University. For the SinMod method, the implementation was done in accordance with (Arts et al., 2010; H. Wang & Amini, 2013). The local quality model proposed by the authors, consisting on a weighted hanning windowing of the power spectrum based on an intensity-based quality measure, was used to correct the motion estimation. The size of the hanning window was set to 15 and the power of the quality measure was chosen as 8.

Motion with SinMod was estimated in a frame-by-frame basis using two consecutive images, and tracked backward to a reference frame using a Thin-Plate spline interpolation. For the estimation of strain, no smoothing techniques were applied to the estimation of spatial derivatives. However, a 10th order polynomial was fitted to each component of the estimated motion to slightly smooth the tissue trajectories (Spottiswoode et al., 2007; Zhong et al., 2010; Wehner et al., 2018).

For the sake of fairness during the comparison, we used the same Butterworth band-pass filter (H. Wang & Amini, 2013) for the three methods, choosing the frequency-cutoff and decay order accordingly to ensure, as far as possible, the removal of higher harmonics and the DC component. The central frequency  $\Omega$  of the filter was defined as the tag-lines frequency.

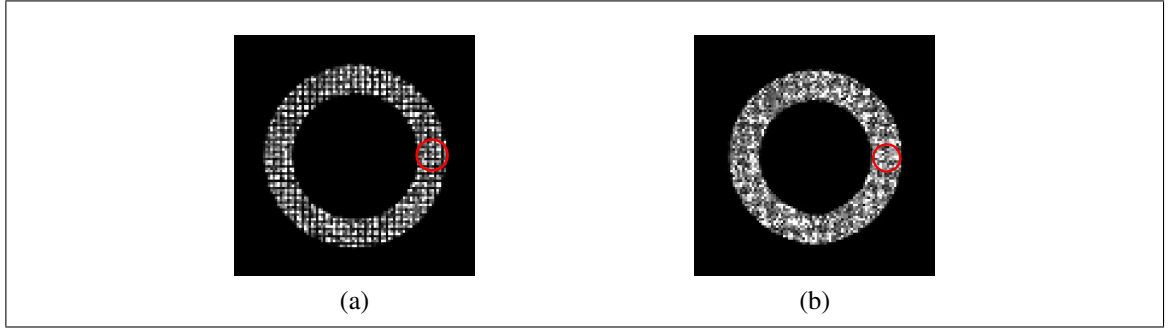


Figure 3.4. (a) First and (b) last frames of a noisy synthetic data. The red circle denotes the place where the stiffer inclusion was added. The contrast of the images (see Eq. 3.16) was set differently for a better visualization. Both images were obtained using the  $WL_5$

### 3.4. Experiments

#### 3.4.1. In-silico experiments

SP-HR, SinMod, and HARP-I were tested using a synthetic 2D dataset of 10 different idealized left-ventricular geometries. The intensity model used was similar to the given in Eq. 3.1 but with a decaying tagged and growing non-tagged terms as follows:

$$I(\mathbf{x}, t_k) = 1 - e^{-t_k/T1} + e^{-t_k/T1} \cos(\Omega X(\mathbf{x}, t_k)) \quad (3.16)$$

where  $T1 = 0.72$  denotes a relaxation parameter chosen to achieve a 75% of signal decay of the tagged part in the last frame. Each image was generated with a resolution of  $200 \times 200$  pixels. The intensity model given in Eq. 3.16 emulates the signal of tagging MR images without DC correction (E.-S. H. Ibrahim, 2011).

The motion pattern of the idealized geometries combines angular and non-uniform radial displacements with a stiffer inclusion to simulate an abnormal contraction (see Figure 3.4). Motion maps were estimated under noise-free and noisy conditions, and all the experiments were performed using wavelengths of 2.9, 4.9, and 6.9 pixels, namely  $WL_3$ ,  $WL_5$ , and  $WL_7$  respectively.

The maximum angular and radial displacements of the inner wall,  $\Delta\theta$  and  $\Delta r$  respectively, vary across data following:

$$\Delta\theta = \frac{WL_i}{2r}, \quad \Delta r = \frac{WL_i}{2} \quad (3.17)$$

where  $WL_i$  is the wavelength of the intensity model ( $i = 4, 5, 7$ ) and  $r$  the inner radius. For the outer displacements, no angular motion was imposed and the maximum radial motion was estimated in order to ensure an isochoric deformation. The spatial variation of the motion pattern across the wall (between the inner and outer radius) was chosen to be linear, with a stiffer additive inclusion to simulate an abnormal contraction. The maximum displacement was applied in increments of  $0.1WL_i$ , i.e., six motion levels per data were simulated, being the maximum displacement achieved in the last frame.

To investigate the behavior of the three methods with low SNR images, additive uncorrelated white Gaussian noise with standard deviation 0.06 was added to both real and complex channels of all the images (see Figure 3.4).

### 3.4.2. In-vivo experiments

Finally, we tested and compared the three methods on a short-axis view of the left ventricle (different cardiac levels) of 23 volunteers (19 males of  $28 \pm 15$  years and 4 females of  $50 \pm 21$  years of which 9 were acquired on a 1.5T Ingenia system (Philips, Best, Netherlands), 4 on a 1.5T Achieva system (Philips, Best, Netherlands), and 10 on a 1.5T Avanto Fit system (Siemens Healthineers, Erlangen, Germany). The spacings of the tag-lines were  $4.5 \pm 0.8$  pixels per wavelength.

Additionally, to demonstrate the functionality of HARP-I on 3D data, the method was tested on a 3D CSPAMM image of one healthy volunteer (male, 66 years old) acquired on a 1.5T Achieva system (Philips, Best, Netherlands). After alignment and resampling of the volumes in each direction, the size of the reconstructed matrix was  $112 \times 112 \times 112$  with a voxel size of  $0.96 \times 0.96 \times 1.12 \text{ mm}^3$ . The tag spacing was 7 mm in each direction. For further details about the acquisition, please refer to (Rutz et al., 2008).

Table 3.1. Diagnoses and/or MRI findings for subjects with abnormal ventricular contraction

Identifier	Sex	Age	Diagnosis/Specialist impression
2*	M	21	Mildly decreased LV ejection fraction (EF 50%).
4*	F	69	Severely decreased LV systolic function. Dyskinetic motion of apex (with thrombus present). Possible hypertrophic cardiomyopathy in septum at LV outflow tract.
7*	M	43	Globally hypokinetic LV.
10	M	12	Duchenne muscular dystrophy.
11	M	30	Duchenne muscular dystrophy.
12	M	11	Duchenne muscular dystrophy.
13	M	12	Hypertrophic cardiomyopathy.
14	M	13	Duchenne muscular dystrophy.

Each subject identifier is accompanied by its respective diagnosis and/or MRI finding. Diagnoses were made by a cardiologist with expertise in cardiovascular MRI, while MRI findings were made by a medical doctor with more than 5 year experience with clinical cardiovascular MRI. These identifiers will be used in the rest of the article to refer to the data.

\*: MRI finding; M: male; F: female; EF: ejection fraction.

The acquisition of all the subjects was approved by the Institutional Review Boards at Pontificia Universidad Católica de Chile (Santiago, Chile), Cincinnati Children’s Hospital Medical Center (Ohio, USA), and the Institute for Clinical and Experimental Medicine (Prague, Czech Republic). The dataset was composed of 16 healthy volunteers (including the 3D data) and 8 patients with known cardiopathies. In Table 3.1, a summary of the diagnoses and/or MRI findings of the subjects can be found.

### 3.4.3. Statistical analysis

All the results presented include comparisons between reference displacements and strain, considering displacement magnitude and direction, and circumferential and radial components of the Lagrangian strain tensor (Gurtin et al., 2010). The metrics used to quantify the error were the normalized root Mean Square Error (nRMSE) and Directional

Error (DE) (Mura et al., 2016), defined as:

$$\text{nRMSE} = \frac{1}{\max\|\mathbf{a}_i^e\|} \sqrt{\frac{1}{N} \sum_{i=1}^N \|\mathbf{a}_i - \mathbf{a}_i^e\|^2} \quad (3.18a)$$

$$\text{DE} = \frac{180}{\pi N} \sum_{i=1}^N \arccos \left( \frac{|\mathbf{u}_i \cdot \mathbf{u}_i^e|}{\|\mathbf{u}_i\|_2 \|\mathbf{u}_i^e\|_2} \right) \quad (3.18b)$$

where  $\|\cdot\|$  represents the Euclidean norm,  $N$  the number of analyzed pixels in the image,  $\mathbf{a}_i$  a pixelwise scalar or vectorial quantity at pixel  $i$ , and  $\mathbf{u}_i$  the pixelwise displacement. The superscript  $()^e$  denotes the reference value. All the results reported in the succeeding section are average values of the metrics presented in Eq. 3.18a and Eq. 3.18b computed over the whole synthetic dataset ( $N = 10$ ) for each displacement level.

### 3.5. Results

In the following sections, we split the results into three parts. The first and the second comprise the in-silico results of the noise-free and noisy experiments respectively, whereas the third one reports the results from the in-vivo data.

#### 3.5.1. Noise-free experiments

Figure 3.5 shows the mean nRMSE and DE across the whole dataset calculated using the expressions given in Eq. 3.18a and Eq. 3.18b. For all the wavelengths the three methods showed a similar behavior, achieving all of them the best performance at  $\text{WL}_3$  and the worst at  $\text{WL}_7$  (see Figures 3.5a to 3.5c). Overall, the performance of HARP-I was similar to SP-HR and SinMod at any wavelength.

In terms of nRMSE and DE, the three methods showed a clear trend across all the wavelengths: the error increased with the displacement level (see Figure 3.5). However, no major differences were found in any case. The average nRMSE and DE obtained using SP-HR, SinMod, and HARP-I (across all wavelengths and displacement levels) were

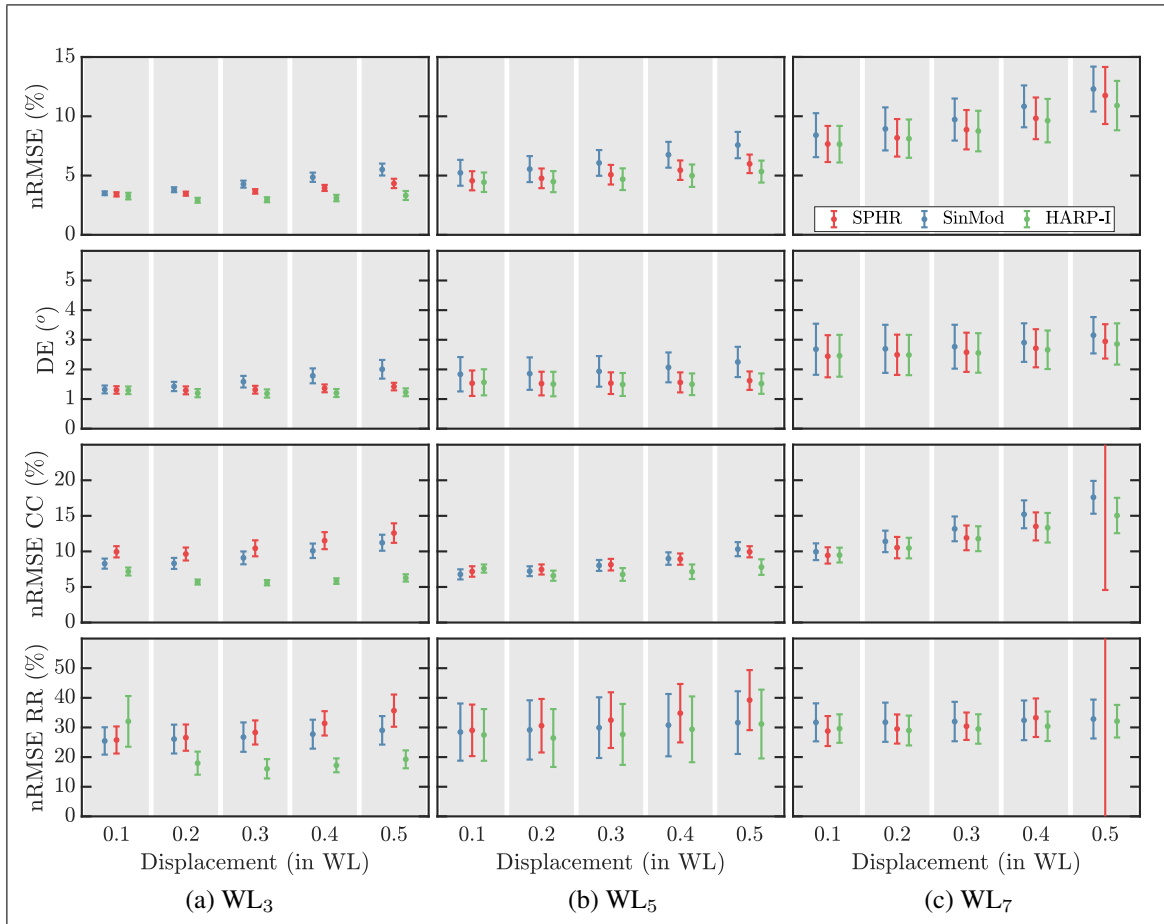


Figure 3.5. Mean errors and deviations in the estimation of displacement magnitude (first row), direction (second row), circumferential strain (third row), and radial strain (fourth row) for wavelengths of (a) 2.9 (WL<sub>3</sub>), (b) 4.9 (WL<sub>5</sub>), and (c) 6.9 (WL<sub>7</sub>) pixels. The label in the  $x$ -axis denotes the amount of radial and angular displacement of the synthetic data (in the last case, the  $x$ -axis represents  $r$  times the angular displacement, as stated by Eq. 3.17), while in the  $y$ -axis, CC and RR stand for circumferential and radial strain components. For all the displacement levels and wavelengths, the performance of HARP-I was superior than SP-HR and SinMod.

$6.1 \pm 2.5\%$  and  $1.8 \pm 0.6^\circ$ ,  $6.9 \pm 2.6\%$  and  $2.2 \pm 0.6^\circ$ , and  $5.6 \pm 2.6\%$  and  $1.8 \pm 0.6^\circ$  respectively, i.e., SP-HR and HARP-I showed slightly better performance than SinMod.

When looking at the variability in the error metrics, the behavior was similar to what was described before. The average standard deviations were  $1.0 \pm 0.7\%$  and  $0.4 \pm 0.2^\circ$  for

SP-HR,  $1.1 \pm 0.6\%$  and  $0.5 \pm 0.2^\circ$  for SinMod, and  $1.0 \pm 0.6\%$  and  $0.4 \pm 0.2^\circ$  for HARP-I, which means that almost no differences were found in terms of variability.

For both strain components, the error metrics behaved similarly to the errors in the displacement field, exhibiting a clear increasing trend with the motion levels (see third and fourth rows of Figure 3.5). However, HARP-I did not follow this trend for WL<sub>3</sub> and SP-HR achieved bigger errors in the last displacement level of the WL<sub>7</sub>. Despite the bigger errors of HARP-I at the smallest displacement for WL<sub>3</sub>, SinMod and HARP-I always achieved better performances in both strain components for WL<sub>3</sub> and WL<sub>5</sub>. For WL<sub>7</sub>, however, SP-HR performed better than SinMod but worse than HARP-I. In terms of averages (across wavelengths and displacement levels), for the circumferential strain the three methods reached errors similar to those found for displacements. However, for the radial component the error increased considerably when compared with displacement magnitude and direction, and also with the circumferential part, reaching average values of  $33.6 \pm 4.7$  for SP-HR,  $29.7 \pm 2.9$  for SinMod, and  $26.4 \pm 2.9$  for HARP-I.

In general, the three methods showed good performance estimating displacements and strains as the errors and differences between techniques were relatively small. This means that SP-HR, SinMod, and HARP-I showed a similar behavior under ideal conditions.

### 3.5.2. Noisy experiments

Figure 3.6 (first and second rows) shows the error metrics for displacement magnitude and direction in the presence of noise. When compared with the noise-free results, the three methods performed worse (as expected) but keeping a similar difference in the error metrics between techniques, although HARP-I achieved the best results at all the displacement levels.

The average error across displacements, in terms of nRMSE and DE, were  $8.0 \pm 2.0\%$  and  $2.7 \pm 0.7^\circ$  for SP-HR,  $8.4 \pm 1.9\%$  and  $2.8 \pm 0.5^\circ$  for SinMod, and  $7.1 \pm 2.1\%$  and  $2.4 \pm 0.6^\circ$  for HARP-I. When compared with the same results in the noise-free case, the

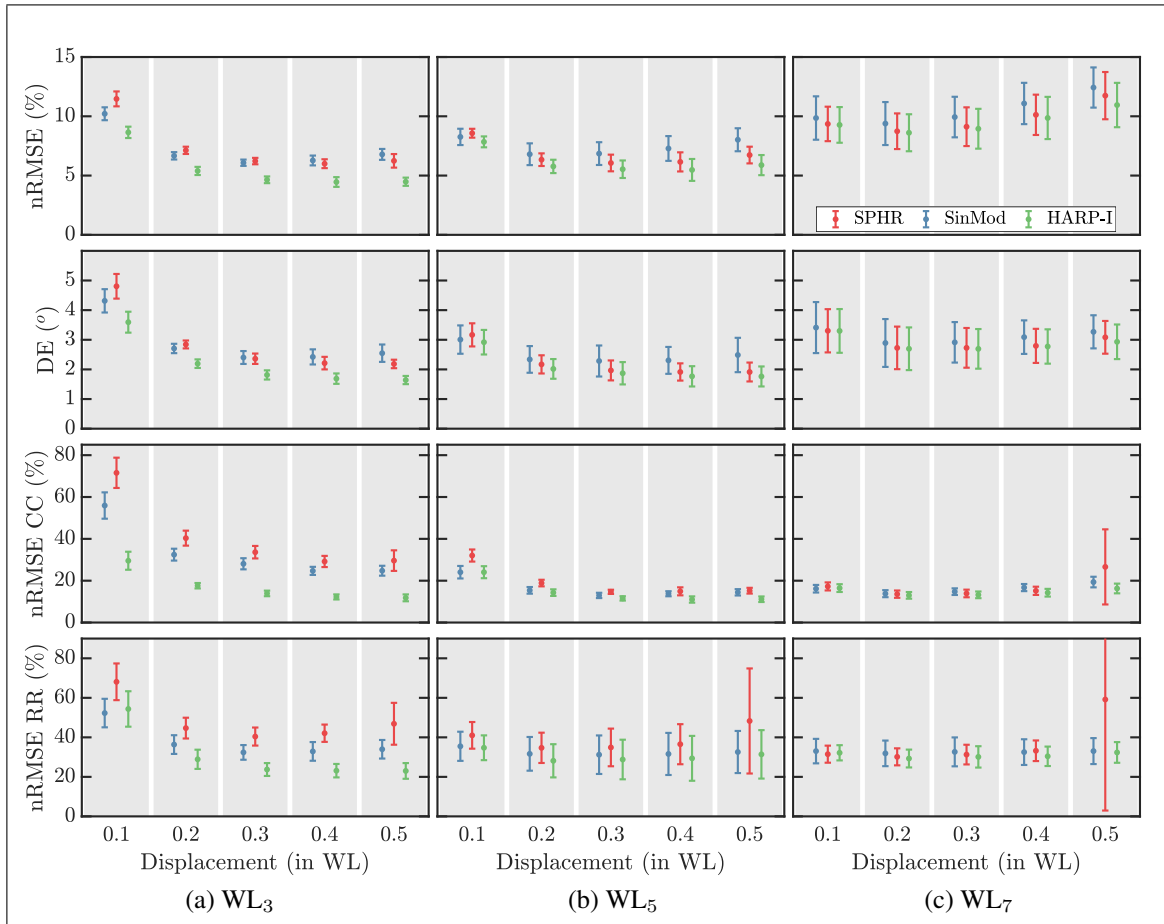


Figure 3.6. Mean errors and deviations in the estimation of displacement magnitude (first row), direction (second row), circumferential strain (third row), and radial strain (fourth row) for the noisy experiment for wave-lengths of (a) 2.9 (WL<sub>3</sub>), (b) 4.9 (WL<sub>5</sub>), and (c) 6.9 (WL<sub>7</sub>) pixels. Strain estimations obtained SP-HR, SinMod, and HARP-I followed a similar behavior than the displacement magnitude and direction. However, the error increased due to the presence of noise.

errors were 1.3 and 1.5 times greater for SP-HR, 1.2 and 1.3 for SinMod, and 1.3 and 1.3 for HARP-I, which means that SinMod was slightly less sensitive to noise in the estimation of displacements. Although the increase in the average nRMSE and DE, the variability in error across the dataset did not experience a significant increase.

Figure 3.6 (third and fourth rows) shows the error metrics for the estimation of the strain components. The circumferential and radial components were better estimated with

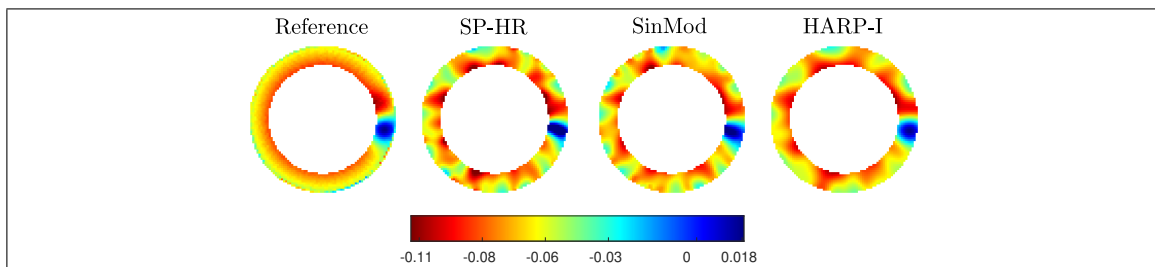


Figure 3.7. Circumferential strain maps obtained with SP-HR, SinMod, and HARP-I for one representative sample of noisy data using  $WL_5$ . Rapid spatial variations were observed in estimations made with SP-HR and SinMod, whereas more accurate and homogeneous results were obtained using HARP-I.

HARP-I, whereas SP-HR performed the worst. In the last case, similar to the noise-free case, bigger errors were induced in the estimation of strain at the last displacement level. The average errors for the circumferential and radial components were  $25.8 \pm 14.9\%$  and  $41.5 \pm 10.4\%$  for SP-HR,  $21.8 \pm 10.8\%$  and  $34.2 \pm 5.0\%$  for SinMod, and  $15.4 \pm 4.5\%$  and  $30.7 \pm 7.1\%$  for HARP-I. When compared with the noise-free experiment, errors obtained under noisy conditions were 2.3 and 1.2 times greater with SP-HR, 2.1 and 1.2 greater for SinMod, and 1.9 and 1.2 greater for HARP-I, indicating that derivatives estimated from SinMod and HARP-I results were less sensitive to noise than SP-HR.

Finally, Figures 3.7 and S1 (see Supporting Information) show the accuracy of HARP-I in the estimation of the position, shape, and strain values under noisy and noise-free conditions. Particularly, Figure S1 presents the results of an experiment conducted to determine the accuracy of HARP-I in the estimation of strain under different inclusion sizes.

### 3.5.3. Motion estimation on healthy volunteers

Figure 3.8 shows the left-ventricular strain maps of a subset of five healthy volunteers estimated using SP-HR, SinMod, and HARP-I, from tagged MR images. Although the strain maps at end-systole were similar between techniques in most cases, SP-HR gave results with severe artifacts, while SinMod and HARP-I showed smooth and similar strain

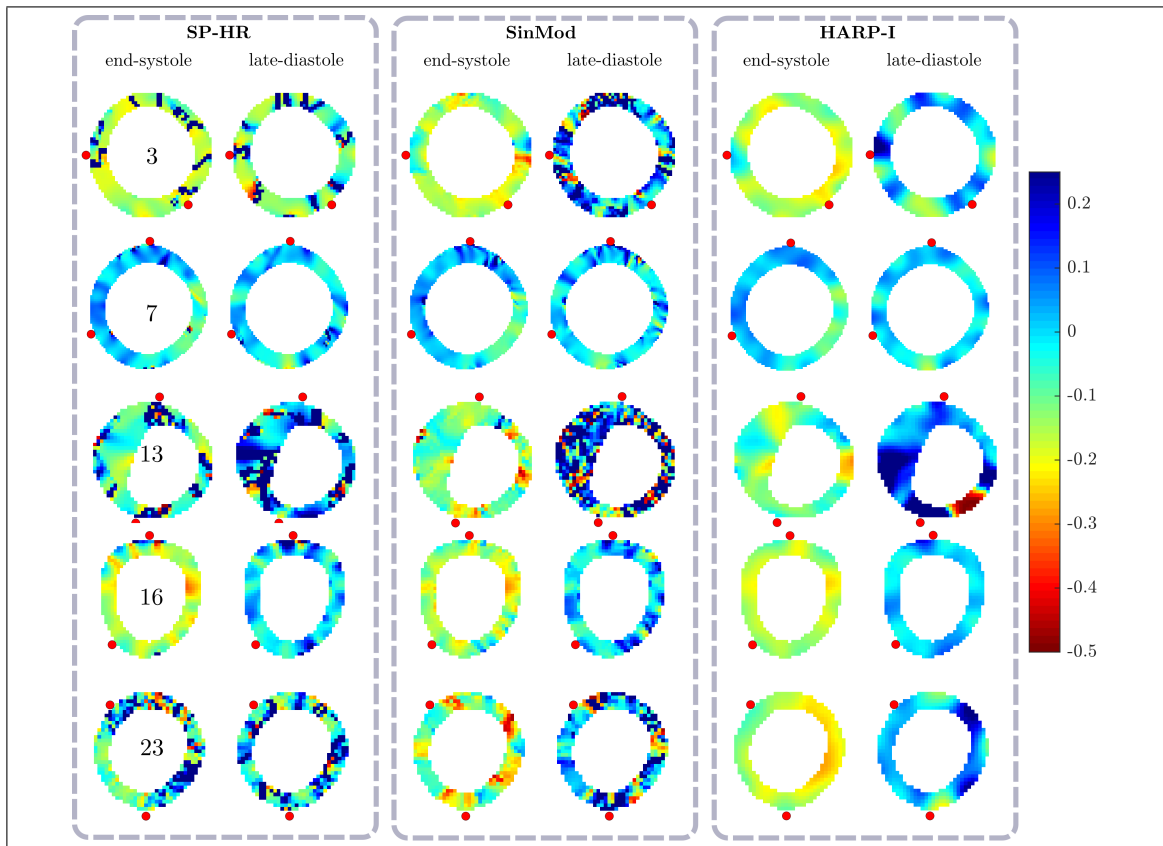


Figure 3.8. Circumferential strain of a short-axis view of the left ventricle for 5 volunteers at end-systole and late-diastole (the last frame acquired). We used late-diastole to emphasize that in ECG triggered MR images, the cardiac cycle is not completely sampled. All the maps are presented in the reference cardiac phase (first frame) and were estimated using SP-HR (left), SinMod (middle), and HARP-I (right). The red dots indicate the insertion points of the RV walls into the LV. Each volunteer was identified with a number to make it easier to refer. The volunteers 7 and 13 presented abnormal strain patterns as they presented cardiomyopathies. The first case showed a hypokinetic LV and the second hypertrophic cardiomyopathy. SP-HR showed strain maps with artifacts on 3 of the 5 cases, whereas SinMod and HARP-I showed similar results at end-systole for most of the cases. Nonetheless, at late-diastole (where cardiac strain in healthy subjects should be small as the heart relaxes and come back to its reference position) some artifacts were observed with three methods in almost all cases. However, HARP-I showed a more stable behavior across the whole cardiac cycle.

maps. At late-diastole, severe artifacts were obtained with the three techniques, but to a lesser extent with HARP-I. In the same Figure, strain maps of two patients, one with a hypokinetic LV (volunteer 7) and other with hypertrophic cardiomyopathy (volunteer 13), are presented.

To get an error measure of the motion and strain, we followed a similar approach as in (Arts et al., 2010), and for all the volunteers, we estimated the accumulated fraction of pixels with circumferential strains exceeding the unlikely high value of 50% (see Figure 3.9). For SP-HR and SinMod this metric increased to elevated levels, reaching maximum values 1.5 and 1.1 respectively. For HARP-I, on the other hand, the fraction remained always close to zero, with a maximum value of 0.02.

In Figure 3.10 the temporal strain curves obtained with the three techniques are shown. With SP-HR and SinMod, highly unlikely strain values (bigger than 0.5) were not considered for the estimation of the curves, whereas with HARP-I all the values were used. Overall, the results given by the three methods were physiologically consistent and closer to clinical values, although SP-HR not always gave good results (see volunteers 11, 13, 18, 21, 22, and 23 in Figure 3.10).

Finally, Figure 3.11 shows the estimated motion of the processed 3D data using 3D HARP-I and 3D SinMod. Each slice of the LV shows the circumferential strain and displacement field (arrows). HARP-I gave smoother strain maps than SinMod and displacements were closer to what we observed from the images. At basal level, the longitudinal displacement measured from the images was -7 and -11 pixels at the red and blue points (see Figures 3.11a and 3.11b), whereas with HARP-I was -7.2 and -10.8, and SinMod -7.6 and -13.1, which means that SinMod overestimated the longitudinal component of the displacement.

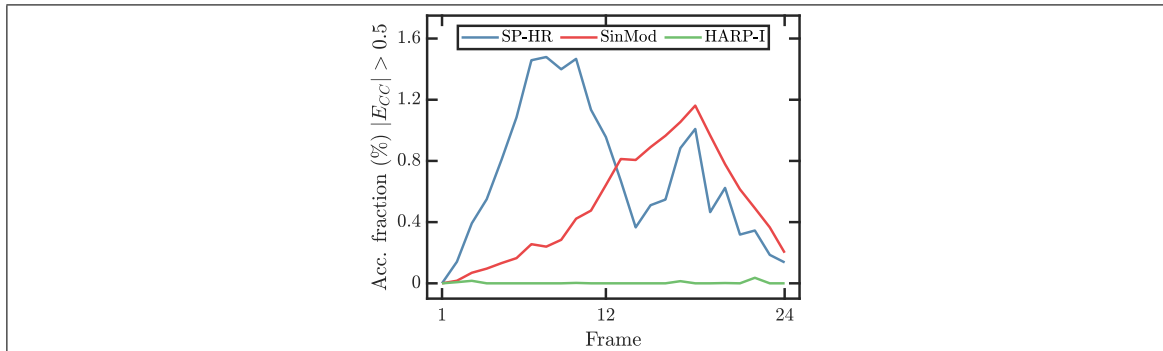


Figure 3.9. Accumulated (across all volunteers) fraction of pixels with circumferential strain ( $E_{CC}$ ) with unlikely high values. The X-axis denotes the frame of the cardiac cycle relative to the first one. The fraction was estimated as the number of pixels satisfying  $|E_{CC}| > 0.5$  divided by the number of pixels inside the left ventricle. Results were added together no matter if they shared the same number of frames (this explains why SP-HR and SinMod shows curves with increasing and decreasing behavior).

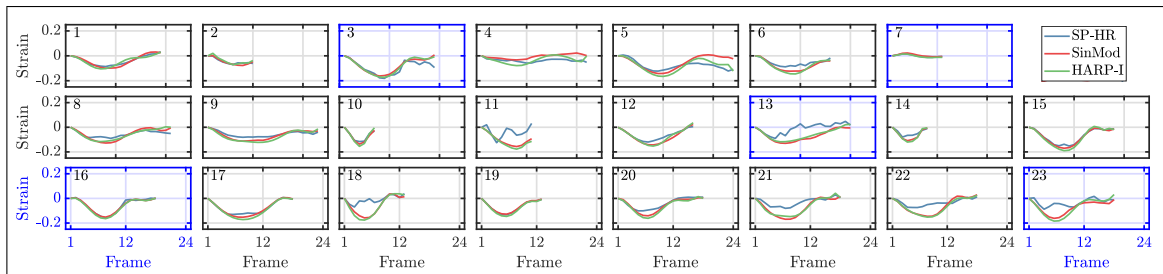


Figure 3.10. Circumferential strain curves estimated with SP-HR, SinMod, and HARP-I for in-vivo data (highly unlikely strain values bigger than 0.5 were not considered for the estimation of the curve with SP-HR and SinMod methods, not so with HARP-I). The number on each plot is a label to make it easier to refer to the result of each volunteer. Results remarked with blue boxes are the same as those presented in Figure 3.8. The volunteers 7 and 13 presented abnormal strain patterns as they presented cardiomyopathies. The first case showed a hypokinetic LV and the second hypertrophic cardiomyopathy.

### 3.6. Discussion

HARP-I was based on the same principles of the original HARP method but using a different approach to recover the tissue motion. Firstly, we obtained the harmonic phases

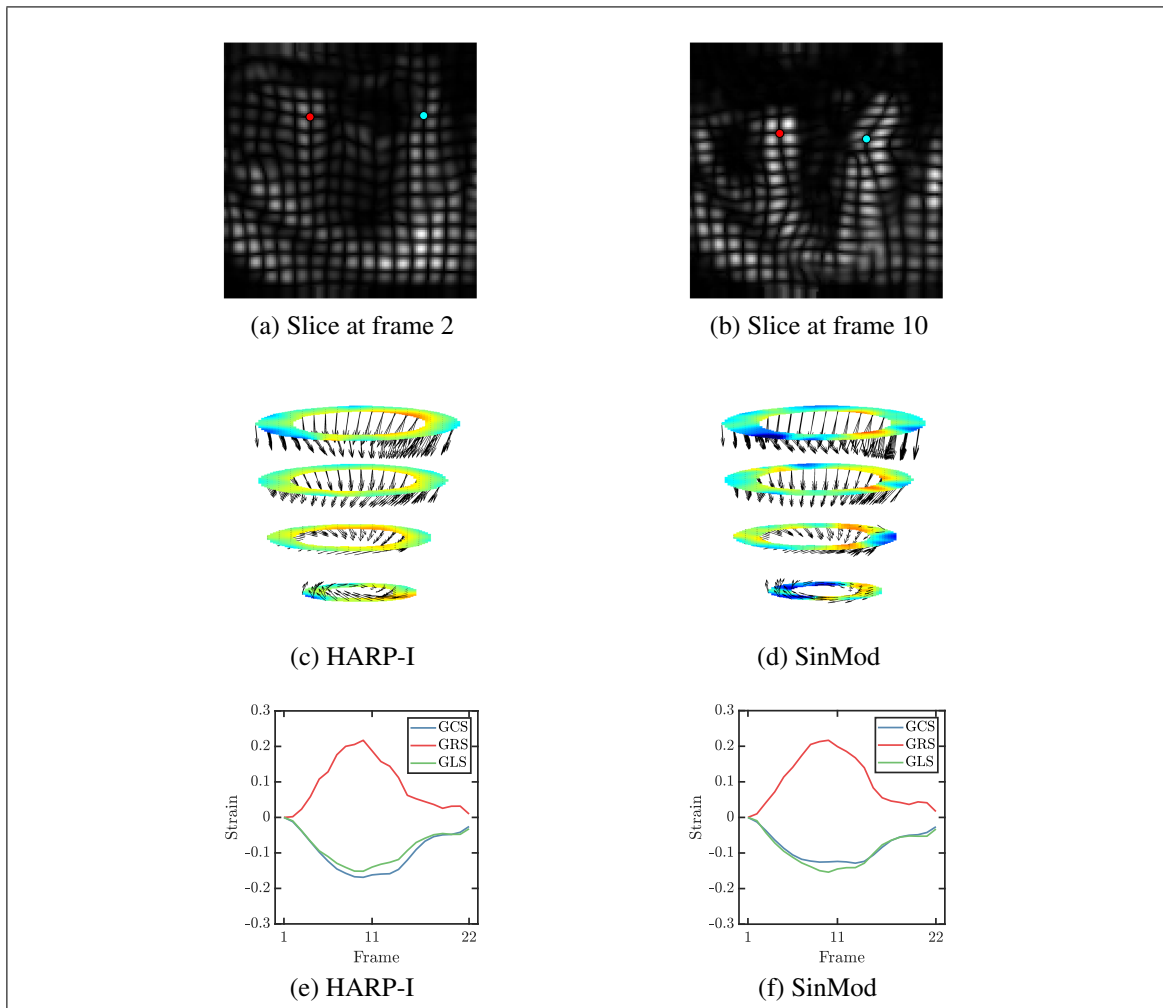


Figure 3.11. Motion estimated from a 3D CSPAMM image of a healthy volunteer using HARP-I and SinMod. The figure shows a slice of the 3D volume at (a) frame 2 and (b) 10 of the cardiac cycle (the first frame was not used because of the lack of contrast between the cardiac walls and the blood pool) and the circumferential strain and displacement field (arrows) at frame 10 estimated using (c) HARP-I and (d) SinMod. The red and blue dot denotes the position of two points manually tracked. Figures (e) and (f) shows the global strains of the circumferential, radial, and longitudinal components (GCS, GRS, and GLS, respectively) obtained with HARP-I and SinMod. The strain maps were plotted in the range  $[-0.5, 0.2]$ .

by bandpass filtering the tagged MR images. Second, we corrected the phases from wrapping artifacts, and then, we correct phase inconsistencies using distance matrices on the virtual coordinate system. Finally, similarly to HARP which treats the phase as a material

property, we used the phase to recover, via RBF interpolations, the motion field at any time on a reference frame. The previous methodology gave us a new technique with similar capabilities to SP-HR and SinMod, but with improved results under ideal as well as under noisy conditions.

In the absence of noise, the proposed method worked similar to that of SP-HR and SinMod, reaching all the techniques the worst performance with  $WL_7$  (see Figure 3.5). For this wavelength, the over-smoothed image obtained by the small bandwidth of the filter did not allow the accurate tracking of the tissue, and sharp details as the stiffer inclusion were lost. Exactly the opposite happened with smaller wavelengths (i.e., bigger filter bandwidths), where more detailed and accurate motion and strain maps were obtained (see Figure 3.5 and 3.7).

One of the most relevant biomarkers of the left-ventricular function is the circumferential strain (A. Young, 2006; Petitjean et al., 2005), which can be directly calculated from displacement fields. However, a good estimation of the tissue motion does not ensure a similar performance of the strain estimate. The last is summarized in Figure 3.6, where in presence of small motions and noise, SP-HR estimated fairly well the displacement field but misestimated the strain maps when compared with SinMod. Furthermore, the nRMSE in the circumferential and radial components obtained with SP-HR (under noise-free and noisy conditions) became more significant at the highest displacement level for  $WL_7$  (see Figures 3.5 and 3.6), which is attributable to high DC contamination.. HARP-I, on the other hand, gave the best estimations of both displacements and strain even at small motion levels, which is advantageous in the study of diseases where small displacements and strains are relevant (Auger et al., 2017).

HARP-I also demonstrated to be a reliable tool for the estimation strain from in-vivo data (see Figures 3.8 and 3.10), where strains similar to SP-HR and SinMod were obtained but with improved quality. The last assertion is also true for patient data with abnormal contraction patterns. For instance, in Figure 3.8, the end-systolic strain maps of the volunteers 7 (hypokinetic LV) and 13 (hypertrophic cardiomyopathy) obtained with HARP-I

were comparable to SP-HR and SinMod, and sharp details were conserved (see the anterolateral and inferolateral parts of volunteer 7, and the anteroseptum for volunteer 13). In the case of the hypokinetic LV, small details were kept even for small motion levels and deformations. However three methods failed at diastolic cardiac phases mainly due to DC contamination of the harmonic images.

Looking carefully into the strain curves, we could observe that they are according to the diagnoses and MRI findings detailed in Table 3.1. For subject 4, the Global Peak-Circumferential Strain (GPCS) was  $-7.0\%$ , which is consistent with the decreased LV systolic function, and the dyskinetic motion explains the unusual shape. The hypokinetic LV of subject 7 explains the GPCS of  $-1.4\%$  and its shape. The patients with Duchenne muscular dystrophy (subjects 10, 11, 12, and 14) presented a GPCS of  $-15.3 \pm 2.6\%$ , which is slightly reduced compared to reference values (Hor et al., 2009). Volunteer 13 exhibited the expected behavior in hypertrophic cardiomyopathy patients (Jeung et al., 2012). Additionally, we found a reduced GCPS of  $-10.5\%$  and  $-11.6\%$  in subjects 1 and 8 respectively, which had no known findings or diagnoses. Interestingly, for subject 2, the GCPS was  $-7.1\%$ , which is surprisingly low for a person with an EF of 50% (greater than 55% is considered normal). The last could be explained by some pathology developed with almost preserved EF unknown by the authors. Excluding the data previously mentioned, the GCPS on healthy subjects was  $-16.2 \pm 1.9\%$  and almost no differences were found between SP-HR, SinMod, and HARP-I.

Until this point, it is crucial to notice that the quality of the harmonic images highly depends on the bandpass filter. Several tagging modalities (as those used to acquire the volunteer data) do not have a sinusoidal intensity, and therefore, the frequency domain contains higher harmonics and a DC component. (Fischer et al., 1993). Thus, the size of the filter should be adjusted to ensure the isolation of just one harmonic and avoid the low-frequency component. At low magnetic fields, however, regardless of the accurate fitting of the filter, obtaining a harmonic image is not always possible because the DC component recovers rapidly with  $T1$ , which contaminates the harmonic peak early in the

cardiac cycle. The last was observed in almost all the in-vivo experiments, where the image corruption at diastolic cardiac phases, did not allow the appropriate estimation of motion with any of the three methods (see Figure 3.8). These issues can be surpassed by using acquisition and reconstruction techniques such as CSPAMM (Fischer et al., 1993) and MICSr (NessAiver & Prince, 2003) with the cost of increased scan time.

An advantageous feature of HARP-I is that, although RBF interpolations removed rapid spatial variations from displacements and strain maps, there was no deterioration in the estimation of local characteristics of the tissue. In fact, under noise-free conditions and without DC component (as in CSPAMM or MICSr images), the shape and position of the stiffer inclusions of different sizes were correctly estimated in almost all the cases, failing just with the smallest (see Figure S2 in Supporting Information). Furthermore, in Figure 3.7 HARP-I correctly estimated the position, shape, and strain of the stiffer inclusion under noisy and DC-contaminated conditions, which could be determinant for the detection of infarcted tissue and other diseases.

Another feature of HARP-I which is shared with SP-HR and SinMod, is that none of them need a segmentation to estimate tissue motion, and similar motion-guided semi-automatic segmentation techniques as such introduced in (Khalifa et al., 2005) and (Miller et al., 2013) can also be implemented. However, the motion estimation with HARP-I depends on the availability of a unwrapped harmonic phase of high quality on the tissue of interest, which depends on the unwrapping method used. In this work, a Quality-guided Path Following algorithm was used, which performed well in all the cases as the path was constrained inside the geometry of the tissue, i.e., a segmentation was available. To avoid the segmentation without losing quality in the estimation of motion, unwrapping algorithms based on phase predictions with region growing (Auger, Cai, Sun, & Epstein, 2018) and graphcuts (Bioucas-Dias & Valadão, 2007; Venkatesh, Gupta, Lloyd, Dell'Italia, & Denney, 2010) could be used.

When working with the 3D CSPAMM data, HARP-I worked better than SinMod in terms of strain smoothness and displacement field estimation. In fact, HARP-I was able

to give accurate estimation displacement field in the longitudinal direction (the reference values were obtained manually from the images), whereas SinMod presented overestimated values. Additionally, as HARP-I estimates the motion between two frames directly (without intermediate estimations), less tracking artifacts were observed.

The efficiency of the proposed method, in terms of computation time, was also measured and compared against SP-HR and SinMod. In general, on a machine with an Intel Core i7-8700 CPU with 12 physical cores of 3.20 GHz and 32 Gb of memory, HARP-I took around 6.0 seconds to process each data (phase-unwrapping and interpolation), while SP-HR took 1.4 seconds and SinMod 3.2. Additionally, for the 3D experiment, the execution times were 184 seconds with HARP-I (phase-unwrapping and interpolation) and 155 with SinMod (frame-by-frame estimation and Lagrangian tracking). In the last case, to avoid memory issues with HARP-I, we implemented a disjoint RBF interpolation scheme, in which the interpolator was defined on a equispaced downsampled set of points and evaluated incrementally in the reference frame. Overall, the three techniques shared similar processing times with the same order of magnitude, and no delays were introduced by HARP-I.

In this study, HARP-I was used to estimate the Lagrangian strain at a reference frame. However, with a small modification of the interpolator given in Eq. 3.7 Eulerian strain could also be obtained. If the interpolator is defined once at the first cardiac phase and evaluated at  $\mathbf{X}_V(\mathbf{x}, t_k)$ , the Eulerian displacement is obtained at frame  $k$ , which allows the estimation of the Eulerian strain tensor. This approach would be faster because it does not need the definition of multiple interpolators.

Additionally, we developed a new method to fix the temporal phase inconsistencies, which uses the same distance matrices needed for the RBF interpolation. With this method, we were able to correct all the phase jumps between frames without additional constraints on the tag-spacings and temporal resolution, making it robust to any combination of imaging parameters. On all the tested data, either in-silico and in-vivo, the correction worked in 100% of the cases. Therefore, even at the low temporal resolutions usually found in

clinical and scientific setups (18 to 20 frames per cardiac cycle), HARP-I could work with even fewer frames without any bound on the total number. Although techniques like HARP Tracking Refinement Using Seeded Region Growing (X. Liu et al., 2007) and SP-HR (X. Liu & Prince, 2010) can also deal with large tissue motion between frames, in this work we found that SP-HR and SinMod failed in many cases due to high DC contamination.

It must be clear that by solving Eq. 3.11, we are ensuring that the tissue motion estimated using HARP-I is free of non-physiological jumps in time. Therefore, the temporal consistency imposed by HARP-I differs from other methodologies proposed previously for MRI and other imaging modalities. Different to computationally expensive registration algorithms (Reinhardt et al., 2008; You, Evangelou, Zun, Andescavage, & Limperopoulos, 2016; Liao et al., 2016), biomechanically constrained inverse problems (Sundar, Davatzikos, & Biros, 2009), and physiological motion models (McClelland, Hawkes, Schaeffter, & King, 2013), HARP-I decouples the temporal consistency problem from the motion estimation step. Furthermore, as these two steps are decoupled (i.e., nothing is said about the displacement field), there is no need for adding spatiotemporal constraints to the motion estimation problem, avoiding adding limitations between the tag spacing and the number of frames of tagged images (Spottiswoode et al., 2007; Venkatesh et al., 2010). Additionally, the proposed technique is self-contained (in the sense that does not need external information) and can be applied to any data without previous knowledge of cardiac motion behavior, which is the case of statistically-based methods (Chandrashekhara et al., 2003). In other words, HARP-I does not need additional calculations to correct temporal inconsistencies rather than comparing two matrices (see Eq. 3.11).

Finally, when compared to further improvements of HARP, HARP-I addressed the same issues but with enhanced results. With HARP-I, smoothed results were obtained without losing quality in the estimation and keeping small and sharp details. The amount of artifacts in the displacement field were highly reduced and they did not propagate to other cardiac phases. Although the used quality-guided unwrapping algorithm does

not handle well corrupted phases, HARP-I demonstrated to have low sensitivity to DC contamination, maintaining its robustness even for highly deteriorated harmonic phases. The proposed RBF interpolation approach also dealt with mistracked boundary points and through-plane motion (which makes the tissue disappear) by interpolating or extrapolating the positions depending on the case. In the case of artifacts in the motion pattern, these were corrected using the polynomial fitting proposed in (Spottiswoode et al., 2007), which did not work with either SP-HR and SinMod.

### **3.7. Conclusion**

We developed a new method for motion estimation from tagged MR images based on the same physical principle as HARP and SP-HR but with a different processing pipeline. HARP-I allows the estimation of motion in any direction with better results than SP-HR and SinMod techniques under highly demanding conditions as DC contamination, tag-lines fading, and image quality. HARP-I also showed to be more robust on estimating motion patterns with high temporal consistency, which was appreciated as artifacts-free strain patterns at almost any cardiac phase. Fast and robust extraction of motion gives HARP-I a potential in routine analysis of clinical exams to facilitate patient stratification. Secondly, the outcome of HARP-I could be used as high-quality observers while assimilating data into complex biomechanical models, e.g., to contribute to optimal therapeutical action (Imperiale, Chabiniok, Moireau, & Chapelle, 2011; Chabiniok et al., 2012; Bertoglio, Moireau, & Gerbeau, 2012; Hadjicharalambous et al., 2017).

### **3.8. Acknowledgements**

The authors thankfully acknowledge the financial support of the ANID Ph. D. Scholarship 21170592 as well as the following projects and institutions: ANID-FONDECYT 1181057, ANID-FONDECYT Postdoctorado 3170737, ANID-FONDECYT de Iniciación en Investigación 11200481, ANID-Millennium Science Initiative Program-NCN17\_129;

the Ministry of Health of the Czech Republic (project No. NV19-08-00071), and Inria-UTSW Medical Center Dallas Associated Team TOFMOD.

## 4. A NOVEL SEQUENCE FOR TAGGING MRI

### 4.1. Title and authors

An Off-Resonance Insensitive Orthogonal CSPAMM sequence (ORI-O-CSPAMM) for the acquisition of CSPAMM and MICSr grids in half scan time

*Hernán Mella*<sup>1,2,4</sup>, *Hui Wang*<sup>5,6</sup>, *Cristian Montalba*<sup>2,4</sup>, and *Sergio Uribe*<sup>2,3,4</sup>

<sup>1</sup> Department of Electrical Engineering, Pontificia Universidad Católica de Chile, Santiago, Chile.

<sup>2</sup> Biomedical Imaging Center, Pontificia Universidad Católica de Chile, Santiago, Chile.

<sup>3</sup> Department of Radiology, School of Medicine, Pontificia Universidad Católica de Chile, Santiago, Chile.

<sup>4</sup> ANID - Millennium Science Initiative Program - Millennium Nucleus in Cardiovascular Magnetic Resonance, Santiago, Región Metropolitana, Chile.

<sup>5</sup> Philips, Cincinnati, Ohio, USA.

<sup>6</sup> Department of Radiology, Cincinnati Children's Hospital Medical Center, Cincinnati, Ohio, USA.

Article published in the Magnetic Resonance in Medicine journal (impact factor of 4.668).

### 4.2. Introduction

Tagged Magnetic Resonance Imaging has been used extensively to study the function of the heart as well as other organs. After its introduction, several techniques have been proposed to improve the original idea, leading to new sequences with improved image quality (Axel et al., 2005; E.-S. H. Ibrahim, 2011). The first and still widely used tagging technique was Spatial Modulation of Magnetization (SPAMM) (Axel & Dougherty, 1989a), which employed a spatial encoding gradient and two non-selective RF pulses to

rapidly modulate the magnetization. One of the most notable improvements was the development of the Complementary SPAMM (CSPAMM) sequence (Fischer et al., 1993), which was introduced to improve the tagging contrast in later phases of the cardiac cycle and remove the unwanted DC signal of SPAMM images, leading to a zero mean sinusoid suitable for motion estimation techniques such as Harmonic Phase-based analysis (HARP) (Osman et al., 1999, 2000; Tecelão et al., 2006; X. Liu et al., 2007; X. Liu & Prince, 2010; Mella et al., 2021), Sine-Wave Modeling (SinMod) (Arts et al., 2010; H. Wang & Amini, 2011, 2013), and Gabor filter banks (Qian et al., 2006; T. Chen & Axel, 2006). A Magnitude Image CSPAMM Reconstruction (MICSr) (NessAiver & Prince, 2003) method was introduced later as an alternative reconstruction procedure to combine SPAMM acquisitions using only magnitude images. The resulting signal shared similar characteristics with CSPAMM (zero mean sinusoid) but with improved tag persistence and enhanced contrast during most of the acquisition window. Moreover, MICSr cancelled out any spurious phase gained during the readout from complex SPAMM data. However, due to the doubled acquisition time, the use of both CSPAMM and MICSr remain restricted for clinical applications, and both CSPAMM and MICSr images are prone to off-resonance effects during the tagging preparation, which can impact the motion estimation in presence of tissue with fat content (Fahmy et al., 2009; Reyhan et al., 2014).

To overcome the acquisition time issue, Wang et al. (H. Wang et al., 2011) introduced the Orthogonal CSPAMM sequence (O-CSPAMM), which allowed to obtain a CSPAMM image with orthogonal taglines using only two acquisitions instead of four. By rotating in  $90^\circ$  the tagging gradient in the complementary SPAMM acquisition, O-CSPAMM removed the DC component while generating an orthogonal grid after complex subtraction (i.e., O-CSPAMM is the sum of two orthogonal zero-mean sinusoids). While this methodology allowed the acquisition of data that can be optimally used for motion estimation (H. Wang et al., 2012) (20), O-CSPAMM is not compatible with MICSr reconstructions and is prone to off-resonance effects. To fix the off-resonance sensitivity issue, Fahmy et al. (Fahmy et al., 2009) proposed a new method to cancel the off-resonance effects of the fat in CSPAMM acquisitions by inverting the tagging gradient of the second SPAMM

image and adjusting its duration. However, this approach was limited to one chemical specie (fat) and was inapplicable at field strengths bigger than 1.5T, especially for closely spaced tag lines. Reyhan et al. (Reyhan et al., 2014) introduced an Off-Resonance Insensitive CSPAMM (ORI-CSPAMM) sequence to compensate for all forms of off-resonance, in which the tagging gradient was split into two parts separated by a  $180^\circ$  refocusing hard pulse, removing the off-resonance effects of any chemical specie at the cost of some intensity changes. Nonetheless, the last two approaches share the same time restrictions than conventional CSPAMM.

In this work, we propose an Off-Resonance Insensitive O-CSPAMM (ORI-O-CSPAMM) sequence, which takes the best of O-CSPAMM and ORI-CSPAMM. The proposed sequence allows the obtention of orthogonally tagged CSPAMM images free of off-resonance artifacts and suitable for MICSr reconstructions in half of the acquisition time compared to CSPAMM and ORI-CSPAMM.

### 4.3. Methods

#### 4.3.1. Sequence development

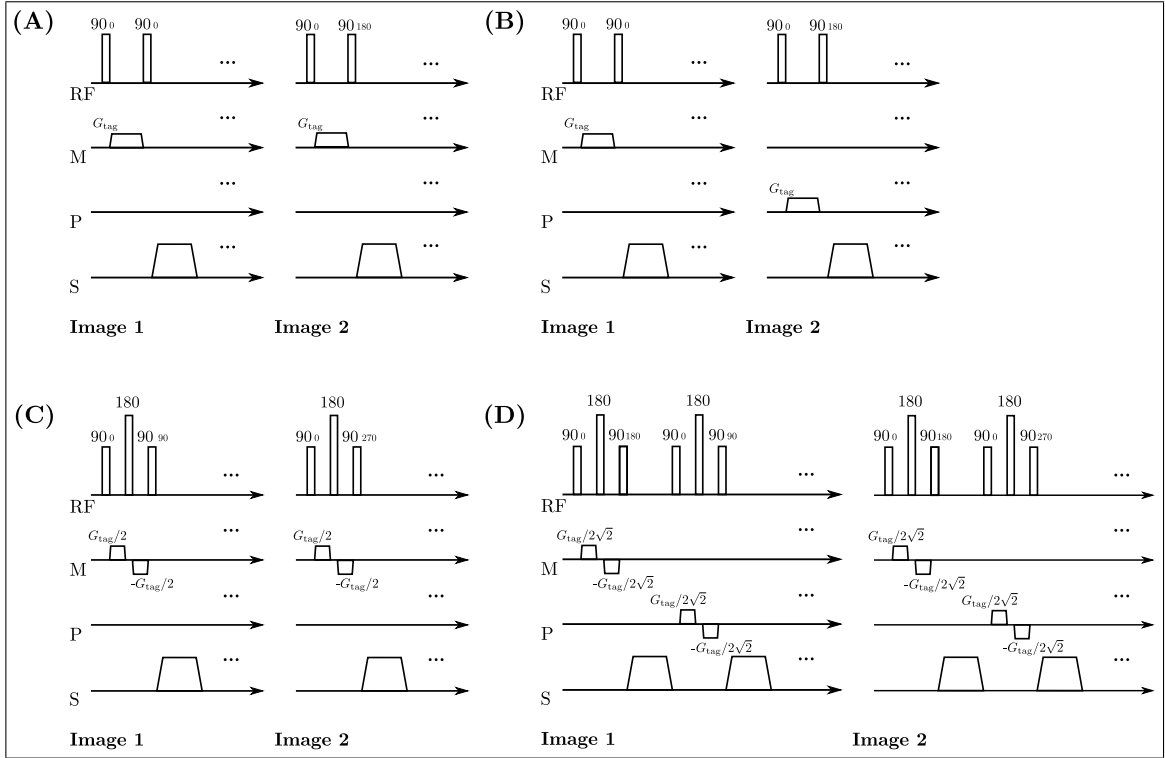


Figure 4.1. (A) CSPAMM, (B) O-CSPAMM, (C) ORI-CSPAMM, and (D) ORI-O-CSPAMM tagging preparations. In all the figures, M, P, and S denote the measurement, phase, and slice axes. In the ORI-CSPAMM sequence, the spurious phase gained during the tagging preparation is re-wound by splitting the tagging gradient into two parts separated by a  $180^\circ$  refocusing hard pulse.

Figure 4.1 shows the pulse sequence diagram for the CSPAMM, O-CSPAMM, ORI-CSPAMM, and the proposed ORI-O-CSPAMM sequences. The phases of the RF pulses in Figure 1 determine if the resulting images will be cosine- or sine-modulated (a  $0^\circ$  RF phase denotes a rotation around the  $+X$  axis and a  $90^\circ$  RF phase a rotation around the  $+Y$ ). As a general rule, we can consider that the tagline modulation will vary with the  $\cos(\phi(X) - \theta)$ , where  $\phi(X)$  is the encoded position and  $\theta$  the phase of the last RF pulse of

the tagging preparation (e.g., if the phase of the last RF pulse is  $0^\circ$  or  $90^\circ$ , the taglines will be cosine- or sine-modulated, respectively). For CSPAMM, as the phases of the second RF pulses are  $0^\circ$  and  $180^\circ$  (see Figure 1A), the transversal magnetization of each image after the readout is cosine-modulated and is given by:

$$M_{\text{CSPAMM},1} = \{f_1(t, T1, M_0, \alpha) - f_2(t, T1, M_0, \alpha) \cos(k_e X + \phi_{\text{tag}})\} e^{i\phi_{\text{RO}}} \sin(\alpha), \quad (4.1a)$$

$$M_{\text{CSPAMM},2} = \{f_1(t, T1, M_0, \alpha) + f_2(t, T1, M_0, \alpha) \cos(k_e X + \phi_{\text{tag}})\} e^{i\phi_{\text{RO}}} \sin(\alpha), \quad (4.1b)$$

where  $i = \sqrt{-1}$  denotes the complex unit,  $k_e$  the encoding frequency produced by the tagging gradient,  $X$  the tissue position at a reference frame (usually at end-diastole in cardiac imaging), and  $\phi_{\text{tag}}$  and  $\phi_{\text{RO}}$  denote spurious phases induced due to off-resonance effects during the application of the tagging gradient and the read-out, respectively. It is important to mention that  $\phi_{\text{RO}}$  was assumed equal between acquisitions for the sake of simplicity, although it can vary between images due to phenomena such as eddy currents. In Eq. 4.1,  $f_1$  and  $f_2$  are increasing and decreasing functions (respectively) that depend on the time  $t_n$  (with  $n = 0, \dots, N_{fr} - 1$  the current frame number and  $N_{fr}$  the total number of frames), the relaxation time  $T1$ , the magnetization in the thermal equilibrium  $M_0$ , and the flip angle  $\alpha$  of the imaging RF pulse (in following equations, the dependency on  $t, T1, M_0$ , and  $\alpha$  will be dropped to simplify the expressions). Both  $f_1$  and  $f_2$  take into consideration that the tissue tends to the thermal equilibrium and the taglines fade, respectively, and take the following form (Fischer et al., 1993; NessAiver & Prince, 2003):

$$f_1 = M_0 \sin(\alpha) \cos^n(\alpha) (1 - e^{-t_n/T1}) \quad (4.2a)$$

$$f_2 = M_0 \sin(\alpha) \cos^n(\alpha) e^{-t_n/T1} \quad (4.2b)$$

In Equation 4.2, the term  $\cos^n(\alpha)$  represent the residual part of the longitudinal magnetization after a train of  $n + 1$  imaging RF pulses of constant flip angle  $\alpha$ . Then, the complex

difference and MICSR images are obtained by:

$$\begin{aligned} M_{\text{CSPAMM}} &= M_{\text{CSPAMM},2} - M_{\text{CSPAMM},1} \\ &= 2f_2 \sin(\alpha) e^{i\phi_{\text{RO}}} \cos(k_e X + \phi_{\text{tag}}) \end{aligned} \quad (4.3a)$$

$$\begin{aligned} M_{\text{MICSR}} &= |M_{\text{CSPAMM},2}|^2 - |M_{\text{CSPAMM},1}|^2 \\ &= 4f_1 f_2 \sin^2(\alpha) \cos(k_e X + \phi_{\text{tag}}) \end{aligned} \quad (4.3b)$$

In the previous expressions, the complex difference taken in Eq. 4.3a does not remove the spurious phase gained during the readout, while the MICSR does.

The magnetization expression for each image in a O-CSPAMM is also cosine-modulated because they use identical RF pulses to CSPAMM. Therefore, the magnetization expressions for O-CSPAMM images are:

$$M_{\text{O-CSPAMM},1} = \{f_1 - f_2 \cos(k_e X + \phi_{\text{tag}})\} e^{i\phi_{\text{RO}}} \sin(\alpha), \quad (4.4a)$$

$$M_{\text{O-CSPAMM},2} = \{f_1 + f_2 \cos(k_e Y + \phi_{\text{tag}})\} e^{i\phi_{\text{RO}}} \sin(\alpha), \quad (4.4b)$$

$$M_{\text{O-CSPAMM}} = f_2 \sin(\alpha) e^{i\phi_{\text{RO}}} \{\cos(k_e X + \phi_{\text{tag}}) + \cos(k_e Y + \phi_{\text{tag}})\} \quad (4.4c)$$

$$\begin{aligned} M_{\text{O-MICSR}} &= 2f_1 f_2 \sin^2(\alpha) \{\cos(k_e X + \phi_{\text{tag}}) + \cos(k_e Y + \phi_{\text{tag}})\} \\ &\quad + f_2^2 \sin^2(\alpha) \{\cos^2(k_e X + \phi_{\text{tag}}) + \cos^2(k_e Y + \phi_{\text{tag}})\}. \end{aligned} \quad (4.4d)$$

In Eq. 4.4c, the image obtained by complex difference is a grid consisting of the sum of two sinusoids, while in Eq. 4.4d, the MICSR image contains unwanted higher order terms.

In ORI-CSPAMM, the tagging gradient during each image's preparation is split into two parts with opposite polarities and separated by a refocusing hard RF pulse (see Fig. 4.1A). The last makes that the spurious phase  $\phi_{\text{tag}}$  gained during the first gradient application be completely rewound after applying the second gradient. Additionally, in this sequence, the phases of the last RF pulses are  $90^\circ$  and  $270^\circ$ , which means that the taglines are sine-modulated. Thus, the longitudinal magnetization after the third pulse of each

SPAMM acquisition is:

$$M_{\text{ORI-CSPAMM},1} = \{f_1 - f_2 \sin(k_e X)\} e^{i\phi_{\text{RO}}} \sin(\alpha), \quad (4.5a)$$

$$M_{\text{ORI-CSPAMM},2} = \{f_1 + f_2 \sin(k_e X)\} e^{i\phi_{\text{RO}}} \sin(\alpha). \quad (4.5b)$$

In this investigation, we could not reproduce the results of (Reyhan et al., 2014), as the spurious phase gained during the read-out was not transformed into a cosine modulation by the subtraction operation (as will be demonstrated later). Therefore, the complex difference and MICSr images obtained with ORI-CSPAMM are:

$$M_{\text{ORI-CSPAMM}} = 2f_2 \sin(\alpha) e^{i\phi_{\text{RO}}} \sin(k_e X), \quad (4.6a)$$

$$M_{\text{ORI-MICSr}} = 4f_1 f_2 \sin^2(\alpha) \sin(k_e X), \quad (4.6b)$$

which have taglines in one direction without off-resonance effects.

With both O-CSPAMM and ORI-CSPAMM, a tagging grid without DC frequencies can be obtained by acquiring 2 and 4 images, respectively. In both cases, the magnetization is shifted by  $e^{i\phi_{\text{RO}}}$ , which induces a distortion in the complex image that can be removed by taking its magnitude or using MICSr. However, the first procedure generates low (DC component) and high harmonic frequencies, and the second is restricted only to ORI-CSPAMM because of the presence of higher order terms (see Eq. 4.4d).

To overcome these issues, in ORI-O-CSPAMM we applied the ORI preparation used in ORI-CSPAMM (see Fig. 4.1C) twice in two orthogonal directions to obtain a SPAMM grid within each image (see Fig. 4.1D). The final modulation of the grid depends on the  $180^\circ$  and  $90^\circ \pm 180^\circ$  phases of the third and sixth RF pulses, respectively, which means that a grid modulated by the product of a cosine and sine functions will be obtained. Thus, the pair of images obtained with ORI-O-CSPAMM follows:

$$M_{\text{ORI-O-CSPAMM},1} = \{f_1 - f_2 \cos(k_e X) \sin(k_e Y)\} e^{i\phi_{\text{RO}}} \sin(\alpha), \quad (4.7a)$$

$$M_{\text{ORI-O-CSPAMM},2} = \{f_1 + f_2 \cos(k_e X) \sin(k_e Y)\} e^{i\phi_{\text{RO}}} \sin(\alpha), \quad (4.7b)$$

which can be combined taking the complex difference or using MICSR, obtaining:

$$M_{\text{ORI-CSPAMM}} = f_2 \sin(\alpha) e^{i\phi_{\text{RO}}} \cos(k_e X) \sin(k_e Y), \quad (4.8a)$$

$$M_{\text{ORI-MICSR}} = 2f_1 f_2 \sin^2(\alpha) \cos(k_e X) \sin(k_e Y). \quad (4.8b)$$

In Eq. 4.8a, still contains the phase shift  $e^{i\phi_{\text{RO}}}$  gained during the read-out, but this is fixed in Eq. 4.8b by the MICSR reconstruction. In both Eqs. 4.8a and 4.8b the obtained result is a grid.

The expressions given in 4.8 can be re-written using the identity  $\cos(x) \sin(y) = \{\sin(x + y) - \sin(x - y)\}/2$ , as:

$$M_{\text{ORI-CSPAMM}} = f_2 \sin(\alpha) e^{i\phi_{\text{RO}}} \{\sin(k_e X + k_e Y) - \sin(k_e X - k_e Y)\}, \quad (4.9a)$$

$$M_{\text{ORI-MICSR}} = 2f_1 f_2 \sin^2(\alpha) \{\sin(k_e X + k_e Y) - \sin(k_e X - k_e Y)\}. \quad (4.9b)$$

From Eq. 4.9, three important observations can be done: (a) ORI-O-CSPAMM gives images with the same contrast as CSPAMM and O-CSPAMM (considering that the absolute value of the sum of two sinusoids is bounded from above by 2. See Eqs. 4.4c, 4.4d, and 4.9). (b) Although the tagging gradients were applied towards the  $X$  and  $Y$  directions, the tagging patterns obtained with ORI-O-CSPAMM are rotated in  $45^\circ$  into the  $X + Y$  and  $X - Y$  directions (i.e., to obtain tag lines pointing towards the directions  $X$  and  $Y$ , the ORI-O-CSPAMM gradients must be applied in the directions  $X - Y$  and  $X + Y$ ). And (c), in ORI-O-CSPAMM smaller tagging gradient areas (by a factor of  $1/\sqrt{2}$ ), i.e. tagging encoding frequencies, are needed to generate the same tag period as in CSPAMM, ORI-CSPAMM, and O-CSPAMM (this is more evident if we consider the frequency of the wave  $\sin(\mathbf{k} \cdot \mathbf{X})$ , where  $\mathbf{k} = (k_e, k_e)$ ,  $\mathbf{X} = (X, Y)$ , and  $\|\mathbf{k}\| = \sqrt{2}k_e$ ).

It is important to notice that using the two complementary images scanned with CSPAMM and ORI-CSPAMM sequences, only 1D motion information can be obtained, while with the same data scanned with O-CSPAMM and ORI-O-CSPAMM, 2D motion information can be recovered.

Table 4.1. Imaging parameters used during the acquisition of the in-silico and in-vivo data. All the volunteers shared the same imaging parameters, only differing in the number of cardiac phases.

	Phantom	Volunteers
ETL (TFE factor)	5	5
Acq. Matrix	160 × 120	160 × 75
Recon. Matrix	160 × 160	160 × 160
FOV (mm <sup>2</sup> )	175 × 175	260 × 260
Tag period (mm)	17.5	17.5
Slice thickness (mm)	8	8
FA	10°	10°
Cardiac phases	21	23, 24, 31
TR/TE	7.0/3.4	5.3/2.6
Trigger delay (ms)	31	26

Abbreviations: ETL, echo-train-length; FA, flip angle.

#### 4.3.2. Phantom and in-vivo data acquisition

A phantom consisting of a bottle filled with the same amount of water and vegetable oil was scanned. For the in-vivo acquisition, three healthy male volunteers with age 27, 28, and 35 years old, weight 60, 74, and 68 kg, and heart rate 51, 68, and 71 beats/min were studied. Each volunteer provided a written informed consent approved by the local institutional review board. ECG triggered images were acquired at end-expiration in a breath-hold condition. Mid-level short-axis views of the heart were obtained using a four-element cardiac coil. The phantom and in-vivo protocols consisted of the acquisition of bSSFP, CSPAMM, ORI-CSPAMM, O-CSPAMM and ORI-O-CSPAMM images. For the ORI-O-CSPAMM scans, tagging gradients  $1/\sqrt{2}$  times weaker were applied in the directions  $X + Y$  and  $X - Y$  to achieve the user-defined tag-period in the directions  $X$  and  $Y$ .

All the sequences for both phantom and in-vivo acquisitions were acquired on a 1.5T Achieva system (Philips, Best, The Netherlands) using a multi-shot Turbo-Field-Echo (TFE) with imaging parameters listed in the Table 4.1, setting the shortest trigger delay time and the maximum number of cardiac phases.

### 4.3.3. Image analysis

To compare the signal characteristics of ORI-O-CSPAMM, we normalized the signal of each complementary image before the complex difference and MICSr reconstructions and compared the normalized mean signals of ORI-O-CSPAMM and ORI-CSPAMM in both fat and water regions of the phantom. The images were normalized by the  $M_0$  of the fat, which has the biggest magnitude at the first cardiac phase (see Fig. 4.2).  $M_0$  was estimated by calculating the mean signal inside a ROI in the fat region of one of the complementary acquisitions of the ORI-CSPAMM sequence (see Fig. 4.1B and Eq. 4.1), as proposed by NessAiver et al. (NessAiver & Prince, 2003).

To obtain the normalized mean signal, two rectangular ROIs with the same dimensions were placed in the fat and water regions. Then, the maximum signal of the magnitude of the complex difference images inside each ROI was found and used to define a threshold. This procedure was applied to the first cardiac phase, masking the pixels where the signal was greater than 0.65 times the maximum value obtained inside each rectangular ROI, obtaining the fat and water masks shown in Fig. 4.2. Finally, the normalized mean signal was calculated with the pixels inside the fat and water masks.

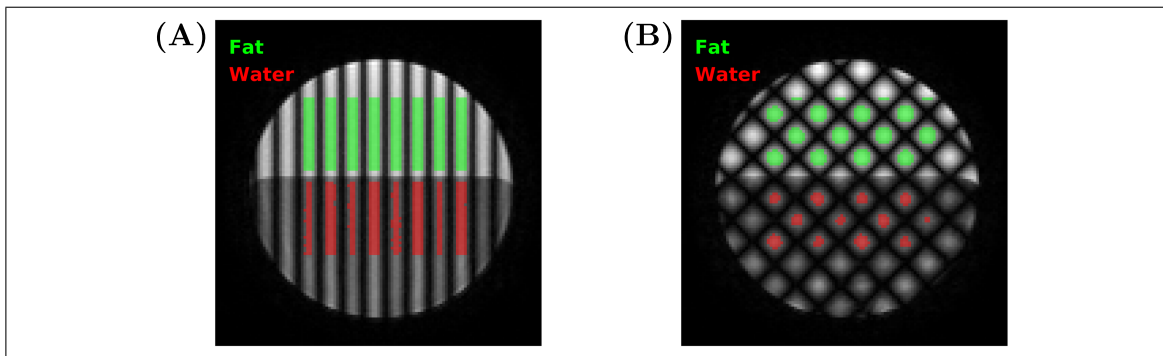


Figure 4.2. Fat and water masks used for the estimation of the Normalized Mean Signal in (A) ORI-CSPAMM and (B) ORI-O-CSPAMM images.

The off-resonance insensitive benefits and the capacity to obtain MICSr images of the proposed ORI-O-CSPAMM sequence are shown by comparing the acquired images qualitatively to O-CSPAMM.

## 4.4. Results

### 4.4.1. Phantom acquisition

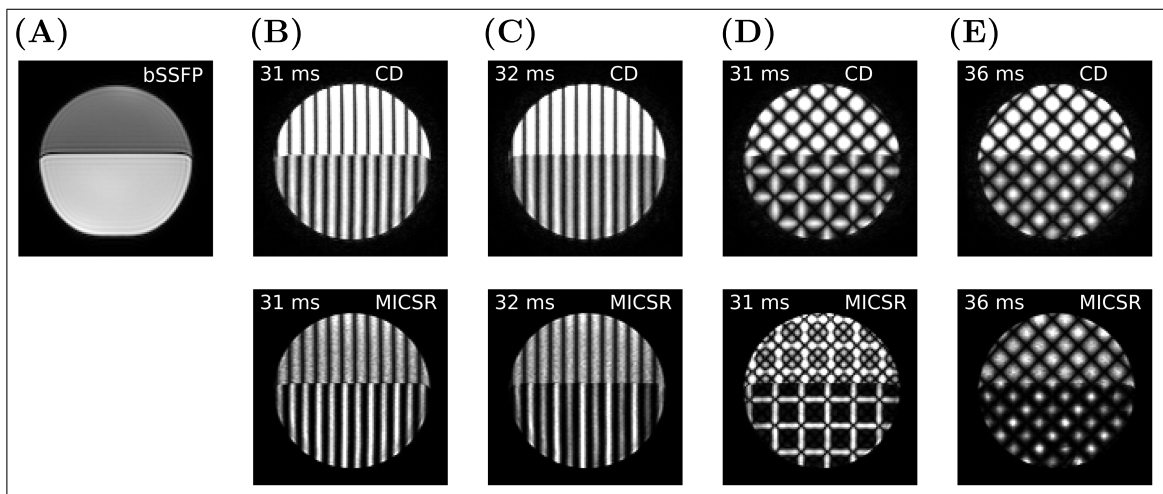


Figure 4.3. Water and fat phantom images obtained using complex difference (CD. Upper row) and MICSr (bottom row). The images were acquired using (A) bSSFP, (B) CSPAMM, (C) ORI-CSPAMM, (D) O-CSPAMM, and (E) ORI-O-CSPAMM sequences. The trigger delay of each image is shown in the figures and varies due to the different duration of the preparation pulses. The images acquired without ORI preparation showed a shift in the tagging pattern at the water-fat interface. The MICSr image obtained from O-CSPAMM lost the grid pattern as predicted in Eq. 4.4d.

Figure 3 shows the first frame of the complex difference and MICSr images obtained from CSPAMM, ORI-CSPAMM, O-CSPAMM, and ORI-O-CSPAMM data. The differences in the trigger delay time between acquisitions is due to the different duration of the preparation pulses. The resulting images show that those acquired without using the ORI preparation (see Figures 4.3B and 4.3D), presented a shift at the fat-water interface. Images obtained using complex difference showed a higher signal than MICSr, which

is the expected behavior. Tagging patterns were correctly obtained with MICSR using CSPAMM, ORI-CSPAMM, and ORI-O-CSPAMM scans, while using O-CSPAMM, distorted grids were obtained due to the second-order sinusoidal term in 4.4d. The complex difference and MICSR images obtained with O-CSPAMM showed distorted grids in the water region produced by high-frequency spectral peaks.

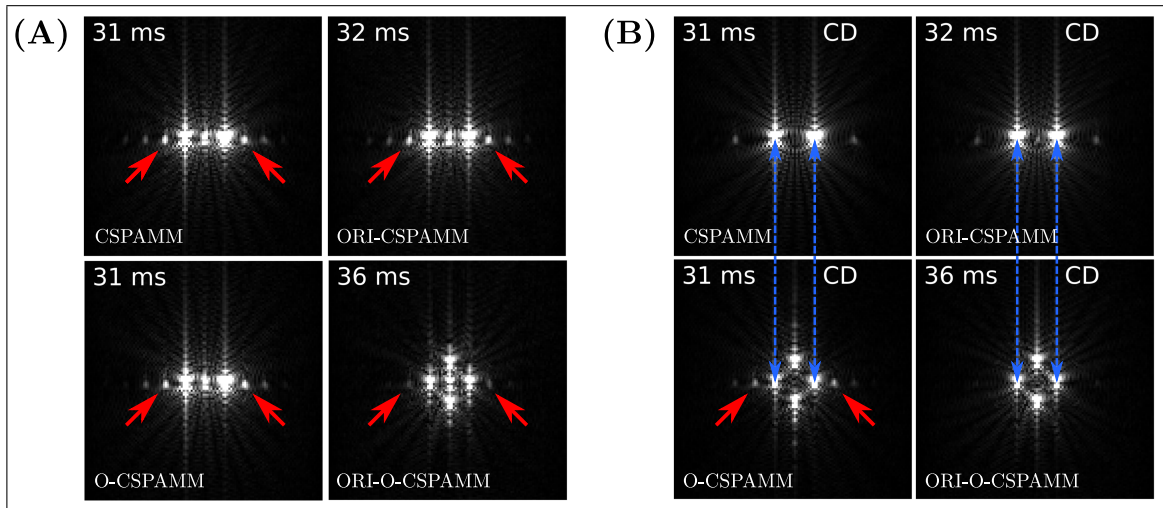


Figure 4.4. k-spaces of the (A) first complementary image acquired by each sequence and (B) the complex difference (CD) reconstructions. High-frequency spectral peaks are present on all the images in (A) although are less visible with ORI-O-CSPAMM (see red arrows). In the complex difference images, the most energetic high-frequency peaks are completely removed with all the sequences but not with O-CSPAMM (see red arrows in (B)), which generate distortions in the water part of the phantom image (see Fig. 4.3). Although  $45^\circ$  rotated and weaker gradients were applied using ORI-O-CSPAMM, the same encoding frequency (tag period) was achieved compared to the other sequences (see blue vertical arrows in (B)).

Fig. 4.4 shows the k-spaces of the first complementary image and the complex difference reconstructions (see Fig. 4.3) obtained in the phantom with the four acquisition sequences. High-frequency spectral peaks are present in all the k-spaces of the first complementary images, but their intensity is reduced with ORI-O-CSPAMM (see Fig. 4.4A). The additional spectral peaks are generated by the reduced k-space in the phase direction (see Table 4.1). In the case of O-CSPAMM, the most energetic high-frequency peaks

were not removed after taking the complex difference (see Fig. 4.4B), which curiously only distorted the water part of the phantom image (see Fig. 4.3D). For the acquisition of the ORI-O-CSPAMM data, the tagging gradients were rotated in  $45^\circ$  into the direction  $X + Y$  and  $X - Y$  and made weaker by a factor of  $1/\sqrt{2}$ . However, the same period and direction of the tagging lines was observed as stated by the Eq. 4.9.

Fig. 4.5 shows the normalized mean signal for the fat and water regions. The signal curves obtained from complex-difference showed the expected behavior in both fat and water, with the highest signal in the first cardiac phase and decaying through the acquired temporal window. The signals measured from MICS images also behaved as expected although there were evident differences between fat and water curves. In the fat (see Fig. 4.5A), the MICS signals increased at the very beginning of the acquisition window, reaching higher values than those obtained by complex difference, and decaying until the end, which follows the characteristic signal behavior of MICS images. In the water (see Fig. 4.5B), however, the decaying part of the MICS signals are not appreciable in the acquisition window used due to the long  $T_1$ . Overall, the normalized mean signals obtained from ORI-O-CSPAMM scans were almost equal in complex difference images and slightly higher in MICS images.

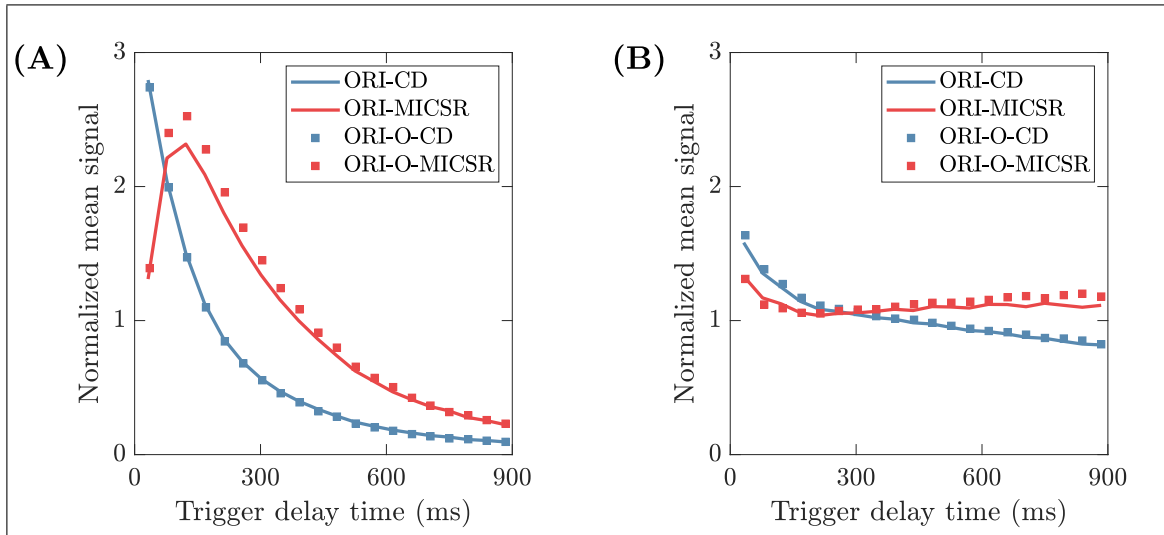


Figure 4.5. Normalized mean signal in the fat (A) and water (B) obtained from images reconstructed using complex difference (CD) and MICSR, from data acquired using ORI-CSPAMM and ORI-O-CSPAMM sequences. The normalized signal from an ORI-CSPAMM acquisition is shown using a blue and red continuous line respectively, while curves obtained from an ORI-O-CSPAMM acquisition are displayed using blue and red square markers.

#### 4.4.2. In-vivo acquisition

Fig. 4.6 shows the first cardiac phase of complex difference and MICSR images obtained with O-CSPAMM and ORI-O-CSPAMM for the three volunteers. MICSR images obtained from O-CSPAMM acquisitions produced distorted grid as predicted by the Eq. 4.4d, which was not the case of ORI-O-CSPAMM acquisitions. The signal of complex difference images was higher than MICSR images for the three volunteers, which was also observed in the phantom (see Figures 4.3 and 4.5) and it is the expected behavior. The three volunteers presented epicardial and subcutaneous fat (see bSSFP images in Fig. 4.6), which distorted the tagging grids in O-CSPAMM (see red arrows in Fig. 4.6) but not in ORI-O-CSPAMM images.

Fig. 4.7 shows the same results described for the Fig. 4.6 but for an end-systolic cardiac phase. The signal of MICSR obtained from ORI-O-CSPAMM was higher than

complex difference images in all the cases, which was also observed in the phantom (see Figures Fig. 4.3 and Fig. 4.5) and it is the expected behavior.

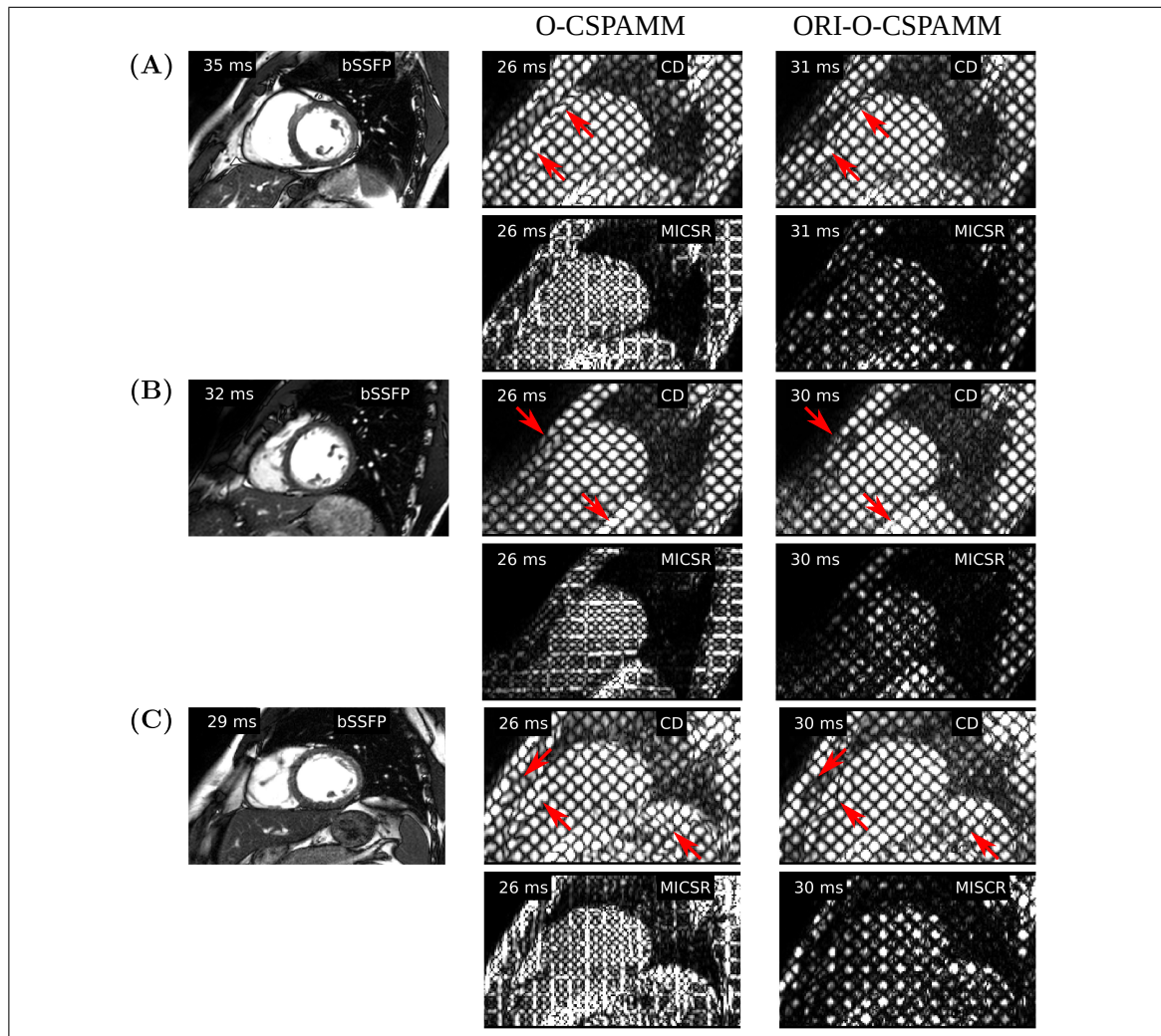


Figure 4.6. Images acquired using the O-CSPAMM (second column) and ORI-O-CSPAMM (third column) sequences and reconstructed using complex difference (CD) and MICSR for (A) volunteer 1, (B) volunteer 2, and (C) volunteer 3. Each volunteer has a bSSFP image as reference. The displayed images correspond to the end-diastolic cardiac phase. The discrepancies in the trigger delay times are due to the difference in the duration of the preparation pulses. The red arrows show the places where the grid is distorted by the presence of epicardial and subcutaneous fat. The images acquired with ORI-O-CSPAMM did not show any distortion in the places indicated by arrows.

Figure 7 shows the same results described for the Figure 6 but for an end-systolic cardiac phase. The signal of MCSR obtained from ORI-O-CSPAMM was higher than complex difference images in all the cases, which was also observed in the phantom (see Figure 3 and 5) and it is the expected behavior.

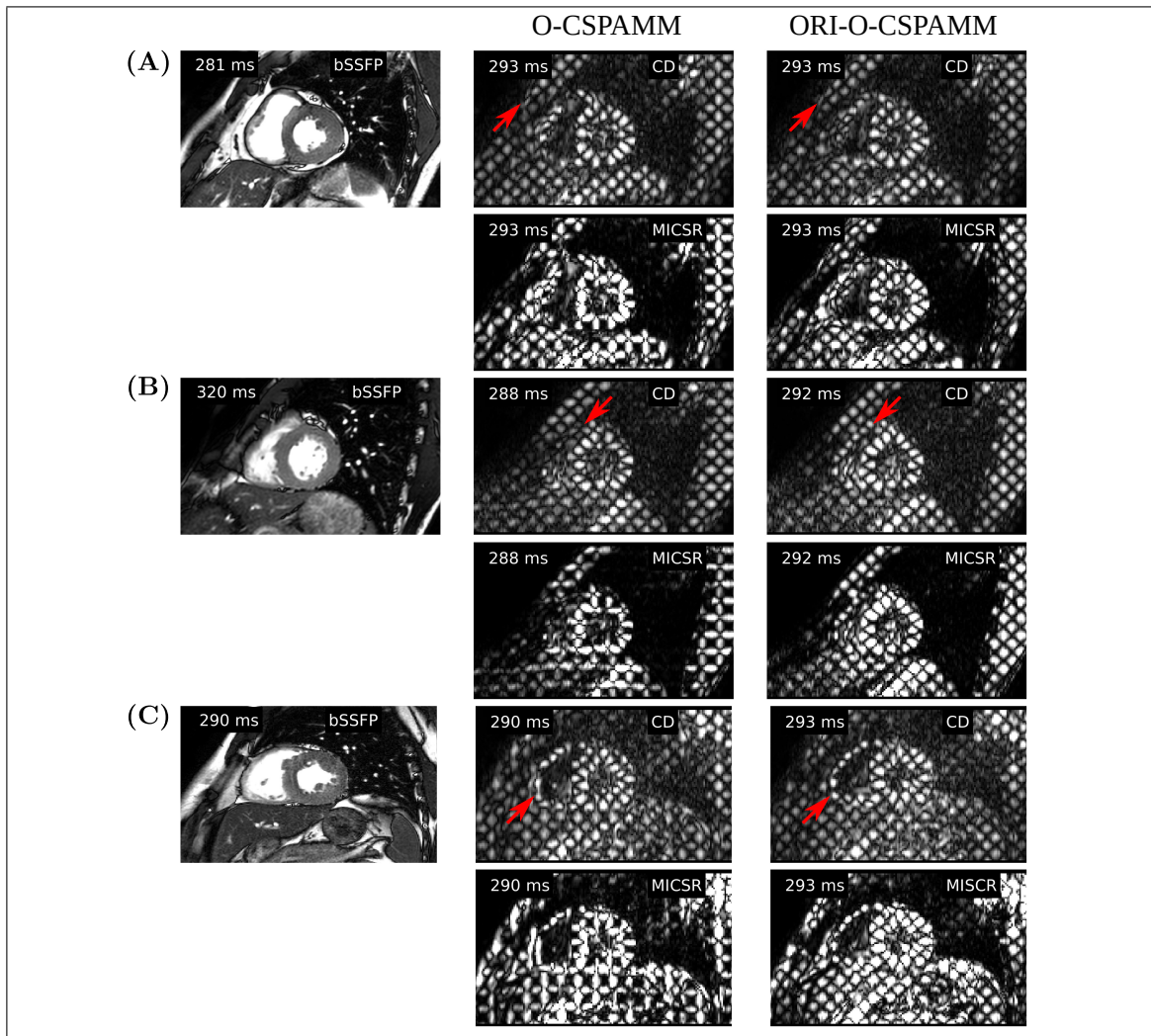


Figure 4.7. Images acquired using the O-CSPAMM (second column) and ORI-O-CSPAMM (third column) sequences and reconstructed using complex difference (CD) and MICSR for (A) volunteer 1, (B) volunteer 2, and (C) volunteer 3. Each volunteer has a bSSFP image as reference. The displayed images correspond to the end-systolic cardiac phase. The discrepancies in the trigger delay times are due to the difference in the duration of the preparation pulses and the cardiac cycle. The red arrows show the places where the grid is distorted by the presence of epicardial and subcutaneous fat. The images acquired with ORI-O-CSPAMM did not show any distortion in the places indicated by arrows.

#### 4.5. Discussion and conclusions

Although the CSPAMM sequence provides images that are suitable to assess not only the cardiac function but also to evaluate other organs (X. Liu & Prince, 2010; Lefebvre et al., 2019), its use remains limited for clinical applications due to the prolonged scan times. Additionally, images obtained from CSPAMM data can suffer from off-resonance effects generated during the tagging preparation. In this investigation a new acquisition sequence called ORI-O-CSPAMM was proposed to tackle these issues. ORI-O-CSPAMM allows the acquisition of a tagging grid free of DC frequencies and free of off-resonance effects in half of the acquisition time compared to the CSPAMM and ORI-CSPAMM sequences. Furthermore, ORI-O-CSPAMM is suitable to obtain MICSr images, which cannot be obtained with O-CSPAMM and could be beneficial to improve the tagging contrast for some clinical applications.

The most used tagging sequence is SPAMM, which can be used to obtain taglines or grids using only one acquisition. In the latter case, the grid modulation is obtained by two consecutive orthogonal SPAMM prepulses applied in the same preparation (Axel & Dougherty, 1989b), which does not affect the scan time. Compared to SPAMM, the proposed ORI-O-CSPAMM sequence takes twice the scan time to acquire a tagging grid with the benefit of removing the DC component, the off-resonance artifacts, and the spurious readout phases (in the case of MICSr images). In the same way, O-CSPAMM takes twice the scan time, and CSPAMM and ORI-CSPAMM take four times.

In healthy people, the primary source of off-resonance artifacts in cardiac tagged MR images is the epicardial fat, which can bias the estimation of motion and related parameters such as strain and twist. Nevertheless, if the heart is correctly segmented, the fat should not play a role in the estimation of strain parameters. However, in patients with fatty infiltration of the LV, i.e., where the fat is inside the cardiac tissue, sequences such as ORI-CSPAMM and ORI-O-CSPAMM could improve the cardiac motion and strain estimations. Moreover, a recent study has demonstrated that the strain estimated from tagged

MR images is a valuable marker for staging non-invasively liver fibrosis (Lefebvre et al., 2019) in Non-Alcoholic Fatty Liver Disease (NAFLD) patients. As the NAFLD stages are an inflammatory process in the presence of fat, we hypothesize that the use of ORI sequences can be helpful at the early stages of the disease. Even more, ORI-O-CSPAMM can be used in clinical protocols replacing SPAMM, which would increase the scan time of tagging grids by a factor two instead of four as it would be done with ORI-CSPAMM.

In phantom and in-vivo data, ORI-CSPAMM and the proposed ORI-O-CSPAMM sequences corrected the distortions generated by the vegetable oil and epicardial and subcutaneous fat (see Figures 4.3, 4.6, and 4.7). Also, we found that O-CSPAMM was particularly sensitive to unwanted high-frequency spectral peaks, which distorted the grid in the water part of the phantom images (see Fig. 4.3). The same behavior was not observed on in-vivo data. We hypothesize that although the complex difference did not remove these spectral peaks, the distortion generated in the water part of the phantom was not visible in tissues with shorter relaxation times such as those scanned in the in-vivo experiments due to the signal decay. Additionally, we demonstrated that the signal obtained with the ORI-O-CSPAMM sequence was comparable to ORI-CSPAMM and no major differences were observed (see Fig. 4.5).

In this investigation we could not reproduce the results obtained in (Reyhan et al., 2014) for ORI-CSPAMM in which the spurious phase gained during the readout was converted into a cosine modulation in complex difference images. However, this was also an issue with the three other sequences. In Fig. 4.8, the phase of the complex difference phantom images is non-zero due to the off-resonance effects and non-idealities during the readout. Here we showed that this adverse condition can only be corrected using MICSR.

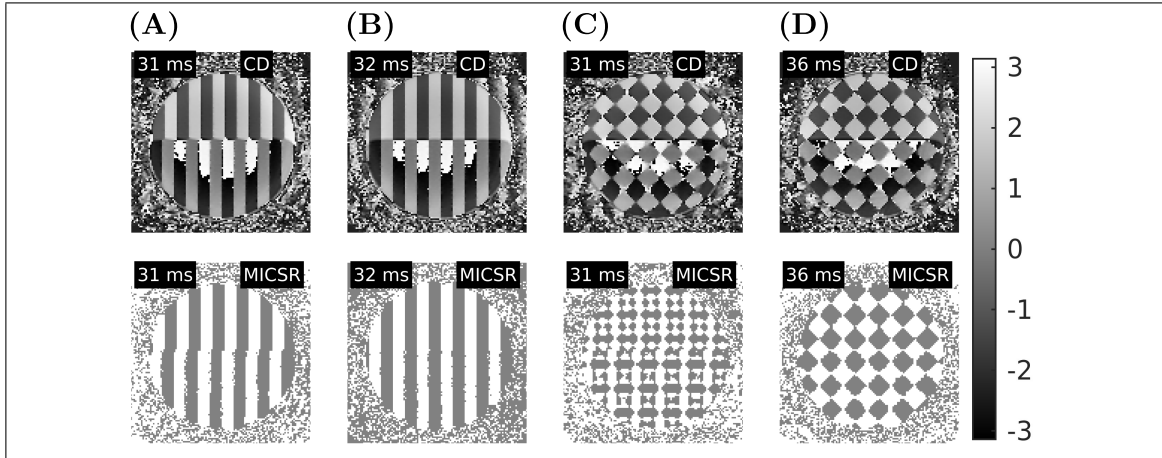


Figure 4.8. Phase of the complex difference (upper row) and MICSR images (bottom row) obtained from (A) CSPAMM, (B) ORI-CSPAMM, (C) O-CSPAMM, and (D) ORI-O-CSPAMM sequences. In complex difference images the phase is always non-zero while in MICSR images the phase is zero and  $\pi$  (the last is due that MICSR images have only real part that varies from positive to negative values).

Concerning the image quality obtained with MICSR images, in Fig. 4.6, results obtained from ORI-O-CSPAMM data showed low image quality compared to complex difference. This behavior is expected with MICSR because the term  $f_2$  is close to zero for short times (see 4.2b). In fact, for the trigger time of 36 ms showed in Fig. 4.6, the term  $1 - \exp(-t/T1)$  takes a value of 0.042, which makes the signal became much smaller. The low-quality images are less evident in the phantom data (see Fig. 4.3) as the coil was closer to the scanned bottle. In contrast, the quality of MICSR images in Fig. 4.7 looks better than the complex difference due to its signal behavior, which is bigger for a trigger time of 293 ms (see Figure Fig. 4.5).

When the maximum gradient of an MR system is limited by the hardware, ORI-O-CSPAMM also allowed the reduction of the gradient amplitude (or duration) into a 70% of the strength needed to generate the same tag periods with the other sequences. This was predicted by Eqs. 4.9a and 4.9b and confirmed by the phantom and in-vivo acquisitions (see Figures 4.3, 4.4, 4.6, and 4.7).

For the imaging parameters described in Table 4.1 for the acquisition of the volunteers, the average breath-hold duration with O-CSPAMM and ORI-O-CSPAMM sequences was 16 seconds, which is tolerable for almost any person, including patients with cardiopathies. With the CSPAMM and ORI-CSPAMM sequences, on the other hand, the average breath-hold needed to obtain 2D information would be around the 32 seconds (twice the time needed for the CSPAMM and ORI-CSPAMM scans in this investigation). The 16 seconds breath-hold duration could be further reduced using acceleration techniques such as half-scan (Feinberg, Hale, Watts, Kaufman, & Mark, 1986; MacFall, Pelc, & Vavrek, 1988), SENSE (Pruessmann, Weiger, Scheidegger, & Boesiger, 1999), and compressed sensing (Lustig, Donoho, & Pauly, 2007), or using faster readouts such as spirals (Ahn, Kim, & Cho, 1986; Börnert, Schomberg, Aldefeld, & Groen, 1999).

It must be noticed that the tagging preparation time needed to acquire ORI-O-CSPAMM data is a few milliseconds longer than with the other sequences due to the duplicated preparation. This is better appreciated in Figures 4.3, 4.6, and 4.7, where the trigger delay time of the first cardiac phase of the data acquired using ORI-O-CSPAMM was 5 ms longer than the CSPAMM and ORI-CSPAMM sequences. The total duration of the ORI-O-CSPAMM preparation for the imaging parameters given in Table 4.1 was 7.8 ms, whereas for CSPAMM, ORI-CSPAMM, and O-CSPAMM was 3.1, 3.9, and 3.1 ms respectively.

Although not considered in this study, ORI-O-CSPAMM can be made more robust by adding slice-selective RF pulses during the tagging preparation to obtain a Slice-Following sequence (Fischer et al., 1994), which handles the through-plane motion of the heart during the acquisition. Additionally, variable flip angle strategies can be used in the readout to improve the tagging contrast at the end of the scanned temporal window.

Strain analysis from MR images has been extensively used to assess the cardiac function (Smiseth, Torp, Opdahl, Haugaa, & Urheim, 2016). Feature tracking (Wu et al., 2014; Amzulescu et al., 2019) has gained a particular interest lately because it allows the strain analysis from bSSFP cine images, in detriment of techniques such as tagging MRI

(SPAMM and CSPAMM), Displacement Encoding with Stimulated Echoes (DENSE) (Aletras et al., 1999), and Strain-Encoded MRI (SENC) (Osman et al., 2001; Neizel et al., 2009). The advantage of feature tracking over the other techniques is that it does not need an additional image for strain analysis, although it can suffer from poor reproducibility for regional estimation (Bucius et al., 2020). Even though tagging (particularly CSPAMM), DENSE, and SENC are robust and highly reproducible for regional strain estimation (Bucius et al., 2020; Haggerty et al., 2013), they suffer from long scan time that difficult their translation to clinical protocols. The long scan time can be handled with ORI-O-CSPAMM, which allows the obtention, in only two scans, of grids suitable for any tagging post-processing method. Even for 3D scans, ORI-O-CSPAMM would still need two acquisitions to obtain a 3D grid by adding a third tagging preparation in the slice direction (for 3D images, CSPAMM and DENSE need 6 and 4 acquisitions, respectively). Compared to feature tracking, strain analysis from ORI-O-CSPAMM data would improve the regional strain estimation without a considerable increase of the scan time. Compared to SPAMM, it would remove biases related to off-resonance artifacts, DC contamination, and spurious readout phases.

In conclusion, we introduced a novel and fast sequence designed to remove off-resonance effects during the tagging preparation, obtain complex difference grids, and obtain MICSR grids in half of the scan time, which could allow its application to clinical protocols. The proposed ORI-O-CSPAMM sequence could be especially useful to study the function of organs suffering from diseases involving fat, such as fatty LV infiltration or NAFLD.

#### **4.6. Acknowledgments**

The authors thankfully acknowledge the financial support of the ANID Ph. D. Scholarship 21170592 as well as the project ANID-FONDECYT 1181057 and the ANID-Millennium Science Initiative Program - NCN17\_129.

## **5. FUTURE WORK AND PERSPECTIVES**

Additional work not listed in the publications' chapters is presented in this section. Three research ideas regarding the heart's and other organs' biomechanical quantification are divided into short-term and mid-term works. The investigation in a more advanced state is shown as short-term work.

### **5.1. Short-term: A Phase Complementary SPAMM (PCSPAMM) acquisition to quantify simultaneously tissue motion and flow velocity**

The cardiac function can be assessed using regional and simultaneous measurements of motion and velocities in the left-ventricle (Zhang et al., 2013). Previously, SPAMM EGG's (Sampath, Kim, Lederman, & McVeigh, 2008) and SPAMM-PAV (Zhang et al., 2011) have demonstrated to be useful techniques to obtain temporally correlated measures of both motion and velocity by combining a tagged MR acquisition with Phase-Contrast (PC) MRI. However, both approaches do not allow the measurement of early-systolic velocities and late-diastolic motion. In this work a new technique is presented, which combines a CSPAMM acquisition (Fischer et al., 1993) with PC, allowing the measurement of both motion and velocity across the whole cardiac cycle.

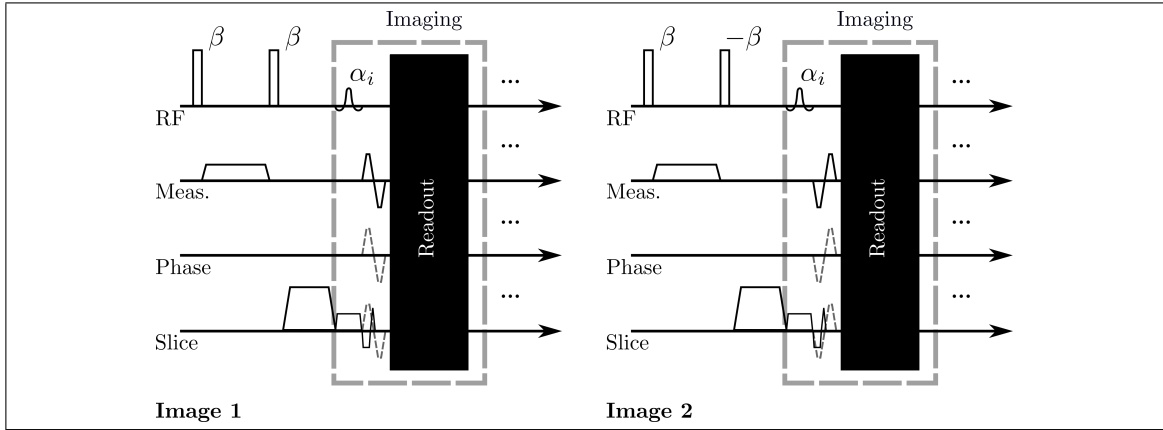


Figure 5.1. Pulse sequence diagram of the proposed PCSPAMM sequence. Bipolar gradients with opposite polarities are applied after the excitation RF pulse during the readout in each SPAMM acquisition.

Similarly to SPAMM-PAV, a 1-1 CSPAMM acquisition was combined with PC-MRI by adding a bipolar gradient with alternate polarities to each SPAMM acquisition (see Fig. 5.1). Two images containing information of the position and velocity of the tissue are measured, whose intensities are given by:

$$I_1 = a + b \cos(\phi_x(\mathbf{p}, t)) e^{+i\phi_{in}} e^{-i\phi_v}, \quad (5.1a)$$

$$I_2 = a - b \cos(\phi_x(\mathbf{p}, t)) e^{+i\phi_{in}} e^{+i\phi_v}, \quad (5.1b)$$

where  $a$  and  $b$  are increasing and decreasing functions depending on the position of the underlying tissue  $\mathbf{p}$ , the relaxation time  $T1$ , and the acquisition time  $t$ . In the previous expressions,  $\cos(\phi_x)$  denotes the sinusoidal tagging pattern,  $\phi_{in}$  the phase induced by field inhomogeneities, and  $\phi_v$  the phase induced by the bipolar gradients. From the expressions given in the Eq. 5.1,  $\phi_{in}$  and  $\phi_v$  are estimated using the following expressions:

$$\phi_{in} = \angle(I_1 + I_2), \quad (5.2a)$$

$$\phi_v = \angle(I_1 e^{-i\phi_{in}} + \text{conj}(I_2 e^{-i\phi_{in}})). \quad (5.2b)$$

With both phases estimated using Eq. 5.2, the images  $I_1$  and  $I_2$  are phase-corrected, allowing the generation of a CSPAMM image (Fischer et al., 1993).

Preliminary results consisting of a 4-chambers view of a healthy volunteer acquired in a 1.5T Achieva MR scanner (Philips, Best, Netherlands) are presented. Two sets of PCSPAMM images which allowed the obtention of tagged images in the read-out and phase directions and velocity encoded images in the phase and through-plane directions were acquired.

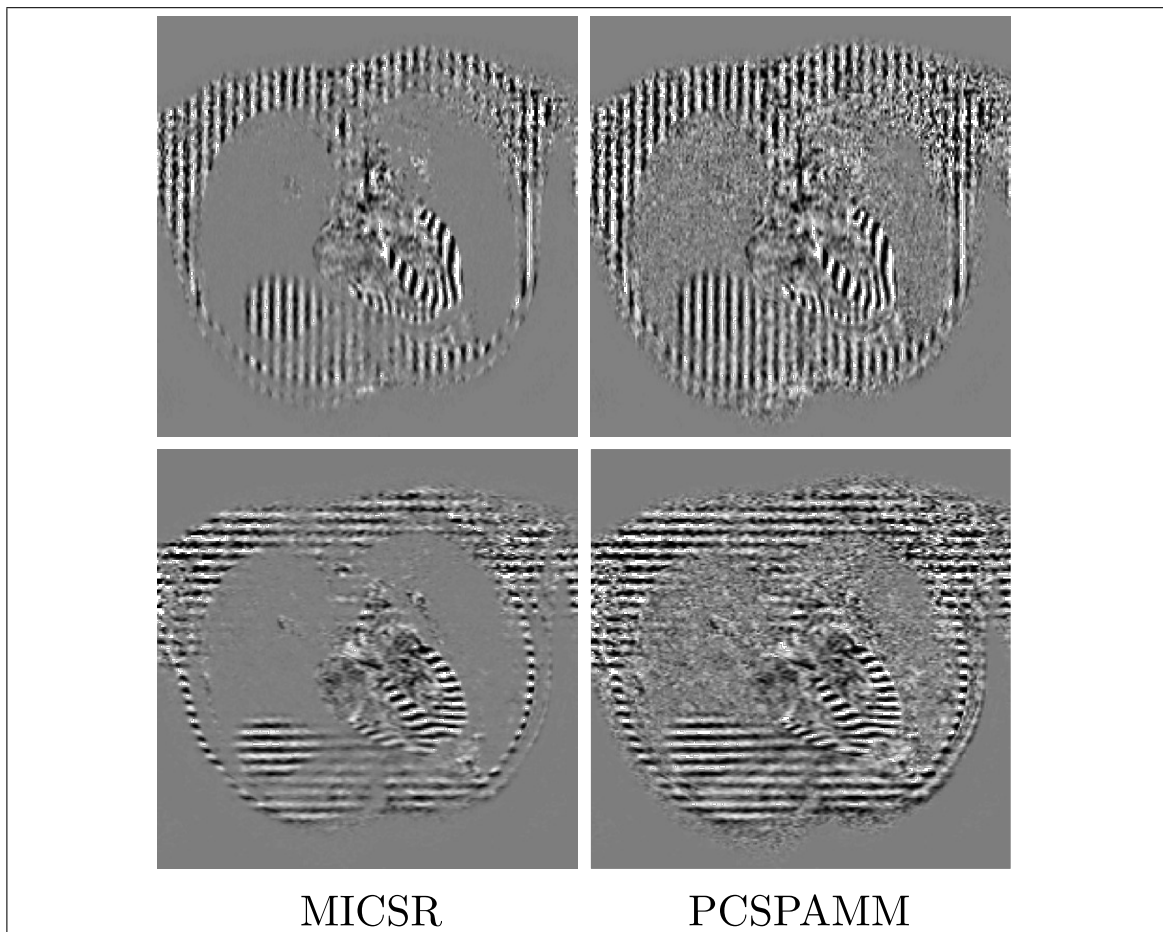


Figure 5.2. MICSr and real part of the CSPAMM image reconstructed from PCSPAMM data at end-systole. After the inhomogeneity correction, the CSPAMM image did not showed lines distortions, leading to a sinusoidal pattern similar to MICSr.

In Fig. 5.2 a comparison between the estimated CSPAMM image obtained with our proposal and the respective MICSr (NessAiver & Prince, 2003) image is presented. As

MICSR is a magnitude reconstruction, the phase of the acquisition did not distort the tag lines. In the case of the estimated CSPAMM image, the tagging pattern is similar to the obtained with MICSR, which means that the phase correction proposed in (5.2) works properly.

Fig. 5.3 shows the PC images obtained with our technique and a SPAMM-PAV-like reconstruction at the earliest systolic cardiac phase. Fig. 5.4 shows the mean velocities estimated using a SPAMM-PAV-like reconstruction and our proposal through the whole cardiac cycle. The mean values were calculated on a ROI positioned near the mitral valve (see Fig. 5.3). The estimated velocity with PCSPAMM was close to the SPAMM-PAV results, giving mean peak velocity magnitudes of  $57 \pm 10$  and  $55 \pm 11$ cm/s respectively.

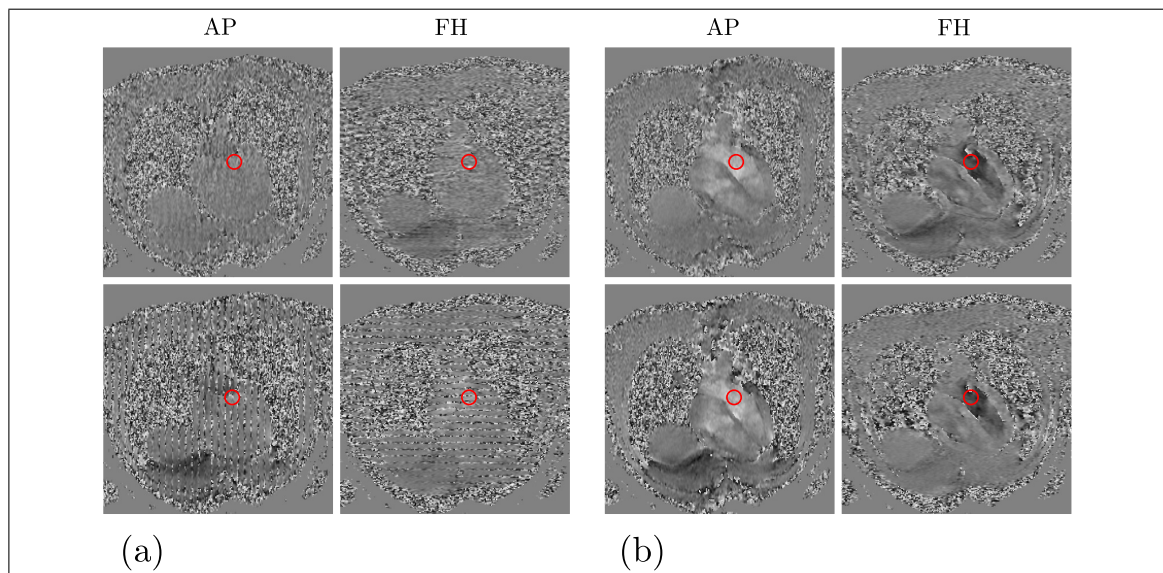


Figure 5.3. PC images estimated using PCSPAMM (top row) and a SPAMM-PAV-like reconstruction for trigger times of (a) 10 msec and (b) 505 ms. In both cases the velocity is shown in the AP and FH directions, and the red circle denotes the ROI placed near the mitral valve. In our proposal the phase is almost free of artifacts generated by the sinusoidal tagging modulation.

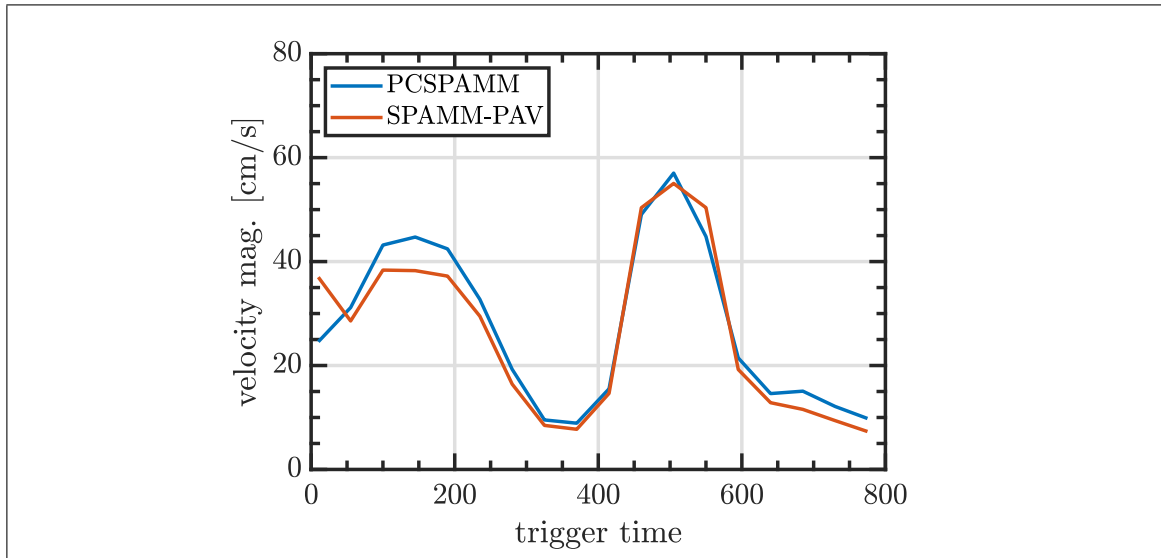


Figure 5.4. Mean velocity magnitude in a ROI placed close to the mitral valve obtained from PCSPAMM and SPAMM-PAV.

The proposed technique allows the estimation of a PC and a CSPAMM using two complementary acquisitions for each encoding direction. The estimated PC images were similar to the SPAMM-PAV estimations, but with our technique less artifacts were found at early diastolic cardiac phases (see Fig. 5.3). In the case of the CSPAMM image, the tag persistence is improved as the DC spectral component is removed, allowing the estimation of motion through the whole cardiac cycle.

## 5.2. Mid-term

We want to apply the proposed ORI-O-CSPAMM sequence and the HARP-I motion estimation technique to liver tagging MR images in the medium term. Recently, the connection between the liver strain obtained from tagged MR images and the stages of Non-Alcoholic Fatty Liver Disease (NAFLD) was investigated (Lefebvre et al., 2019), obtaining an excellent correlation between them. As the early stages of the NAFLD are

associated with the amount of fat in the liver, we hypothesize that off-resonance insensitive acquisition sequences such as the proposed ORI-O-CSPAMM would improve the estimation of liver strain as would reduce the off-resonance artifacts produced by fat.

Additionally, we want to investigate and improve the estimation of the Lagrangian strain tensor components that currently are not correctly estimated from MR images due mainly to technical limitations (Augustine et al., 2013; Swoboda et al., 2011; Haggerty et al., 2013). Remarkably, the radial cardiac strain is often misestimated due to the limited resolution through the left ventricle's radial direction. We hypothesize that the radial component can be estimated indirectly from the other tensor components, which do not suffer from the resolution issue.

## 6. CONCLUSIONS

A complete framework for estimating the cardiac motion and strain using tagged MR images was developed in this investigation. The presented methodologies represent novel quantitative tools for assessing the cardiac function, although they could also be applied to other organs. This research will help to scan faster and better tagging MR images and get better information from its processing.

Although the three research articles were not tested together, they can improve the tagged MR images' quality and the tissue motion and strain estimation using a joint framework. The first article elucidate which imaging and processing techniques work better under certain imaging conditions, which helps set the correct imaging parameters in the scanner and correctly choose the processing tools to be used.

The second article introduced a novel motion estimation technique called HARP-I that enhanced the motion and strain estimation from tagged MR images. The proposed technique handled some known issues of the current processing techniques such as large frame-to-frame displacements, through-plane displacements, and DC contamination. In combination with optimally acquired tagging images (i.e., using ORI-O-CSPAMM with parameters chosen according to the first publication), HARP-I would allow even more precise and accurate estimations.

The third article introduced a novel and fast acquisition sequence called ORI-O-CSPAMM, which allowed the acquisition of tagging grids in half of the scan time. Combined with tag periods and pixel sizes discussed in the first article, the proposed sequence would allow the acquisition of high-quality tagging images free of DC frequencies and off-resonance artifacts and with image characteristics that make it suitable for motion estimation techniques.

Overall, the methods proposed in this thesis are an improvement to the state-of-the-art tagging acquisition and processing techniques and could improve the study of the cardiac function as well as other organs.

## REFERENCES

- Abd-Elmoniem, K. Z., Stuber, M., Osman, N. F., & Prince, J. L. (2005). ZHARP: Three-dimensional motion tracking from a single image plane. In *Lecture notes in computer science* (Vol. 3565, pp. 639–651). doi: 10.1007/11505730\_53
- Adamczak, D. M., Oduah, M. T., Kiebalo, T., Nartowicz, S., Bęben, M., Pochylski, M., ... Straburzyńska-Migaj, E. (2020, sep). *Heart Failure with Preserved Ejection Fraction—a Concise Review* (Vol. 22) (No. 9). Springer. doi: 10.1007/s11886-020-01349-3
- Ahn, C. B., Kim, J. H., & Cho, Z. H. (1986). High-Speed Spiral-Scan Echo Planar NMR Imaging-I. *IEEE Transactions on Medical Imaging*, 5(1), 2–7. doi: 10.1109/TMI.1986.4307732
- Aletras, A. H., Ding, S., Balaban, R. S., & Wen, H. (1999). DENSE: Displacement Encoding with Stimulated Echoes in Cardiac Functional MRI. *Journal of Magnetic Resonance*, 137(1), 247–252. doi: 10.1006/jmre.1998.1676
- Amini, A. A., Chen, Y., Curwen, R. W., Mani, V., & Sun, J. (1998). Coupled B-snake grids and constrained thin-plate splines for analysis of 2-D tissue deformations from tagged MRI. *IEEE Transactions on Medical Imaging*, 17(3), 344–356. doi: 10.1109/42.712124
- Amzulescu, M. S., De Craene, M., Langet, H., Pasquet, A., Vancraeynest, D., Pouleur, A. C., ... Gerber, B. L. (2019, jun). Myocardial strain imaging: review of general principles, validation, and sources of discrepancies. *European Heart Journal - Cardiovascular Imaging*, 20(6), 605–619. doi: 10.1093/ehjci/jez041
- Arts, T., Prinzen, F. W., Delhaas, T., Milles, J. R., Rossi, A. C., & Clarysse, P. (2010, may). Mapping displacement and deformation of the heart with local sine-wave modeling. *IEEE Transactions on Medical Imaging*, 29(5), 1114–1123. doi: 10.1109/TMI.2009.2037955
- Auger, D. A., Bilchick, K. C., Gonzalez, J. A., Cui, S. X., Holmes, J. W., Kramer, C. M.,

- ... Epstein, F. H. (2017, sep). Imaging left-ventricular mechanical activation in heart failure patients using cine DENSE MRI: Validation and implications for cardiac resynchronization therapy. *Journal of Magnetic Resonance Imaging*, 46(3), 887–896. doi: 10.1002/jmri.25613
- Auger, D. A., Cai, X., Sun, C., & Epstein, F. H. (2018). Improved phase unwrapping algorithm for automatic cine DENSE strain analysis using phase predictions and region growing. In *Proceedings of the 27th annual meeting of the ismrm*. ISMRM.
- Augustine, D., Lewandowski, A. J., Lazdam, M., Rai, A., Francis, J., Myerson, S., ... Leeson, P. (2013). Global and regional left ventricular myocardial deformation measures by magnetic resonance feature tracking in healthy volunteers: Comparison with tagging and relevance of gender. *Journal of Cardiovascular Magnetic Resonance*, 15(1), 15–17. doi: 10.1186/1532-429X-15-8
- Axel, L., & Dougherty, L. (1989a). MR imaging of motion with spatial modulation of magnetization. *Radiology*, 171(3), 841–845. doi: 10.1148/radiology.171.3.2717762
- Axel, L., & Dougherty, L. (1989b). Heart wall motion: Improved method for spatial modulation of magnetization for MR imaging. *Radiology*, 172(2), 349–350. doi: 10.1148/radiology.172.2.2748813
- Axel, L., Montillo, A., & Kim, D. (2005). Tagged magnetic resonance imaging of the heart: A survey. *Medical Image Analysis*, 9(4 SPEC. ISS.), 376–393. doi: 10.1016/j.media.2005.01.003
- Bender, J. A., Ahmad, R., & Simonetti, O. P. (2013, mar). The importance of k-space trajectory on off-resonance artifact in segmented echo-planar imaging. *Concepts in Magnetic Resonance Part A: Bridging Education and Research*, 42 A(2), 23–31. doi: 10.1002/cmra.21255
- Bertoglio, C., Moireau, P., & Gerbeau, J.-F. (2012, apr). Sequential parameter estimation for fluid-structure problems: Application to hemodynamics. *International Journal for Numerical Methods in Biomedical Engineering*, 28(4), 434–455. doi: 10.1002/cnm.1476

- Bioucas-Dias, J. M., & Valadao, G. (2007). Phase unwrapping via graph cuts. *IEEE Transactions on Image Processing*, 16(3), 698–709. doi: 10.1109/TIP.2006.888351
- Börnert, P., Schomberg, H., Aldefeld, B., & Groen, J. (1999, oct). Improvements in spiral MR imaging. *Magma: Magnetic Resonance Materials in Physics, Biology, and Medicine*, 9(1-2), 29–41. Retrieved from <https://link.springer.com/article/10.1007/BF02634590> doi: 10.1007/bf02634590
- Bucius, P., Erley, J., Tanacli, R., Zieschang, V., Giusca, S., Korosoglou, G., ... Kelle, S. (2020). Comparison of feature tracking, fast-SENC, and myocardial tagging for global and segmental left ventricular strain. *ESC Heart Failure*, 7(2), 523–532. doi: 10.1002/ehf2.12576
- Budge, L. P., Helms, A. S., Salerno, M., Kramer, C. M., Epstein, F. H., & Bilchick, K. C. (2012, aug). MR Cine DENSE Dyssynchrony Parameters for the Evaluation of Heart Failure: Comparison With Myocardial Tissue Tagging. *JACC: Cardiovascular Imaging*, 5(8), 789–797. doi: 10.1016/J.JCMG.2011.12.024
- Buhmann, M. D. (2003). *Radial Basis Functions: Theory and Implementations*. Cambridge: Cambridge University Press. doi: 10.1017/CBO9780511543241
- Burkhardt, B. E. U., Velasco Forte, M. N., Durairaj, S., Rafiq, I., Valverde, I., Tandon, A., ... Hussain, T. (2017, feb). Timely Pulmonary Valve Replacement May Allow Preservation of Left Ventricular Circumferential Strain in Patients with Tetralogy of Fallot. *Frontiers in Pediatrics*, 5, 39. doi: 10.3389/fped.2017.00039
- Cao, J. J., Ngai, N., Duncanson, L., Cheng, J., Gliganic, K., & Chen, Q. (2018). A comparison of both DENSE and feature tracking techniques with tagging for the cardiovascular magnetic resonance assessment of myocardial strain. *Journal of Cardiovascular Magnetic Resonance*, 20. doi: 10.1186/s12968-018-0448-9
- Carr, J. C., Beatson, R. K., McCallum, B. C., Fright, W. R., McLennan, T. J., & Mitchell, T. J. (2003). Smooth surface reconstruction from noisy range data. In *Proceedings of the 1st international conference on computer graphics and interactive techniques in australasia and south east asia, graphite '03* (p. 119). New York, New York, USA: ACM Press. doi: 10.1145/604471.604495

- Cerqueira, M. D., Weissman, N. J., Dilsizian, V., Jacobs, A. K., Kaul, S., Laskey, W. K., . . . Verani, M. S. (2002, jan). *Standardized myocardial segmentation and nomenclature for tomographic imaging of the heart: A Statement for Healthcare Professionals from the Cardiac Imaging Committee of the Council on Clinical Cardiology of the American Heart Association* (Vol. 105) (No. 4). Lippincott Williams & Wilkins. doi: 10.1161/hc0402.102975
- Chabiniok, R., Moireau, P., Lesault, P. F., Rahmouni, A., Deux, J. F., & Chapelle, D. (2012, may). Estimation of tissue contractility from cardiac cine-MRI using a biomechanical heart model. *Biomechanics and Modeling in Mechanobiology*, 11(5), 609–630. doi: 10.1007/s10237-011-0337-8
- Chandrashekhara, R., Mohiaddin, R., Razavi, R., & Rueckert, D. (2007). Nonrigid image registration with subdivision lattices: Application to cardiac mr image analysis. In *Proceedings of the 10th international conference on medical image computing and computer-assisted intervention - volume part i* (p. 335–342). Berlin, Heidelberg: Springer-Verlag.
- Chandrashekhara, R., Rao, A., Sanchez-Ortiz, G. I., Mohiaddin, R. H., & Rueckert, D. (2003). Construction of a statistical model for cardiac motion analysis using nonrigid image registration. *Lecture Notes in Computer Science (including sub-series Lecture Notes in Artificial Intelligence and Lecture Notes in Bioinformatics)*, 2732, 599–610. Retrieved from [https://link.springer.com/chapter/10.1007/978-3-540-45087-0\\_50](https://link.springer.com/chapter/10.1007/978-3-540-45087-0_50) doi: 10.1007/978-3-540-45087-0\_50
- Chen, L. (2001, dec). Quantification of Left Ventricular Function with Contrast-Enhanced Harmonic Colour Doppler and a Semiautomated Boundary Detection Algorithm in Technically Difficult Patients: Feasibility, Accuracy, and Inter-observer Variability. *European Journal of Echocardiography*, 2(4), 253–261. doi: 10.1053/euje.2001.0104
- Chen, T., & Axel, L. (2006). Using gabor filter banks and temporal-spatial constraints to compute 3D myocardium strain. *Annual International Conference of the IEEE Engineering in Medicine and Biology - Proceedings*, 4755–4758. doi:

10.1109/IEMBS.2006.259875

- Chen, T., Wang, X., Chung, S., Metaxas, D., & Axel, L. (2010). Automated 3D motion tracking using gabor filter bank, robust point matching, and deformable models. *IEEE Transactions on Medical Imaging*, 29(1), 1–11. doi: 10.1109/TMI.2009.2021041
- Chitiboi, T., & Axel, L. (2017). Magnetic resonance imaging of myocardial strain: A review of current approaches. *Journal of Magnetic Resonance Imaging*, 46(5), 1263–1280. doi: 10.1002/jmri.25718
- Cikes, M., & Solomon, S. D. (2016, jun). Beyond ejection fraction: An integrative approach for assessment of cardiac structure and function in heart failure. *European Heart Journal*, 37(21), 1642–1650. doi: 10.1093/eurheartj/ehv510
- Claus, P., Omar, A. M. S., Pedrizzetti, G., Sengupta, P. P., & Nagel, E. (2015). Tissue Tracking Technology for Assessing Cardiac Mechanics: Principles, Normal Values, and Clinical Applications. *JACC: Cardiovascular Imaging*, 8(12), 1444–1460. doi: 10.1016/j.jcmg.2015.11.001
- Dougherty, L., Asmuth, J. C., Blom, A. S., Axel, L., & Kumar, R. (1999). Validation of an optical flow method for tag displacement estimation. *IEEE Transactions on Medical Imaging*, 18(4), 359–363. doi: 10.1109/42.768845
- ElDeeb, S. M., & Fahmy, A. S. (2016). Accurate harmonic phase tracking of tagged MRI using locally-uniform myocardium displacement constraint. *Medical Engineering and Physics*, 38(11), 1305–1313. doi: 10.1016/j.medengphy.2016.08.002
- Epstein, F. H., & Gilson, W. D. (2004, oct). Displacement-encoded cardiac MRI using cosine and sine modulation to eliminate (CANSSEL) artifact-generating echoes. *Magnetic Resonance in Medicine*, 52(4), 774–781. doi: 10.1002/mrm.20232
- Ernande, L., Thibault, H., Bergerot, C., Moulin, P., Wen, H., Derumeaux, G., & Croisille, P. (2012, nov). Systolic Myocardial Dysfunction in Patients with Type 2 Diabetes Mellitus: Identification at MR Imaging with Cine Displacement Encoding with Stimulated Echoes. *Radiology*, 265(2), 402–409. doi: 10.1148/radiol.12112571

- Fahmy, A. S., Basha, T. A., & Osman, N. F. (2009). Inherent fat cancellation in complementary spatial modulation of magnetization. *Magnetic Resonance in Medicine*, *61*(1), 234–238. doi: 10.1002/mrm.21811
- Feinberg, D. A., Hale, J. D., Watts, J. C., Kaufman, L., & Mark, A. (1986, nov). Halving MR imaging time by conjugation: Demonstration at 3.5 kG. *Radiology*, *161*(2), 527–531. Retrieved from <https://pubs.rsna.org/doi/abs/10.1148/radiology.161.2.3763926> doi: 10.1148/radiology.161.2.3763926
- Fischer, S. E., McKinnon, G. C., Maier, S. E., & Boesiger, P. (1993, aug). Improved myocardial tagging contrast. *Magnetic Resonance in Medicine*, *30*(2), 191–200. doi: 10.1002/mrm.1910300207
- Fischer, S. E., McKinnon, G. C., Scheidegger, M. B., Prins, W., Meier, D., & Boesiger, P. (1994, apr). True myocardial motion tracking. *Magnetic Resonance in Medicine*, *31*(4), 401–413. doi: 10.1002/mrm.1910310409
- Florack, L., Van Assen, H., & Suinesiaputra, A. (2007). Dense multiscale motion extraction from cardiac cine MR tagging using harp technology. *Proceedings of the IEEE International Conference on Computer Vision*. doi: 10.1109/ICCV.2007.4409147
- Fonseca, C. G., Dissanayake, A. M., Doughty, R. N., Whalley, G. A., Gamble, G. D., Cowan, B. R., ... Young, A. A. (2004, dec). Three-dimensional assessment of left ventricular systolic strain in patients with type 2 diabetes mellitus, diastolic dysfunction, and normal ejection fraction. *The American Journal of Cardiology*, *94*(11), 1391–1395. doi: 10.1016/J.AMJCARD.2004.07.143
- Genet, M., Stoeck, C. T., von Deuster, C., Lee, L. C., & Kozerke, S. (2018, dec). Equilibrated warping: Finite element image registration with finite strain equilibrium gap regularization. *Medical Image Analysis*, *50*, 1–22. doi: 10.1016/j.media.2018.07.007
- Ghiglia, D. C., & Pritt, M. D. (1998). *Two-dimensional phase unwrapping: theory, algorithms, and software*. Wiley.
- Gilliam, A. D., & Epstein, F. H. (2012). Automated motion estimation for 2-D cine DENSE MRI. *IEEE Transactions on Medical Imaging*, *31*(9), 1669–1681. doi:

10.1109/TMI.2012.2195194

- Gilliam, A. D., & Suever, J. D. (2016). *DENSEanalysis*. \url = {<https://github.com/denseanalysis/denseanalysis>}.
- Gilson, W. D., Yang, Z., French, B. A., & Epstein, F. H. (2004, apr). Complementary displacement-encoded MRI for contrast-enhanced infarct detection and quantification of myocardial function in mice. *Magnetic Resonance in Medicine*, *51*(4), 744–752. doi: 10.1002/mrm.20003
- Gorcsan, J., & Tanaka, H. (2011). Echocardiographic assessment of myocardial strain. *Journal of the American College of Cardiology*, *58*(14), 1401–1413. doi: 10.1016/j.jacc.2011.06.038
- Goto, Y., Ishida, M., Takase, S., Sigfridsson, A., Uno, M., Nagata, M., ... Sakuma, H. (2017, may). Comparison of Displacement Encoding With Stimulated Echoes to Magnetic Resonance Feature Tracking for the Assessment of Myocardial Strain in Patients With Acute Myocardial Infarction. *The American Journal of Cardiology*, *119*(10), 1542–1547. doi: 10.1016/J.AMJCARD.2017.02.029
- Götte, M. J., Germans, T., Rüssel, I. K., Zwanenburg, J. J., Marcus, J. T., van Rossum, A. C., & van Veldhuisen, D. J. (2006, nov). Myocardial Strain and Torsion Quantified by Cardiovascular Magnetic Resonance Tissue Tagging. Studies in Normal and Impaired Left Ventricular Function. *Journal of the American College of Cardiology*, *48*(10), 2002–2011. doi: 10.1016/j.jacc.2006.07.048
- Götte, M. J., Van Rossum, A. C., Twisk, J. W., Kuijer, J. P., Marcus, J. T., & Visser, C. A. (2001, mar). Quantification of regional contractile function after infarction: Strain analysis superior to wall thickening analysis in discriminating infarct from remote myocardium. *Journal of the American College of Cardiology*, *37*(3), 808–817. doi: 10.1016/S0735-1097(00)01186-4
- Gurtin, M. E., Fried, E., & Anand, L. (2010). *The Mechanics and Thermodynamics of Continua*. Cambridge: Cambridge University Press. doi: 10.1017/CBO9780511762956
- Guttman, M. A., Prince, J. L., & McVeigh, E. R. (1994). Tag and Contour Detection in

- Tagged MR Images of the Left Ventricle. *IEEE Transactions on Medical Imaging*, 13(1), 74–88. doi: 10.1109/42.276146
- Haber, I., Metaxas, D. N., & Axel, L. (2000, dec). Three-dimensional motion reconstruction and analysis of the right ventricle using tagged MRI. *Medical Image Analysis*, 4(4), 335–355. doi: 10.1016/S1361-8415(00)00028-1
- Hadjicharalambous, M., Asner, L., Chabiniok, R., Sammut, E., Wong, J., Peressutti, D., ... Nordsletten, D. (2017, mar). Non-invasive Model-Based Assessment of Passive Left-Ventricular Myocardial Stiffness in Healthy Subjects and in Patients with Non-ischemic Dilated Cardiomyopathy. *Annals of Biomedical Engineering*, 45(3), 605–618. doi: 10.1007/s10439-016-1721-4
- Haggerty, C. M., Kramer, S. P., Binkley, C. M., Powell, D. K., Mattingly, A. C., Charnigo, R., ... Fornwalt, B. K. (2013, aug). Reproducibility of cine displacement encoding with stimulated echoes (DENSE) cardiovascular magnetic resonance for measuring left ventricular strains, torsion, and synchrony in mice. *Journal of Cardiovascular Magnetic Resonance*, 15(1), 71. Retrieved from <http://jcmr-online.biomedcentral.com/articles/10.1186/1532-429X-15-71> doi: 10.1186/1532-429X-15-71
- Hor, K. N., Wansapura, J., Markham, L. W., Mazur, W., Cripe, L. H., Fleck, R., ... Gottliebson, W. M. (2009). Circumferential Strain Analysis Identifies Strata of Cardiomyopathy in Duchenne Muscular Dystrophy. A Cardiac Magnetic Resonance Tagging Study. *Journal of the American College of Cardiology*, 53(14), 1204–1210. doi: 10.1016/j.jacc.2008.12.032
- Huang, J., Abendschein, D., Dâvila-Român, V. G., & Amini, A. A. (1999). Spatio-temporal tracking of myocardial deformations with a 4-D B-spline model from tagged MRI. *IEEE Transactions on Medical Imaging*, 18(10), 957–972. doi: 10.1109/42.811299
- Ibrahim, E. S., Swanson, S., Stojanovska, J., Duvernoy, C., & Pop-Busui, R. (2016). Harmonic phase versus sine-wave modulation for measuring regional heart function from tagged MRI images. *Proceedings - International Symposium on Biomedical*

- Imaging, 2016-June*, 444–447. doi: 10.1109/ISBI.2016.7493303
- Ibrahim, E.-S. H. (2011, jul). Myocardial tagging by Cardiovascular Magnetic Resonance: evolution of techniques–pulse sequences, analysis algorithms, and applications. *Journal of Cardiovascular Magnetic Resonance*, 13(1), 36. doi: 10.1186/1532-429X-13-36
- Ibrahim, E. S. H., Stojanovska, J., Hassanein, A., Duvernoy, C., Croisille, P., Pop-Busui, R., & Swanson, S. D. (2018). Regional cardiac function analysis from tagged MRI images. Comparison of techniques: Harmonic-Phase (HARP) versus Sinusoidal-Modeling (SinMod) analysis. *Magnetic Resonance Imaging*, 54(April), 271–282. doi: 10.1016/j.mri.2018.05.008
- Imperiale, A., Chabiniok, R., Moireau, P., & Chapelle, D. (2011). Constitutive parameter estimation methodology using tagged-MRI data. In *Lecture notes in computer science (including subseries lecture notes in artificial intelligence and lecture notes in bioinformatics)* (Vol. 6666 LNCS, pp. 409–417). Springer, Berlin, Heidelberg. doi: 10.1007/978-3-642-21028-0\_52
- Jeung, M. Y., Germain, P., Croisille, P., Ghannudi, S. E., Roy, C., & Gangi, A. (2012). Myocardial tagging with MR imaging: Overview of normal and pathologic findings. *Radiographics*, 32(5), 1381–1398. doi: 10.1148/rg.325115098
- Kar, J., Cohen, M. V., McQuiston, S. A., Figarola, M. S., & Malozzi, C. M. (2019, oct). Can post-chemotherapy cardiotoxicity be detected in long-term survivors of breast cancer via comprehensive 3D left-ventricular contractility (strain) analysis? *Magnetic Resonance Imaging*, 62, 94–103. doi: 10.1016/j.mri.2019.06.020
- Kerwin, W. S., & Prince, J. L. (1998, dec). Cardiac material markers from tagged MR images. *Medical Image Analysis*, 2(4), 339–353. doi: 10.1016/S1361-8415(98)80015-7
- Khalifa, A. M., Youssef, A. B. M., & Osman, N. F. (2005). Improved Harmonic Phase (HARP) method for motion tracking a tagged cardiac MR images. *Annual International Conference of the IEEE Engineering in Medicine and Biology - Proceedings*, 7 VOLS, 4298–4301. doi: 10.1109/iembs.2005.1615415

- Kim, D., Gilson, W. D., Kramer, C. M., & Epstein, F. H. (2004). Myocardial Tissue Tracking with Two-dimensional Cine Displacement-encoded MR Imaging: Development and Initial Evaluation. *Radiology*, *230*(3), 862–871. doi: 10.1148/radiol.2303021213
- Ledesma-Carbayo, M. J., Derbyshire, J. A., Sampath, S., Santos, A., Desco, M., & McVeigh, E. R. (2008, jan). Unsupervised estimation of myocardial displacement from tagged MR sequences using nonrigid registration. *Magnetic Resonance in Medicine*, *59*(1), 181–189. Retrieved from <http://doi.wiley.com/10.1002/mrm.21444> doi: 10.1002/mrm.21444
- Lefebvre, T., Petitclerc, L., Hébert, M., Bilodeau, L., Sebastiani, G., Olivié, D., ... Tang, A. (2019, oct). MRI cine-tagging of cardiac-induced motion for noninvasive staging of liver fibrosis. *Journal of Magnetic Resonance Imaging*, *jmri.26935*. Retrieved from <https://onlinelibrary.wiley.com/doi/abs/10.1002/jmri.26935> doi: 10.1002/jmri.26935
- Leitman, M., Lysyansky, P., Sidenko, S., Shir, V., Peleg, E., Binenbaum, M., ... Vered, Z. (2004). Two-dimensional strain-A novel software for real-time quantitative echocardiographic assessment of myocardial function. *Journal of the American Society of Echocardiography*, *17*(10), 1021–1029. doi: 10.1016/j.echo.2004.06.019
- Li, B., Liu, Y., Occleshaw, C. J., Cowan, B. R., & Young, A. A. (2010). In-line automated tracking for ventricular function with magnetic resonance imaging. *JACC: Cardiovascular Imaging*, *3*(8), 860–866. doi: 10.1016/j.jcmg.2010.04.013
- Li, B., Young, A. A., & Cowan, B. R. (2008). GPU accelerated non-rigid registration for the evaluation of cardiac function. *Medical Image Computing and Computer-Assisted Intervention—MICCAI 2008*, *11*(Pt 2), 880–887.
- Liao, R., Turk, E. A., Zhang, M., Luo, J., Ellen Grant, P., Adalsteinsson, E., & Golland, P. (2016, oct). Temporal registration in in-utero volumetric MRI time series. In *Lecture notes in computer science (including subseries lecture notes in artificial intelligence and lecture notes in bioinformatics)* (Vol. 9902 LNCS, pp. 54–62). Springer Verlag. Retrieved from <https://link.springer.com/chapter/10.1007/978>

-3-319-46726-9{-}7 doi: 10.1007/978-3-319-46726-9\_7

- Liu, H., Wang, J., Xu, X., Song, E., Wang, Q., Jin, R., ... Fei, B. (2014). A robust and accurate center-frequency estimation (RACE) algorithm for improving motion estimation performance of SinMod on tagged cardiac MR images without known tagging parameters. *Magnetic Resonance Imaging*, 32(9), 1139–1155. doi: 10.1016/j.mri.2014.07.005
- Liu, X., Murano, E., Stone, M., & Prince, J. L. (2007). HARP tracking refinement using seeded region growing. *2007 4th IEEE International Symposium on Biomedical Imaging: From Nano to Macro - Proceedings*, 372–375. doi: 10.1109/ISBI.2007.356866
- Liu, X., & Prince, J. L. (2010). Shortest path refinement for motion estimation from tagged MR images. *IEEE Transactions on Medical Imaging*, 29(8), 1560–1572. doi: 10.1109/TMI.2010.2045509
- Lustig, M., Donoho, D., & Pauly, J. M. (2007, dec). Sparse MRI: The application of compressed sensing for rapid MR imaging. *Magnetic Resonance in Medicine*, 58(6), 1182–1195. Retrieved from <http://doi.wiley.com/10.1002/mrm.21391> doi: 10.1002/mrm.21391
- MacFall, J. R., Pelc, N. J., & Vavrek, R. M. (1988, mar). Correction of spatially dependent phase shifts for partial Fourier imaging. *Magnetic Resonance Imaging*, 6(2), 143–155. doi: 10.1016/0730-725X(88)90444-4
- MacGowan, G. A., Shapiro, E. P., Azhari, H., Siu, C. O., Hees, P. S., Hutchins, G. M., ... Rademakers, F. E. (1997, jul). Noninvasive Measurement of Shortening in the Fiber and Cross-Fiber Directions in the Normal Human Left Ventricle and in Idiopathic Dilated Cardiomyopathy. *Circulation*, 96(2), 535–541. doi: 10.1161/01.CIR.96.2.535
- Mangion, K., Carrick, D., Carberry, J., Mahrous, A., McComb, C., Oldroyd, K. G., ... Berry, C. (2019, feb). Circumferential Strain Predicts Major Adverse Cardiovascular Events Following an Acute ST-Segment–Elevation Myocardial Infarction. *Radiology*, 290(2), 329–337. doi: 10.1148/radiol.2018181253

- McClelland, J. R., Hawkes, D. J., Schaeffter, T., & King, A. P. (2013, jan). *Respiratory motion models: A review* (Vol. 17) (No. 1). Elsevier. doi: 10.1016/j.media.2012.09.005
- McCulloch, A. (2000, sep). Cardiac Biomechanics. In J. Bronzino (Ed.), *Biomedical engineering handbook* (1st ed., pp. 27–54). CRC Press. doi: 10.1201/9781420008197.ch8
- Mella, H., Mura, J., Wang, H., Taylor, M. D., Chabiniok, R., Tintera, J., ... Uribe, S. (2021). HARP-I: A Harmonic Phase Interpolation Method for the Estimation of Motion from Tagged MR Images. *IEEE Transactions on Medical Imaging*, 40(4), 1240–1252. doi: 10.1109/TMI.2021.3051092
- Miller, C. A., Borg, A., Clark, D., Steadman, C. D., McCann, G. P., Clarysse, P., ... Schmitt, M. (2013). Comparison of local sine wave modeling with harmonic phase analysis for the assessment of myocardial strain. *Journal of Magnetic Resonance Imaging*, 38(2), 320–328. doi: 10.1002/jmri.23973
- Moerman, K. M., Sprengers, A. M., Simms, C. K., Lamerichs, R. M., Stoker, J., & Nederveen, A. J. (2011). Validation of SPAMM tagged MRI based measurement of 3D soft tissue deformation. *Medical Physics*, 38(3), 1248–1260. doi: 10.1118/1.3533942
- Morton, G., Schuster, A., Jogiya, R., Kutty, S., Beerbaum, P., & Nagel, E. (2012). Inter-study reproducibility of cardiovascular magnetic resonance myocardial feature tracking. *Journal of Cardiovascular Magnetic Resonance*, 14(1), 43. Retrieved from <http://jcmr-online.biomedcentral.com/articles/10.1186/1532-429X-14-43> doi: 10.1186/1532-429X-14-43
- Mura, J., Pino, A. M., Sotelo, J., Valverde, I., Tejos, C., Andia, M. E., ... Uribe, S. (2016, oct). Enhancing the Velocity Data From 4D Flow MR Images by Reducing its Divergence. *IEEE Transactions on Medical Imaging*, 35(10), 2353–2364. doi: 10.1109/TMI.2016.2570010
- Nagata, Y., Kado, Y., Onoue, T., Otani, K., Nakazono, A., Otsuji, Y., & Takeuchi, M. (2018, mar). Impact of image quality on reliability of the measurements of left

- ventricular systolic function and global longitudinal strain in 2D echocardiography. *Echo Research and Practice*, 5(1), 27–39. doi: 10.1530/erp-17-0047
- Neizel, M., Lossnitzer, D., Korosoglou, G., Schäufole, T., Lewien, A., Steen, H., ... Giannitsis, E. (2009, jan). Strain-encoded (SENC) magnetic resonance imaging to evaluate regional heterogeneity of myocardial strain in healthy volunteers: Comparison with conventional tagging. *Journal of Magnetic Resonance Imaging*, 29(1), 99–105. Retrieved from <http://doi.wiley.com/10.1002/jmri.21612> doi: 10.1002/jmri.21612
- NessAiver, M., & Prince, J. L. (2003). Magnitude image CSPAMM reconstruction (MICSr). *Magnetic Resonance in Medicine*, 50(2), 331–342. doi: 10.1002/mrm.10523
- Osman, N. F., Kerwin, W. S., McVeigh, E. R., & Prince, J. L. (1999, dec). Cardiac motion tracking using CINE harmonic phase (HARP) magnetic resonance imaging. *Magnetic Resonance in Medicine*, 42(6), 1048–1060. doi: 10.1002/(SICI)1522-2594(199912)42:6<1048::AID-MRM9>3.0.CO;2-M
- Osman, N. F., McVeigh, E. R., & Prince, J. L. (2000). Imaging heart motion using harmonic phase MRI. *IEEE Transactions on Medical Imaging*, 19(3), 186–202. doi: 10.1109/42.845177
- Osman, N. F., Sampath, S., Atalar, E., & Prince, J. L. (2001, aug). Imaging longitudinal cardiac strain on short-axis images using strain-encoded MRI. *Magnetic Resonance in Medicine*, 46(2), 324–334. doi: 10.1002/mrm.1195
- Owan, T. E., Hodge, D. O., Herges, R. M., Jacobsen, S. J., Roger, V. L., & Redfield, M. M. (2006, jul). Trends in Prevalence and Outcome of Heart Failure with Preserved Ejection Fraction. *New England Journal of Medicine*, 355(3), 251–259. doi: 10.1056/nejmoa052256
- Park, J., Metaxas, D., & Axel, L. (1996). Analysis of left ventricular wall motion based on volumetric deformable models and MRI-SPAMM. *Medical Image Analysis*, 1(1), 53–71. doi: 10.1016/S1361-8415(01)80005-0

- Park, J., Metaxas, D., Young, A. A., & Axel, L. (1996). Deformable models with parameter functions for cardiac motion analysis from tagged MRI data. *IEEE Transactions on Medical Imaging*, 15(3), 278–289. doi: 10.1109/42.500137
- Park, J., Metaxas, D. N., Axel, L., Yuan, Q., & Blom, A. S. (1999). Cascaded MRI-SPAMM for LV motion analysis during a whole cardiac cycle. *International Journal of Medical Informatics*, 55(2), 117–126. doi: 10.1016/S1386-5056(99)00026-X
- Petitjean, C., Rougon, N., & Cluzel, P. (2005). Assessment of myocardial function: A review of quantification methods and results using tagged MRI. *Journal of Cardiovascular Magnetic Resonance*, 7(2), 501–516. doi: 10.1081/JCMR-200053610
- Poggio, T., & Girosi, F. (1990). Networks for Approximation and Learning. *Proceedings of the IEEE*, 78(9), 1481–1497. doi: 10.1109/5.58326
- Ponikowski, P., Voors, A. A., Anker, S. D., Bueno, H., Cleland, J. G., Coats, A. J., ... Davies, C. (2016, jul). *2016 ESC Guidelines for the diagnosis and treatment of acute and chronic heart failure* (Vol. 37) (No. 27). Oxford University Press. doi: 10.1093/eurheartj/ehw128
- Prince, J. L., & McVeigh, E. R. (1992). Motion Estimation from Tagged MR Image Sequences. *IEEE Transactions on Medical Imaging*, 11(2), 238–249. doi: 10.1109/42.141648
- Pruessmann, K. P., Weiger, M., Scheidegger, M. B., & Boesiger, P. (1999, nov). SENSE: Sensitivity encoding for fast MRI. *Magnetic Resonance in Medicine*, 42(5), 952–962. Retrieved from <http://doi.wiley.com/10.1002/%28SICI%291522-2594%28199911%2942%3A5%3C952%3A%3AAID-MRM16%3E3.0.CO%3B2-S> doi: 10.1002/(SICI)1522-2594(199911)42:5<952::AID-MRM16>3.0.CO;2-S
- Qian, Z., Metaxas, D. N., & Axel, L. (2006). Extraction and tracking of MRI tagging sheets using a 3D gabor filter bank. *Annual International Conference of the IEEE Engineering in Medicine and Biology - Proceedings*, 711–714. doi: 10.1109/IEMBS.2006.259542
- Radeva, P., Amini, A. A., & Huang, J. (1997, may). Deformable B-Solids and Implicit

- Snakes for 3D Localization and Tracking of SPAMM MRI Data. *Computer Vision and Image Understanding*, 66(2), 163–178. doi: 10.1006/cviu.1997.0611
- Reichek, N. (2017, nov). *Myocardial Strain: Still a Long Way to Go* (Vol. 10) (No. 11). NLM (Medline). doi: 10.1161/CIRCIMAGING.117.007145
- Reinhardt, J. M., Ding, K., Cao, K., Christensen, G. E., Hoffman, E. A., & Bodas, S. V. (2008, dec). Registration-based estimates of local lung tissue expansion compared to xenon CT measures of specific ventilation. *Medical Image Analysis*, 12(6), 752–763. doi: 10.1016/j.media.2008.03.007
- Reyhan, M., Natsuaki, Y., & Ennis, D. B. (2014). Off-resonance insensitive complementary SPAtial Modulation of Magnetization (ORI-CSPAMM) for quantification of left ventricular twist. *Journal of Magnetic Resonance Imaging*, 39(2), 339–345. doi: 10.1002/jmri.24154
- Rutz, A. K., Ryf, S., Plein, S., Boesiger, P., & Kozerke, S. (2008, apr). Accelerated whole-heart 3D CSPAMM for myocardial motion quantification. *Magnetic Resonance in Medicine*, 59(4), 755–763. doi: 10.1002/mrm.21363
- Ryf, S., Spiegel, M. A., Gerber, M., & Boesiger, P. (2002, sep). Myocardial tagging with 3D-CSPAMM. *Journal of Magnetic Resonance Imaging*, 16(3), 320–325. doi: 10.1002/jmri.10145
- Ryf, S., Tsao, J., Schwitter, J., Stuessi, A., & Boesiger, P. (2004, nov). Peak-combination HARP: A method to correct for phase errors in HARP. *Journal of Magnetic Resonance Imaging*, 20(5), 874–880. doi: 10.1002/jmri.20186
- Salgo, I. S., Tsang, W., Ackerman, W., Ahmad, H., Chandra, S., Cardinale, M., & Lang, R. M. (2012, jan). Geometric assessment of regional left ventricular remodeling by three-dimensional echocardiographic shape analysis correlates with left ventricular function. *Journal of the American Society of Echocardiography*, 25(1), 80–88. doi: 10.1016/j.echo.2011.09.014
- Sampath, S., Kim, J. H., Lederman, R. J., & McVeigh, E. R. (2008). Simultaneous imaging of myocardial motion and chamber blood flow with SPAMM n' EGGS (Spatial Modulation of Magnetization with Encoded Gradients for Gauging Speed).

- Journal of Magnetic Resonance Imaging*, 27(4), 809–817. doi: 10.1002/jmri.21295
- Schuster, A., Morton, G., Hussain, S. T., Jogiya, R., Kutty, S., Asrress, K. N., ... Nagel, E. (2013). The intra-observer reproducibility of cardiovascular magnetic resonance myocardial feature tracking strain assessment is independent of field strength. *European Journal of Radiology*, 82(2), 296–301. doi: 10.1016/j.ejrad.2012.11.012
- Schuster, A., Paul, M., Bettencourt, N., Morton, G., Chiribiri, A., Ishida, M., ... Nagel, E. (2013, jun). Cardiovascular magnetic resonance myocardial feature tracking for quantitative viability assessment in ischemic cardiomyopathy. *International Journal of Cardiology*, 166(2), 413–420. doi: 10.1016/J.IJCARD.2011.10.137
- Selvadurai, B. S., Puntmann, V. O., Bluemke, D. A., Ferrari, V. A., Friedrich, M. G., Kramer, C. M., ... Nagel, E. (2018, jun). Definition of Left Ventricular Segments for Cardiac Magnetic Resonance Imaging. *JACC: Cardiovascular Imaging*, 11(6), 926–928. doi: 10.1016/j.jcmg.2017.09.010
- Sigfridsson, A., Haraldsson, H., Ebbers, T., Knutsson, H., & Sakuma, H. (2011). In vivo SNR in DENSE MRI; temporal and regional effects of field strength, receiver coil sensitivity and flip angle strategies. *Magnetic Resonance Imaging*, 29(2), 202–208. doi: 10.1016/j.mri.2010.08.016
- Škardová, K., Rambašek, M., Chabiniok, R., & Genet, M. (2019, oct). Mechanical and Imaging Models-Based Image Registration. In *Lecture notes in computational vision and biomechanics* (Vol. 34, pp. 77–85). Springer Netherlands. doi: 10.1007/978-3-030-32040-9\_9
- Smiseth, O. A., Torp, H., Opdahl, A., Haugaa, K. H., & Urheim, S. (2016, apr). Myocardial strain imaging: how useful is it in clinical decision making? *European heart journal*, 37(15), 1196–207. Retrieved from <http://www.ncbi.nlm.nih.gov/pubmed/26508168>  
<http://www.pubmedcentral.nih.gov/articlerender.fcgi?artid=PMC4830908> doi: 10.1093/eurheartj/ehv529
- Spottiswoode, B. S., Zhong, X., Hess, A. T., Kramer, C. M., Meintjes, E. M., Mayosi, B. M., & Epstein, F. H. (2007). Tracking myocardial motion from cine DENSE

- images using spatiotemporal phase unwrapping and temporal fitting. *IEEE Transactions on Medical Imaging*, 26(1), 15–30. doi: 10.1109/TMI.2006.884215
- Spottiswoode, B. S., Zhong, X., Lorenz, C. H., Mayosi, B. M., Meintjes, E. M., & Epstein, F. H. (2008). 3D myocardial tissue tracking with slice followed cine DENSE MRI. *Journal of Magnetic Resonance Imaging*, 27(5), 1019–1027. doi: 10.1002/jmri.21317
- Stuber, M., Spiegel, M. A., Fischer, S. E., Scheidegger, M. B., Danias, P. G., Pedersen, E. M., & Boesiger, P. (1999, oct). Single breath-hold slice-following CSPAMM myocardial tagging. *Magma: Magnetic Resonance Materials in Physics, Biology, and Medicine*, 9(1-2), 85–91. doi: 10.1007/BF02634597
- Sundar, H., Davatzikos, C., & Biros, G. (2009). Biomechanically-constrained 4D estimation of myocardial motion. In *Lecture notes in computer science (including subseries lecture notes in artificial intelligence and lecture notes in bioinformatics)* (Vol. 5762 LNCS, pp. 257–265). Springer, Berlin, Heidelberg. Retrieved from [https://link.springer.com/chapter/10.1007/978-3-642-04271-3\\_32](https://link.springer.com/chapter/10.1007/978-3-642-04271-3_32) doi: 10.1007/978-3-642-04271-3\_32
- Swoboda, P., Larghat, A., Greenwood, J., & Plein, S. (2011, dec). Reproducibility of strain and twist measurements calculated using CSPAMM tagging. *Journal of Cardiovascular Magnetic Resonance*, 13(S1), P52. Retrieved from <https://jcmr-online.biomedcentral.com/articles/10.1186/1532-429X-13-S1-P52> doi: 10.1186/1532-429x-13-s1-p52
- Tecelão, S. R., Zwanenburg, J. J., Kuijjer, J. P., & Marcus, J. T. (2006). Extended harmonic phase tracking of myocardial motion: Improved coverage of myocardium and its effect on strain results. *Journal of Magnetic Resonance Imaging*, 23(5), 682–690. doi: 10.1002/jmri.20571
- Van Rossum, G., & Drake, F. L. (2009). *Python 3 Reference Manual*. Scotts Valley, CA: CreateSpace.
- Venkatesh, B. A., Gupta, H., Lloyd, S. G., Dell'Italia, L., & Denney, T. S. (2010, apr). 3D left ventricular strain from unwrapped harmonic phase measurements. *Journal*

- of Magnetic Resonance Imaging*, 31(4), 854–862. doi: 10.1002/jmri.22099
- Wang, D., Fu, Y., & Ashraf, M. A. (2015). Artifacts reduction in strain maps of tagged magnetic resonance imaging using harmonic phase. *Open medicine (Warsaw, Poland)*, 10(1), 425–433. doi: 10.1515/med-2015-0074
- Wang, H., & Amini, A. A. (2010, mar). Accurate 2D cardiac motion tracking using scattered data fitting incorporating phase information from MRI. In R. C. Molthen & J. B. Weaver (Eds.), (Vol. 7626, p. 76260M). International Society for Optics and Photonics. doi: 10.1117/12.846390
- Wang, H., & Amini, A. A. (2011, mar). Cardiac motion tracking with multilevel B-splines and SinMod from tagged MRI. In J. B. Weaver & R. C. Molthen (Eds.), (Vol. 7965, p. 796520). International Society for Optics and Photonics. doi: 10.1117/12.878825
- Wang, H., & Amini, A. A. (2012). Cardiac motion and deformation recovery from MRI: A review. *IEEE Transactions on Medical Imaging*, 31(2), 487–503. doi: 10.1109/TMI.2011.2171706
- Wang, H., & Amini, A. a. (2013). Cardiac deformation analysis using 3D SinMod from 3D CSPAMM tagged MRI. In *Proceedings volume 8672, medical imaging 2013: Biomedical applications in molecular, structural, and functional imaging* (Vol. 8672, p. 86720B). doi: 10.1117/12.2008426
- Wang, H., Kadbi, M., Alshaher, M., Kotys-Traughber, M., Fischer, S., & Amini, A. (2012, dec). Cardiac deformation analysis from orthogonal CSPAMM (OCSPAMM) tagged MRI. *Journal of Cardiovascular Magnetic Resonance*, 14(S1), 1–2. Retrieved from <http://www.jcmr-online.com/content/14/S1/W17> doi: 10.1186/1532-429x-14-s1-w17
- Wang, H., Kadbi, M., Kotys, M., Ersoy, M., Chatzimavroudis, G. P., Setser, R. M., ... Amini, A. A. (2011, sep). Orthogonal CSPAMM (OCSPAMM) MR tagging for imaging ventricular wall motion. In *Proceedings of the annual international conference of the ieee engineering in medicine and biology society, embs* (pp. 535–538). doi: 10.1109/IEMBS.2011.6090098

- Wehner, G. J., Jing, L., Haggerty, C. M., Suever, J. D., Chen, J., Hamlet, S. M., . . . Fornwalt, B. K. (2018, dec). Comparison of left ventricular strains and torsion derived from feature tracking and DENSE CMR. *Journal of Cardiovascular Magnetic Resonance*, *20*(1), 63. doi: 10.1186/s12968-018-0485-4
- Wu, L., Germans, T., Güçlü, A., Heymans, M. W., Allaart, C. P., & Van Rossum, A. C. (2014). Feature tracking compared with tissue tagging measurements of segmental strain by cardiovascular magnetic resonance. *Journal of Cardiovascular Magnetic Resonance*, *16*(1), 10. doi: 10.1186/1532-429X-16-10
- You, W., Evangelou, I. E., Zun, Z., Andescavage, N., & Limperopoulos, C. (2016, apr). Robust preprocessing for stimulus-based functional MRI of the moving fetus. *Journal of Medical Imaging*, *3*(2), 026001. Retrieved from <https://www.spiedigitallibrary.org/terms-of-use> doi: 10.1117/1.jmi.3.2.026001
- Young, A. (2006). Assessment of cardiac performance with magnetic resonance imaging. *Current Cardiology Reviews*, *2*(4), 271–282. doi: 10.2174/157340306778772904
- Young, A. A. (1999, dec). Model tags: Direct three-dimensional tracking of heart wall motion from tagged magnetic resonance images. *Medical Image Analysis*, *3*(4), 361–372. doi: 10.1016/S1361-8415(99)80029-2
- Young, A. A., & Axel, L. (1992, oct). Three-dimensional motion and deformation of the heart wall: Estimation with spatial modulation of magnetization - A model-based approach. *Radiology*, *185*(1), 241–247. doi: 10.1148/radiology.185.1.1523316
- Young, A. A., Kraitchman, D. L., Dougherty, L., & Axel, L. (1995). Tracking and Finite Element Analysis of Stripe Deformation in Magnetic Resonance Tagging. *IEEE Transactions on Medical Imaging*, *14*(3), 413–421. doi: 10.1109/42.414605
- Young, A. A., Kramer, C. M., Ferrari, V. A., Axel, L., & Reichek, N. (1994, aug). Three-dimensional left ventricular deformation in hypertrophic cardiomyopathy. *Circulation*, *90*(2), 854–867. doi: 10.1161/01.CIR.90.2.854
- Young, A. A., Li, B., Kirton, R. S., & Cowan, B. R. (2012, jun). Generalized spatiotemporal myocardial strain analysis for DENSE and SPAMM imaging. *Magnetic*

- Resonance in Medicine*, 67(6), 1590–1599. doi: 10.1002/mrm.23142
- Zerhouni, E. A., Parish, D. M., Rogers, W. J., Yang, A., & Shapiro, E. P. (1988, oct). Human heart: Tagging with MR imaging - A new method for noninvasive assessment of myocardial motion. *Radiology*, 169(1), 59–63. doi: 10.1148/radiology.169.1.3420283
- Zhang, Z., Dione, D. P., Brown, P. B., Shapiro, E. M., Sinusas, A. J., & Sampath, S. (2011). Assessment of early diastolic strain-velocity temporal relationships using spatial modulation of magnetization with polarity alternating velocity encoding (SPAMM-PAV). *Magnetic Resonance in Medicine*, 66(6), 1627–1638. doi: 10.1002/mrm.22965
- Zhang, Z., Friedman, D., Dione, D. P., Lin, B. A., Duncan, J. S., Sinusas, A. J., & Sampath, S. (2013, sep). Assessment of left ventricular 2D flow pathlines during early diastole using spatial modulation of magnetization with polarity alternating velocity encoding: A study in normal volunteers and canine animals with myocardial infarction. *Magnetic Resonance in Medicine*, 70(3), 766–775. Retrieved from <http://doi.wiley.com/10.1002/mrm.24517> doi: 10.1002/mrm.24517
- Zhong, X., Spottiswoode, B. S., Meyer, C. H., Kramer, C. M., & Epstein, F. H. (2010, jun). Imaging three-dimensional myocardial mechanics using navigator-gated volumetric spiral cine DENSE MRI. *Magnetic Resonance in Medicine*, 64(4), 1089–1097. doi: 10.1002/mrm.22503

**APPENDIX**

## A. APPENDIX FOR PUBLICATION 1

### A.1. Motion model

The two-dimensional motion model of the idealized left-ventricle (LV) used in the experiments was introduced in (Gilliam & Epstein, 2012) and depends on several parameters defining both the geometry and its behaviour. Let  $t \in [0, 1]$  denote the time through the cardiac cycle. The position of the deformed LV tissue is given by the polar pair  $(r, \theta)$ :

$$\begin{bmatrix} r(t) \\ \theta(t) \end{bmatrix} = \begin{bmatrix} r_{ED} \\ \theta_{ED} \end{bmatrix} + \begin{bmatrix} u_r(t) \\ u_\theta(t) \end{bmatrix}, \quad (\text{A.1})$$

where  $r, \theta$  denotes the position of the deformed tissue at the time  $t$ ,  $(r_{ED}, \theta_{ED})$  the end-diastolic position of the tissue (the reference position at  $t = 0$ ), and  $(u_r, u_\theta)$  the radial and angular displacement of the tissue at the time  $t$  which are defined through the set of parameters  $[d_{ep}, \varphi_{ep}]$  and  $[d_{en}, \varphi_{en}]$  via:

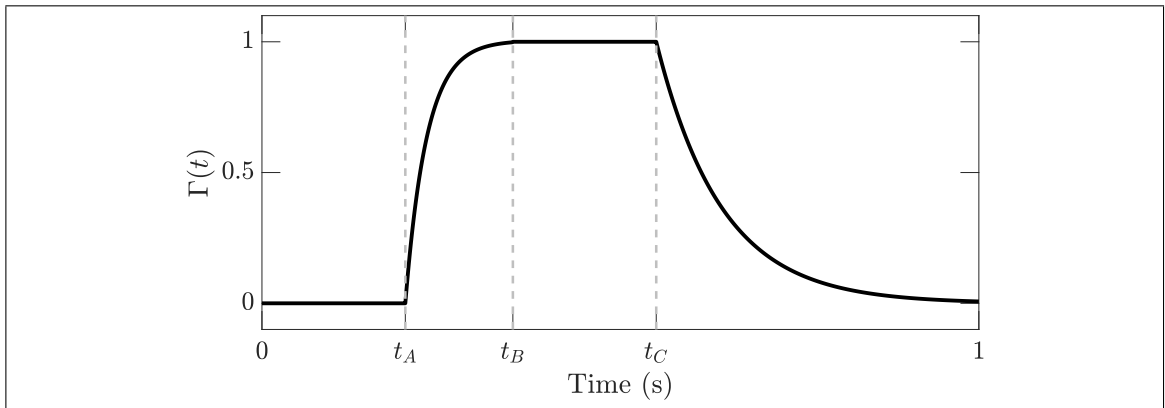


Figure A.1. Modulation function used to weight the cardiac motion.

$$\begin{bmatrix} u_r(t) \\ u_\theta(t) \end{bmatrix} = \Gamma(t) \begin{bmatrix} (1 - \mu)d_{ep} + \mu d_{en} \\ (1 - \mu)\varphi_{ep} + \mu\varphi_{en}, \end{bmatrix} \quad (\text{A.2})$$

where  $\Gamma(t)$  is a modulation function used to emulate the cardiac cycle (see Figure A1) given by:

$$\Gamma(t) = \begin{cases} 0 & \text{if } t < t_A \\ 1.005 - 1.005e^{-5(t-t_A)/(t_B-t_A)} & \text{if } t_A \leq t < t_B \\ e^{-11(t-t_C)} & \text{if } t \geq t_B \end{cases} \quad (\text{A.3})$$

The  $\mu$  parameter given in (A.2) is calculated as:

$$\mu = \left( \frac{R_{ep} - r_{ED}}{R_{ep} - R_{en}} \right)^\sigma, \quad (\text{A.4})$$

where  $r_{ep}$  represents the epicardial radius,  $R_{en}$  the endocardial radius, and  $\sigma \in [0, \infty[$  a parameter that skews the motion towards the epicardial ( $\sigma > 1$ ) or endocardial ( $\sigma < 1$ ) wall. Thus, the end-systolic position of the LV is obtained using:

$$\begin{bmatrix} r_{ES} \\ \theta_{ES} \end{bmatrix} = \begin{bmatrix} r_{ED} \\ \theta_{ED} \end{bmatrix} + \begin{bmatrix} (1 - \mu)d_{ep} + \mu d_{en} \\ (1 - \mu)\varphi_{ep} + \mu\varphi_{en} \end{bmatrix}. \quad (\text{A.5})$$

For patient data, the displacement given in (A.2) is slightly modified to obtain an abnormal motion pattern using:

$$\begin{bmatrix} u_r^p(t) \\ u_\theta^p(t) \end{bmatrix} = \Gamma(t) \left( \Psi(\theta_{ED}) \begin{bmatrix} r_{ES} \\ \theta_{ES} \end{bmatrix} - \begin{bmatrix} r_{ED} \\ \theta_{ED} \end{bmatrix} \right), \quad (\text{A.6a})$$

$$\Psi(\theta) = \frac{\chi(1 - \cos(\theta - \psi))}{2}, \quad (\text{A.6b})$$

where  $\Psi$  is a weighting function that reduces the tissue motion in the direction  $\psi \in [0, 2\pi]$  by a factor  $\chi \in [0, 1]$ .

The set of parameters used in this study are presented in Table A.1.

For the three-dimensional simulations, the through plane component of the motion is completely described in the article.

Table A.1. Set of parameters used to generate the synthetic geometries and motion patterns. The notation  $x \sim \mathcal{U}(a, b)$  means that for every simulation, the variable  $x$  was selected from a uniform distribution on the range  $(a, b)$ . The epicardial radius is calculated using  $R_{ep} = R_{en} + \tau$ ,  $d_{en} = (1 - S_{en})R_{en}$ , and  $d_{ep}$  was calculated to obtain the change in left-ventricular area imposed by  $S_{ar}$ .

Parameter name	Parameter symbol and value
End-diastolic endocardial radius	$R_{en} \sim \mathcal{U}(10, 30)$ mm
End-diastolic wall thickness	$\tau \sim \mathcal{U}(7.5, 12.5)$ mm
End-systolic endocardial scaling	$S_{en} \sim \mathcal{U}(0.6, 0.8)$
End-systolic area scaling	$S_{ar} \sim \mathcal{U}(0.6, 0.8)$
End-systolic endocardial twist	$\varphi_{en} \sim \mathcal{U}(-10^\circ, 10^\circ)$
End-systolic epicardial twist	$\varphi_{ep} = 0^\circ$
$\Gamma(t)$ parameters (see Fig. A.1)	$t_A \sim \mathcal{U}(0.05, 0.15)$
	$t_B \sim \mathcal{U}(0.35, 0.45)$
	$t_C \sim \mathcal{U}(0.5, 0.6)$
Abnormal angle (if present)	$\psi \sim \mathcal{U}(0^\circ, 360^\circ)$
Abnormal scale (if present)	$\chi \sim \mathcal{U}(0.5, 1.5)$
Motion skew parameter	$\sigma \sim \mathcal{U}(0.5, 1.7)$

## B. APPENDIX FOR PUBLICATION 2

### B.1. Exact interpolation condition

To determine the RBF weights associated with the interpolation function  $g(\cdot)$  in Eq. 3.7, satisfying the exact interpolation condition  $g(\mathbf{X}_V(\mathbf{x}_i, t_k)) = \mathbf{x}_i$ , the following linear system must be solved (Buhmann, 2003):

$$\Psi \boldsymbol{\lambda} = \mathbf{G} \quad (\text{B.1})$$

where  $\boldsymbol{\lambda}$  is a column vector of RBF weights,  $\mathbf{G}$  a column vector containing the deformed positions of each pixel (observations), and each element of the matrix  $\Psi$ , for  $m, n \in \{1, \dots, N_{\text{pixels}}\}$ , is given by:

$$\Psi_{mn} = \psi(\|\mathbf{X}_V(\mathbf{x}_m, t_k) - \mathbf{X}_V(\mathbf{x}_n, t_k)\|). \quad (\text{B.2})$$

### B.2. Evaluated norms in the RBF interpolator

As the deformation map  $\varphi(\mathbf{X}, t)$  is invertible (Gurtin et al., 2010), there are two points  $\mathbf{P} \in \mathbf{R}_0$  and  $\mathbf{p} \in \mathbf{R}_k$  satisfying  $\mathbf{X}(\mathbf{x}(\mathbf{p}), t_k) = \mathbf{X}(\mathbf{P}, t_0)$  (see Figure 3.1). Therefore, the next relation holds:

$$\mathbf{X}_V(\mathbf{P}, t_0) - \mathbf{X}_V(\mathbf{x}(\mathbf{p}), t_k) = \Delta \mathbf{n}_\phi \quad (\text{B.3})$$

where  $\Delta \mathbf{n}_\phi(\mathbf{x}) = \mathbf{n}_\phi(\mathbf{P}, t_0) - \mathbf{n}_\phi(\mathbf{p}, t_k)$  represents a noise difference.

Considering that the euclidean norm of the relation Eq. B.3 relates to the noise difference, the evaluation of  $\mathbf{X}_V(\mathbf{X}, t_0)$  in the interpolator in Eq. 3.7 gives an estimate of the target function on the reference domain.

## C. SUMMARY OF PARTICIPATION IN OTHER RESEARCH PROJECTS

### C.1. Research articles

- Sotelo J., Bissell M., Jiang Y., Mella H., Mura J., and Uribe S. “Three-dimensional quantification of circulation using finite-element methods in 4D Flow MR data of the thoracic aorta”. *Magnetic Resonance in Medicine*. Published August 2021.
- Mella H., Wang H., Montalba C., and Uribe S. “An Off-Resonance Insensitive Orthogonal CSPAMM sequence (ORI-O-CSPAMM) for the acquisition of CSPAMM and MICSr grids in half scan time”. *Magnetic Resonance in Medicine*. Published July 2021.
- Mella H., Mura J., Sotelo J., and Uribe S. “A Comprehensive Comparison Between Shortest-Path HARP Refinement, SinMod, and DENSEanalysis Processing Tools Applied to CSPAMM and DENSE Images”. *Magnetic Resonance Imaging*. Submitted July 2021.
- Mella H., Mura J., Wang H., Taylor M., Chabiniok R., Tintera J., Sotelo J., and Uribe S. “HARP-I: A harmonic phase interpolation method for the estimation of motion from tagged MR images”. *IEEE Transactions on Medical Imaging*. Published January 2021.
- Garay J., Mella H., Sotelo J., Cárcamo C., Uribe S., Mura J., and Bertoglio C. “A new mathematical model for verifying the Navier-Stokes compatibility of 4D Flow MRI data”. *Journal of Computational Physics*. Submitted January 2021.
- Mura J., Sotelo J., Mella H., Wong J., Hussain T., Ruijsink B., and Uribe S. “Noninvasive local pulse wave velocity using 4D flow MRI”. *Biomedical Signal Processing and Control*. Submitted June 2020.

## C.2. International conferences

- “An Off-Resonance Insensitive Orthogonal CSPAMM Sequence (ORI-O-CSPAMM)”. Paper presented at the 29th Annual Meeting of the International Society for Magnetic Resonance (first author). Online, May 2021.
- “Beyond SPAMM-PAV: a Phase Complementary SPAMM (PCSPAMM) acquisition to quantify simultaneously tissue motion and flow velocity”. Paper presented at the 28th Annual Meeting of the International Society for Magnetic Resonance (first author). Online, August 2020.
- “A novel, accurate and robust three-dimensional quantification of circulation using finite-element methods in 4D Flow MRI data of thoracic aorta”. Paper presented at the 28th Annual Meeting of the International Society for Magnetic Resonance (co-author and speaker). Online, August 2020.
- “A Harmonic phase interpolation method for the estimation of motion from tagged MR images”. Paper presented at the 27th Annual Meeting of the International Society for Magnetic Resonance in Medicine (first author). Montreal, CA, June 2019.
- “PyMRStrain: A Python library for the generation of SPAMM, C-SPAMM, and DENSE synthetic images”. Paper presented at the 27th Annual Meeting of the International Society for Magnetic Resonance in Medicine (first author). Montreal, CA, June 2019.
- “4D-flow MRI and robust local pulse wave velocity allow the detection of alterations in human aortas”. Paper presented at the 27th Annual Meeting of the International Society for Magnetic Resonance in Medicine (co-author). Montreal, CA, June 2019.
- “A Python finite element based library for strain phantoms generation”. Paper presented at the 26th Annual Meeting of the International Society for Magnetic Resonance in Medicine (first author). Paris, FR, June 2018.

- “Implementation of a mixed and hybrid formulation of the PML method in elastodynamics using FEniCS”. Paper presented at the FEniCS Conference, Luxembourg, LU, June 2017.
- “Left ventricle strain estimation using flow data”. Paper presented at the 25th Annual Meeting of the International Society for Magnetic Resonance in Medicine (first author). Honolulu, HI, April 2017.

### **C.3. National conferences**

- “Improved motion estimation from tagged cardiac MRI”. Paper presented at the 1st Chilean Meeting of Biomechanics and Biomaterials (first author and speaker). Online, October 2020.
- “Estimación de deformaciones en el ventrículo izquierdo usan imágenes de flujo”. Paper presented at the 16th Jornadas de Mecánica Computacional (first author and speaker). October 2017.
- “Implementación eficiente de una formulación mixta e híbrida del método PML en elastodinámica”. Paper presented at the 16th Jornadas de Mecánica Computacional (first author and speaker). October 2017.